AD A025357

ADVANCED H_2 – HCl GAS DYNAMIC LASER

PHASE II

FINAL TECHNICAL REPORT

January 1976

Submitted to:

Dr. David Howgate
U.S. Army Missile Command
Redstone Arsenal, Alabama 35809

Under Contract No. DAAH01-75-C-0789

Submitted by:

Atlantic Research Corporation
5390 Cherokee Avenue
Alexandria, Virginia 22314

ARC No. 47-5655

ATLANTIC RESEARCH CORPORATION
ALEXANDRIA, VIRGINIA · 22314

ADVANCED H_2 — HCl GAS DYNAMIC LASER,
PHASE II .

FINAL TECHNICAL REPORT, *apr - Dec 75.*

Jan 76

⑪

⑫ 152 p.

Submitted to:

Dr. David Howgate
U. S. Army Missile Command
Redstone Arsenal, Alabama
35809

Under Contract No. DAAH01-75-C-0789

Submitted by:

Atlantic Research Corporation
5390 Cherokee Avenue
Alexandria, Virginia   22314

ARC -47-5655

i

FOREWARD

This final technical report on an "Advanced H_2 - HCl Gas Dynamic Laser" was prepared by Atlantic Research Corporation, 5390 Cherokee Avenue, Alexandria, Virginia, 22314. The Project Engineer was Dr. Robert Cavalleri, the program was directed by Robert Naismith. The major subcontractor was Physical Sciences Inc., 18 Lakeside Office Park, Wakefield, Massachusetts, 01880. The principal investigator of that effort was Dr. Raymond Taylor. Technical support was provided by Stephen Scheffee of Atlantic Research Corporation and Dr. David Rosen, John Coughlin and Dr. Peter Wu, of Physical Sciences, Inc.

The effort was conducted from April 1975 through December 1975. The effort was administered under the Army Missile Command, Redstone Arsenal, Alabama. Dr. David Howgate was the technical monitor.

This report was submitted February 3, 1976 and has been reviewed and is approved for publication.

iii

SUMMARY

The initial phase of this work was a feasibility study of an $H_2^{\prime}$ - HCl mixing gas dynamic laser. The results of that study indicated that a high energy laser system based on the $H_2^{\prime}$ - HCl system was indeed feasible. This laser device concept envisions the use of a solid propellant to generate high temperature $H_2^{\prime}$ - HCl mixtures which are expanded supersonically to create the proper conditions for efficient $H_2^{\prime}$ $\rightarrow$ HCl V $\rightarrow$ V transfer and lasing on HCl. This type of laser device has several significant potential advantages as a high energy device for military application, i.e., the use of compact, field storable solid fuel technology, high specific power (80 - 100 Kj/lb), and lasing of HCl in the 4.0μ atmospheric window.

The objective of the current phase was to experimentally verify the V - V and V - T kinetics for the important H_2 - HCl processes and to develop solid propellant gas generators that could be used to generate the required gases at attractive weight yields. The results of the current phase have verified that the kinetics are capable with operation of a H_2 - HCl laser. In addition, the gas generator development program has succeeded in producing the required gases at weight yields that make the system attractive for Army field application. The potential of even higher gas yields that would make the system even more attractive is also possible but requires additional propellant development. The fundamental remaining problem area is the effect of H-atoms on performance.

TABLE OF CONTENTS

(LIST OF TABLES - CONTINUED)

1.0 INTRODUCTION

The initial phase of this work was a feasibility study of an H_2-HCl mixing gas dynamic laser. The results of that study indicated that a high energy laser based on the H_2-HCl molecular system was indeed feasible. This laser device concept envisions the use of a solid propellant to generate high temperature H_2-HCl mixtures which are expanded supersonically to create the proper conditions for efficient $H_2 \rightarrow$HCl V$\rightarrow$V transfer and lasing on HCl. This type of laser device has several significant potential advantages as a high energy device for military application, i.e., the use of compact, field storable solid fuel technology, high specific power (80-100 Kj/lb), and lasing of HCl in the 4.0μ atmospheric window.

In the initial study phase the critical kinetic and propellant issues that required further research were identified. In the kinetics area, it was determined that the three most critical kinetic rates that control the laser performance were (i) the H_2/HCl V$\rightarrow$V process for which no data were then available, (ii) the HCl/H_2 V$\rightarrow$T process for which only a room temperature data point had been determined, and (iii) the HCl/H V$\rightarrow$T process for which only room temperature measurements existed. In the propellant area, it was determined that gas generators with the desired gaseous weight yields and gas composition must be developed.

The purpose of the present investigation (Phase II) was to provide experimental data on the rates of the H_2/HCl V$\rightarrow$V and HCl/H_2 V$\rightarrow$T processes at temperatures in the range of 1000-2500°K, to develop the gas generators with the required weight yield and gas composition characteristics as well as to perform additional analytical studies for the design of an appropriate proof experiment. The results of this work are reported in this document.

2.0 KINETICS

2.1 Background

As was emphasized in the early stages of the H_2-HCl GDL feasibility study[1], the vibrational energy transfer kinetics play a critical role in determining potential laser performance. The vibrational temperature, gain, and extractable power are all highly dependent on the rates for V-T and V-V exchange. The principal vibrational energy transfer processes used in the harmonic oscillator model are listed in Table 2.1.

There is presently a large body of experimental data on process (1) obtained from several different experiments[2-5] and covering a large temperature range from $150 \leq T \leq 2100$. The rate constant for process (2) has been measured at room temperature[6], and, quite recently, some shock tube-laser fluorescence data by Bott[7] have become available which provide some additional information about process (2) up to T = 770°K. These most recent data by Bott will be discussed later in this section.

Experimental data for V-T process (3) exist from three separate experiments - a low temperature experiment[8] covering the temperature range from approximately 50°K to 450°K and two high temperature shock tube experiments[9,10] covering the temperature range from 1100°K to 2700°K. These data allow us to make a reasonably good curve fit to the rate constant for process (3) over the temperature range of interest for the proposed H_2-HCl GDL.

While there is at present no experimental data in the literature for process (4), it is not expected that this reaction will make a significant contribution to the vibrational energy relaxation. According to theories of the SSH type, HCl is expected to be less efficient at deactivating vibrationally excited H_2 than H_2 itself. This fact coupled with the small concentration of HCl relative to H_2 in the laser medium make the contribution of process (4) negligible.

Perhaps the most critical, yet most poorly determined rate is that for the V-V exchange-process (5). Previous to the present experiment, no experimental data existed for the rate of process (5) and, therefore, the laser modeling calculations have had to be done using an estimated rate expression for this process derived from a combination of empirical correlation and theory[1,10].

TABLE 2.1

$\underline{H_2/HCl}$ VIBRATIONAL ENERGY TRANSFER PROCESSES
HARMONIC OSCILLATOR MODEL

V → T Processes

$$HCl \ (v = 1) + HCl \rightarrow HCl \ (v = 0) + HCl + 2886 \ cm^{1} \qquad (1)$$

$$HCl \ (v = 1) + H_2 \rightarrow HCl \ (v = 0) + H_2 + 2886 \ cm^{-1} \qquad (2)$$

$$H_2 \ (v = 1) + H_2 \rightarrow H_2 \ (v = 0) + H_2 + 4159 \ cm^{-1} \qquad (3)$$

$$H_2 \ (v = 1) + HCl \rightarrow H_2 \ (v = 0) + HCl + 4159 \ cm^{-1} \qquad (4)$$

V → V Process

$$H_2 \ (v = 1) + HCl \ (v = 0) \rightarrow H_2 \ (v = 0) + HCl \ (v = 1) + 1273 \ cm^{-1} \qquad (5)$$

- 3 -
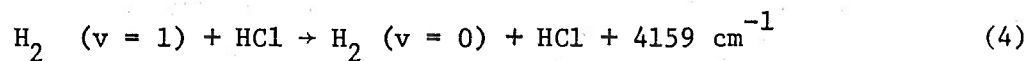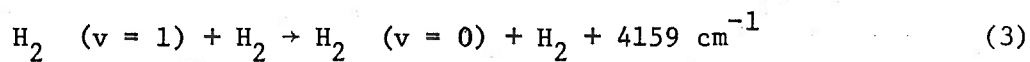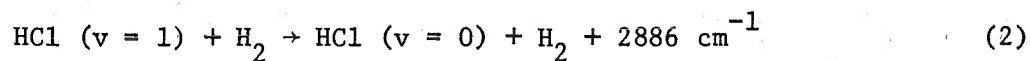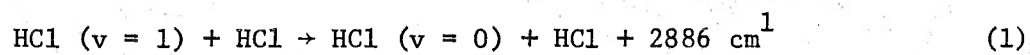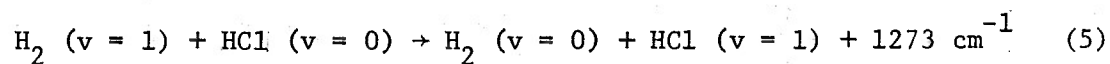
On the basis of the above analysis, it is clear that the important molecular vibrational rate constants that required experimental investigation are those for the V-V process (5) and the V-T process (2). The present shock tube experiment was designed to make measurements of these rate processes over the temperature range of roughly 1000°K to 2500°K.

2.2   Experimental Technique

The experiments were carried out on a conventional 1.5-inch diameter shock tube. A photograph of the general shock tube facility is shown in Figure 2.0.

The basic technique employed monitoring the infrared fluorescence emitted by the HCl behind incident shock waves. It has been shown[11] that the infrared radiation intensity from the fundamental vibrational rotation band is proportional to the vibrational energy in that mode. Therefore, following the time history of emission from the fundamental band is equivalent to measuring the rate of change of the vibrational energy.

The shock tube was constructed of 1.5-inch i.d. stainless steel with a 4-foot long driver section and a 15-foot driven section. Shock waves were produced by bursting scored aluminum and cold rolled steel diaphragms with helium. The shock speeds were measured with a series of six thin film, platinum heat transfer gauges mounted at various positions down the tube. The output from the heat transfer gauges were displayed on a speed raster sweep of a suitably modified Tektronix oscilloscope. A typical photograph of such a speed raster sweep with the differentiated outputs of the various heat transfer gauges is shown in Figure 2.1c.

The infrared emission intensity was detected behind the incident shock by means of the optical system shown in Figure 2.2. The radiation first passed through a 0.50-inch diameter CaF_2 window contoured to match the inner radius of the shock tube. The light was then collected by a 10-cm diameter aluminum mirror with a 30-cm radius of curvature, directed to a flat aluminum mirror, and finally imaged with 1:1 magnification on a 1-mm diameter detector element. The detector was a liquid nitrogen cooled InSb detector operated in the photovoltaic mode. An infrared filter with a bandpass of 3.2 to 5.8μ was placed before the detector to isolate the fundamental HCl emission.
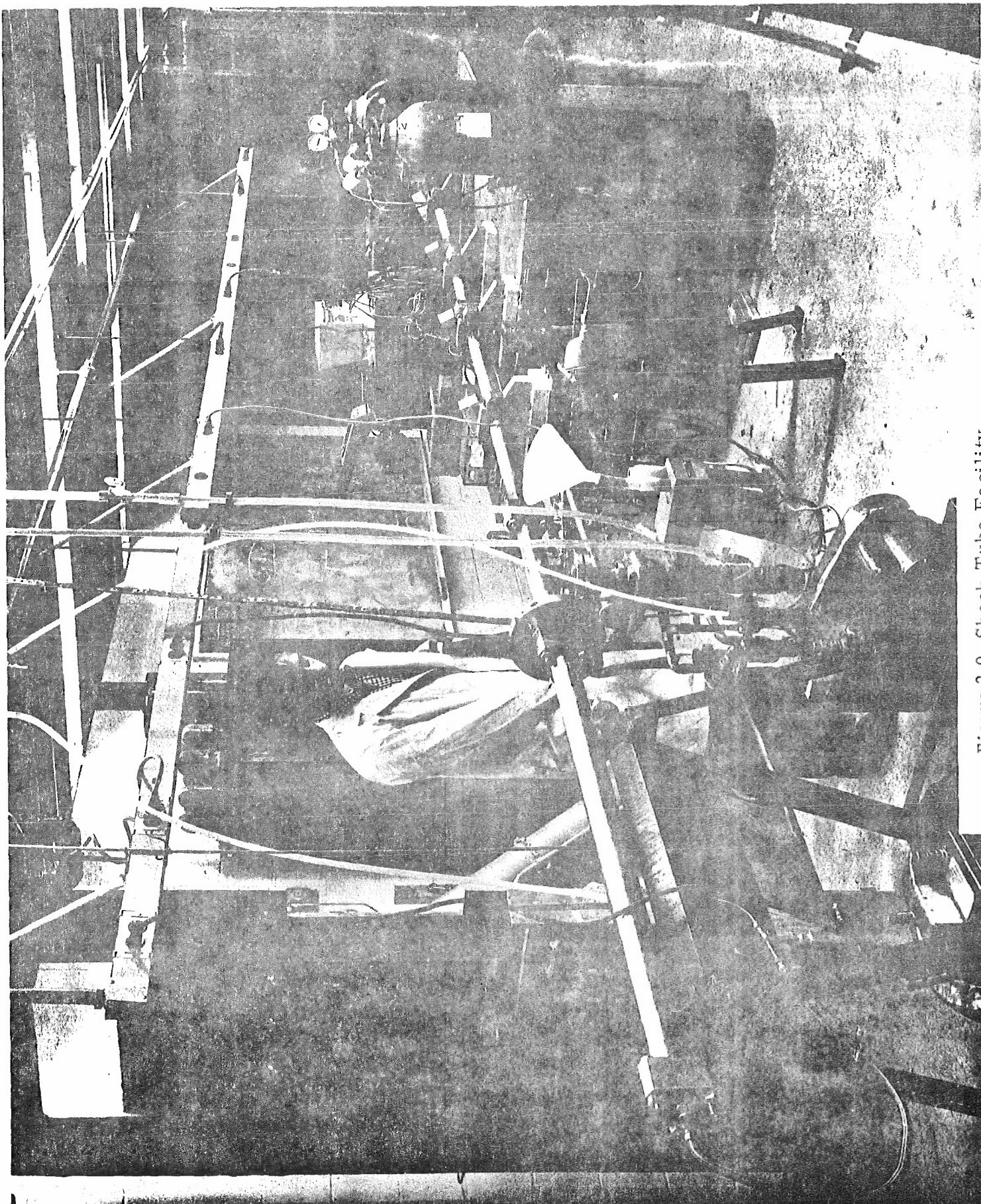
Figure 2.0 Shock Tube Facility

- 5 -

a) IR FLUORESCENCE
0.083 HCl, 0.167 H_2, 0.75 Ar
P_1 = 12 torr, T_2 = 1030 °K

5 μ sec

IR INTENSITY
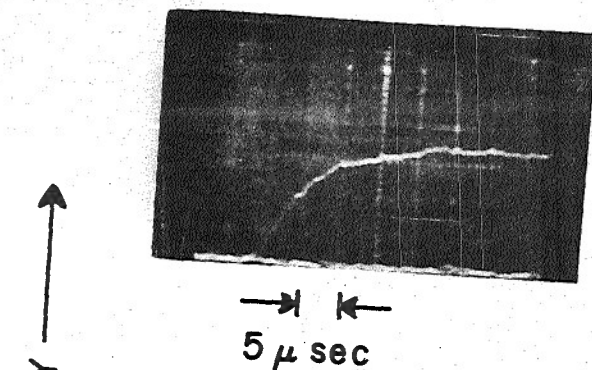
b)

0.03 HCl, 0.57 H_2, 0.40 Ar
P_1 = 7.2 torr, T_2 = 1170 °K

5 μ sec

TIME
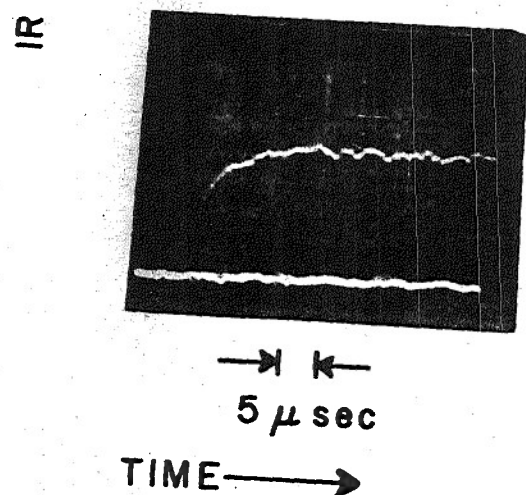
c) SPEED RASTER TRACE

TIME
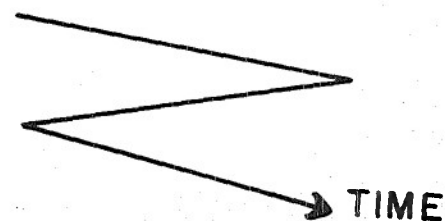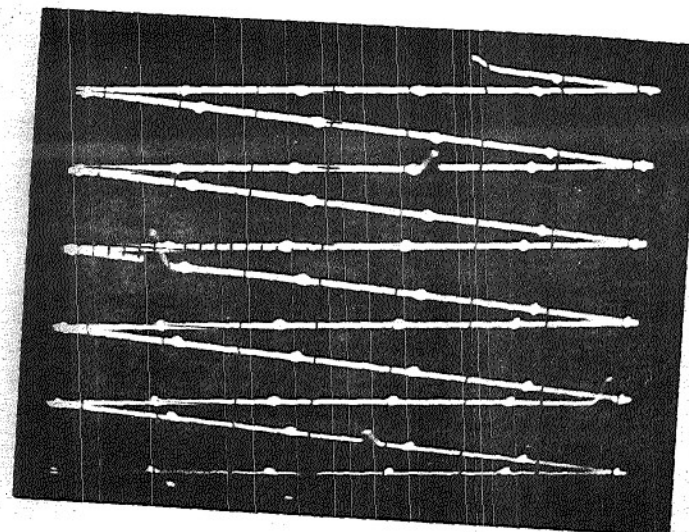
Figure 2.1   Sample Fluorescence and Shock Speed Oscillograms
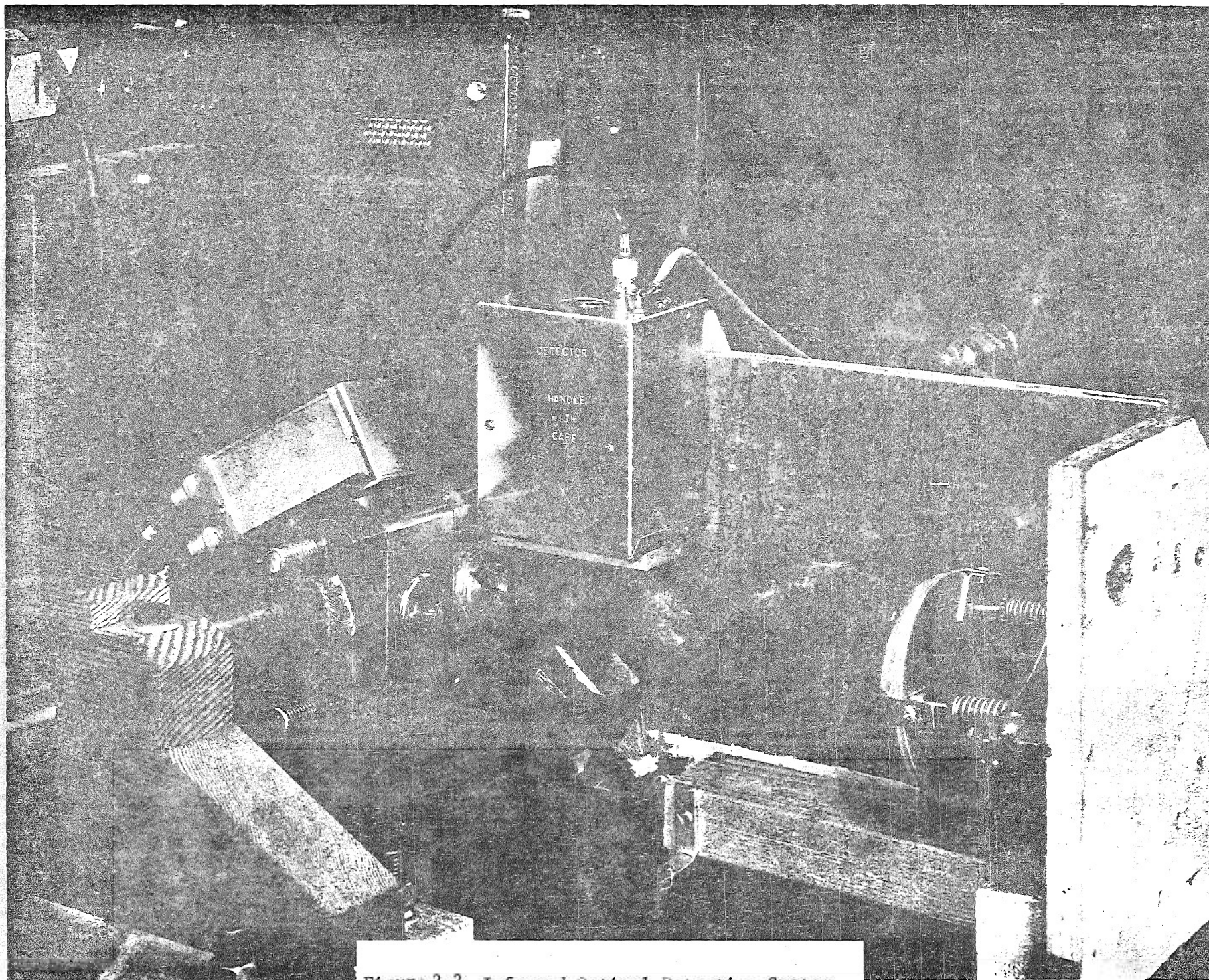
Figure 2.2 Infrared Optical Detection System

The test section of the shock tube was constructed of Lucite to minimize the stray light that might reach the detector by internal reflections off the metal shock tube walls. Before this Lucite section was utilized, light emission was detected before passage of the shock front by the optical station, presumably from radiation emitted down the tube ahead of the shock and reflected into the optical system by the back wall of the original metal test section. Changing the test section to Lucite, which is a poor reflector in the infrared, eliminated this extraneous light.

The output of the IR detector was amplified by a wide band low noise preamplifier of 20 Db gain before recording by a 545B Tektronix oscilloscope. A 3 MHz high frequency cut-off filter was employed immediately before the input to the final amplifying stage of the oscilloscope. The time response of the optical detection system and associated electronics was approximately 1μ sec. A sample of typical IR fluorescence traces is shown in Figures 2.1a and 2.1b.

Initial fill pressures, p_1, in the driven section were measured with a Wallace & Tiernan absolute pressure gauge (0 - 200 torr) and an oil manometer. Typical fill pressures ranged from about 3 torr to 20 torr. The gases used in this tudy were Argon: Matheson Purity, minimum purity 99.995%; HCl: Linde Specialty Gases L.E.D. grade, minimum purity 99.995%; and H_2: Linde Specialty Gases, ultra high purity, minimum purity of 99.999% and a maximum moisture content of 3 ppm. The argon was further purified to remove any possible water content by passage through a copper coil immersed in a dry ice-acetone bath. The HCl was subjected to a freeze-pump-thaw cycle between 77°K and 300°K to remove any residual H_2 that might have formed due to decomposition. This HCl was then passed through a copper coil at dry ice temperature to remove residual water vapor. Finally, the H_2 was passed through a copper coil immersed in a liquid nitrogen bath to trap out any water vapor. The gas mixtures were prepared in a 4 liter stainless steel mixing tank at total pressures up to 100 psig and allowed to mix by diffusion for at least twenty-four hours before utilizing them in the experiments. The shock tube was capable of being pumped to 2×10^{-5} torr before each run with a combined leak/outgas rate of less than 7×10^{-4} torr/minute.

2.3   Experimental Results

Since the rates for vibrational relaxation of HCl in argon are well established[12,13] over a substantial temperature range, the first data were taken on HCl-Ar mixtures for the purpose of calibrating our system. As expected, the time resolved HCl fluorescence behind the incident shock was found to follow a single exponential behavior. Figure 2.3 is a semi-logarithmic plot of the normalized HCl emission intensity versus lab time for a 10% HCl-90% Ar mixture, an initial pressure 7.5 torr, and a shock speed of 1.17 mm/μsec. Fig. 2.4 summarizes the results obtained for a 5% HCl-95% Ar mixture. The data have been reduced to particle relaxation times referenced to a post shock pressure of 1 atmosphere for various post shock temperatures. The large Ar dilution assures an essentially constant post shock temperature during the relaxation. The solid line represents the results obtained by Seery[13] for a similar mixture, and, as can be seen there is good agreement between our data and that of Seery. Data obtained in other HCl-Argon mixtures demonstrated similar good agreement.

With the HCl-Ar runs completed and confidence in our diagnostic system and gas handling procedures established, we proceeded to make shock tube runs for various HCl-H_2-Ar mixtures.

The vibrational energy relaxation equations for a binary gas mixture of harmonic oscillators has been derived previously[14] and will be utilized here without further demonstration. The specific equations used are as follows:

$$- \frac{dX_A}{dt} = \left[\psi/\tau_{AA} + \frac{1 - \psi}{\tau_{AB}} \right] X_A \tag{6}$$

$$- \frac{1 - \psi}{\tau_{AB}^e} \left[\frac{X_B(1 - X_A)}{1 - \exp(-\theta_A)} - \frac{X_A(1 - X_B)}{1 - \exp(-\theta_B)} \right] [1 - \exp(-\theta_A)]$$

and
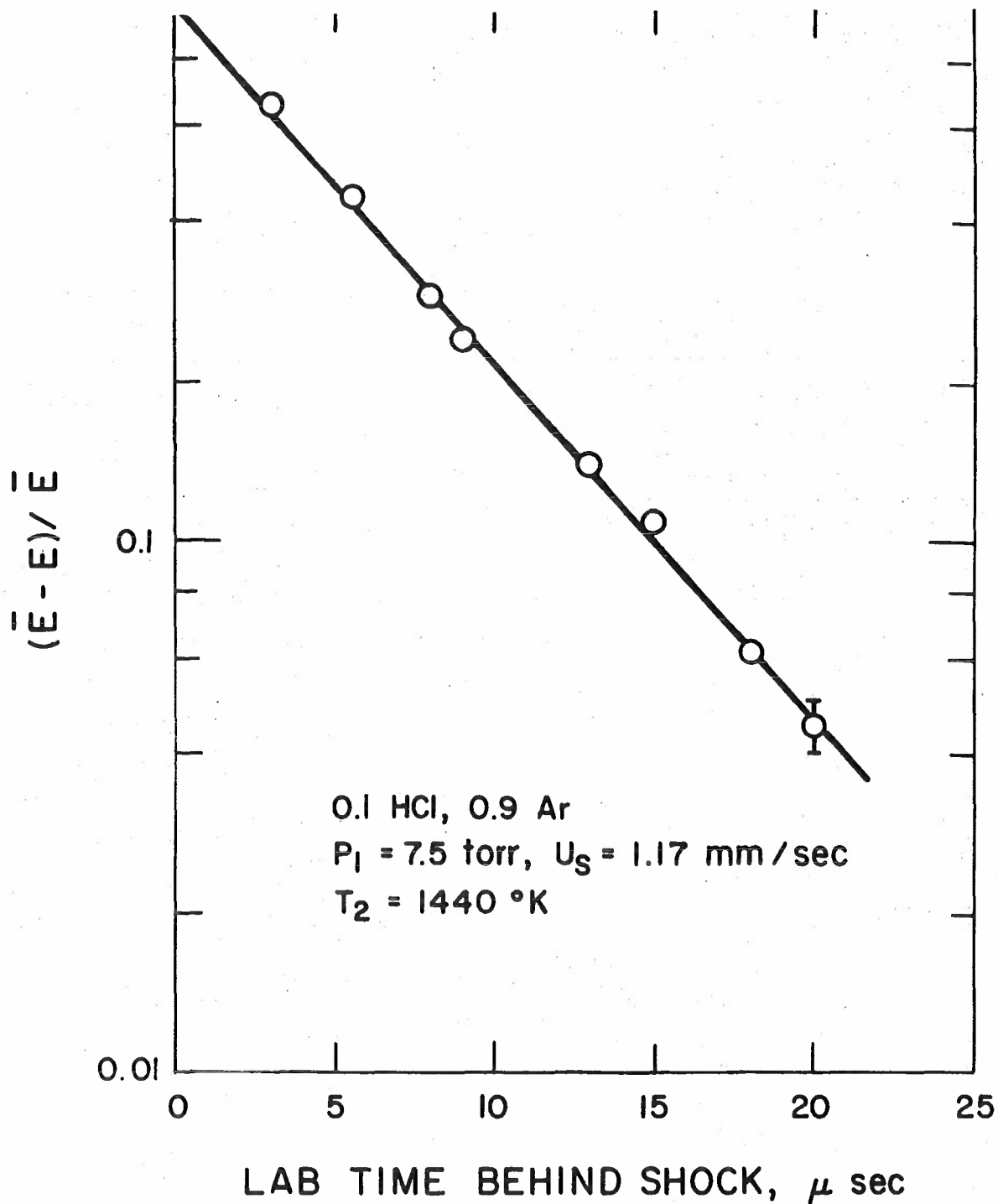
Figure 2.3 HCl-Ar Shock Tube Run. Semilogarithmic Plot of HCl Vibrational Energy Relaxation Behind Shock.
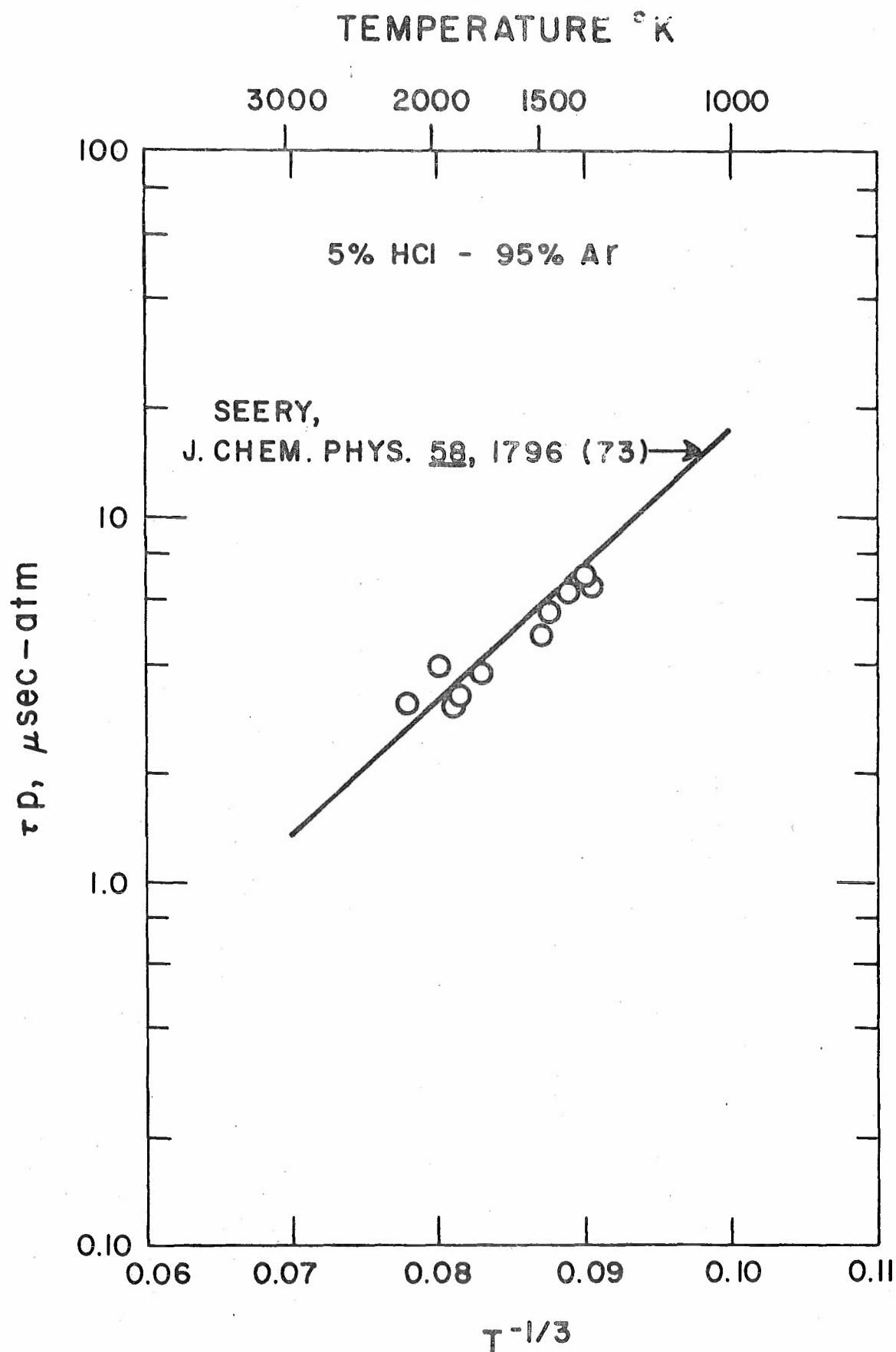
Figure 2.4. Reduced Particle Relaxation Times versus
Temperature for 5% HCl – 95% Ar Mixture

$$-\frac{dX_B}{dt} = \left[\frac{1 - \psi}{\tau_{BB}} + \frac{\psi}{\tau_{BA}} \right] X_B + $$

$$\qquad\qquad\qquad\qquad\qquad\qquad\qquad\qquad\qquad\qquad (7)$$

$$\frac{\psi}{\tau_{AB}^e} \quad \frac{\exp(\theta_B)}{\exp(\theta_A)} \times \left[\frac{X_B(1 - X_A)}{1 - \exp(-\theta_A)} - \frac{X_A(1 - X_B)}{1 - \exp(-\theta_B)} \right] \times [1 - \exp(-\theta_A)]$$

where $X = (\overline{E} - E)/\overline{E}$, $\overline{E}$ is the equilibrium vibrational energy at translational temperature T, and E is the vibrational energy at the local vibrational temperature T_v; ψ and $1 - \psi$ are the mole fractions of species A and B respectively; and $\theta = hc\omega/kT$. Denoting H_2 as species A and HCl as species B, τ_{AA}, τ_{AB}, τ_{BB}, τ_{BA}, τ_{AB}^e would be the characteristic time constants for process (3), (4), (1), (2), and (5), respectively of Table 2.1.

While the above equations may be linearized to provide approximate solutions[15,16], for the present analysis solutions were generated numerically by computer. With input of initial fill pressure, temperature (295°K), gas composition, and incident shock velocity, the computer program calculates the post-shock conditions and, depending on the values chosen for the unknown rate constants, predicts normalized temporal profiles of both the HCl and H_2 vibrational energies following passage of the incident shock.

From a number of initial computer simulation runs of various experimental conditions, it became apparent that determination of the V-V rate for process (5) from the experimentally observed relaxation profiles would require a reasonably accurate prior knowledge of the rate for V-T process (2). Further, it was determined that there was a regime of experimental conditions where the rate for process (2) could be extracted essentially independent of an evaluation of the V-V rate constant, namely, at relatively low H_2/HCl concentration ratios, i.e., 1:1, 2:1 and 3:1, and at the lower end of the experimental temperature range. Under such conditions, energy sharing between HCl and H_2 is minimal and the relaxation profile is only very weakly dependent on the V-V rate. This fact is illustrated by Figure 2.5 which is a calculation of the temporal profile of the HCl vibrational energy behind the incident shock for a 10% HCl-20% H_2-70% Ar mixture at an initial pressure of 10 torr, an incident shock speed of $u_s =$ 1.0 mm/μsec, and a post shock temperature of 915°K. Comparison of the two
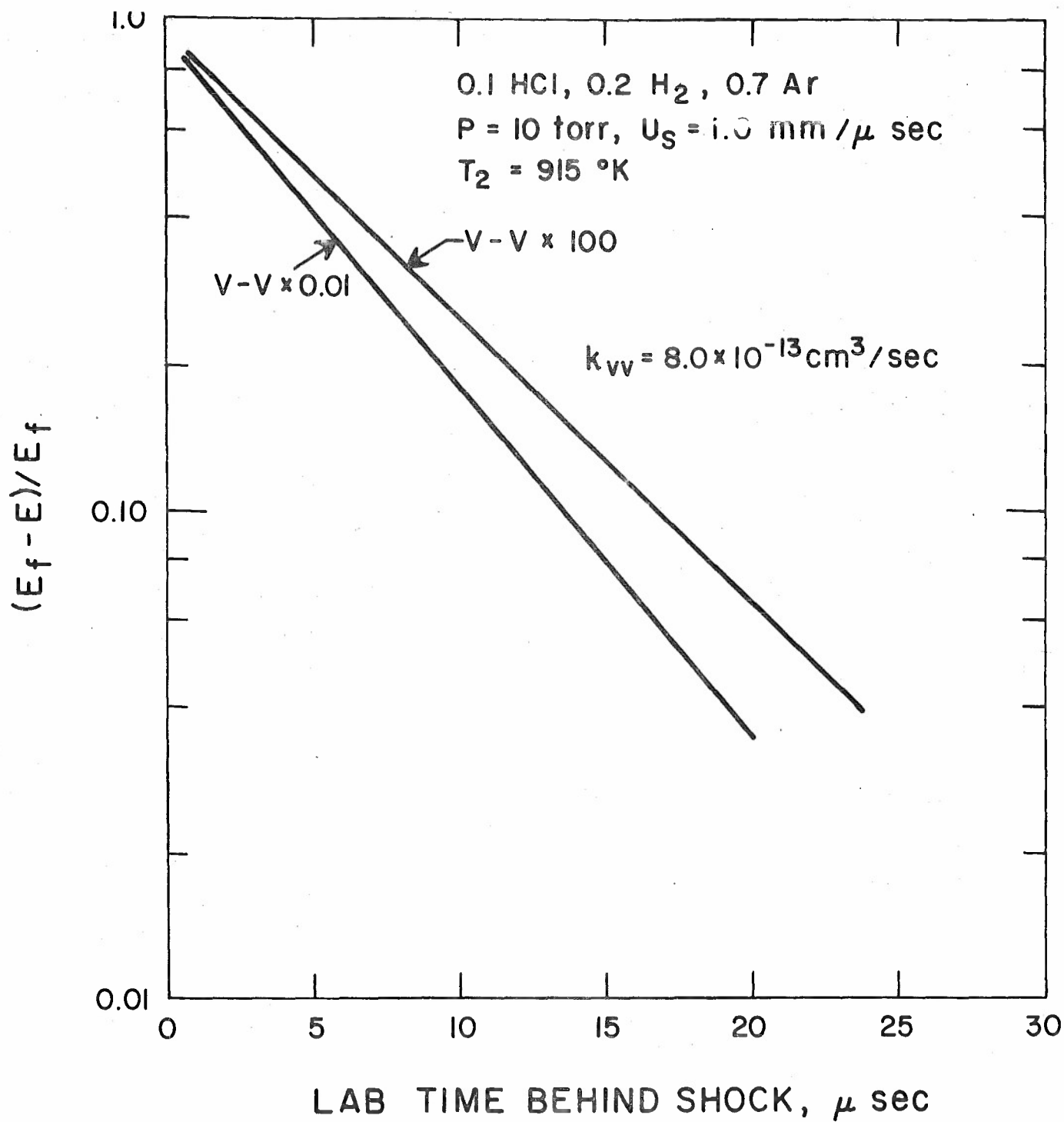
Figure 2.5.   Shock Tube Calculation of HCl Vibrational Energy Relaxa-
tion.   Shows Regime of Temperature and H_2/HCl Concentra-
tion Ratio Where Relaxation is not Sensitive to V-V Rate

- 13 -

calculated curves shows only a small difference in the predicted relaxation behavior even though the assumed V-V rate has been varied a factor of 100 around the baseline theoretical rate.

Such computer stimulations made clear the logical sequence of experiments to be performed to determine both the HCl-H_2 V-T rate and the HCl-H_2 V-V rate. First, runs would be made for mixtures with relatively low H_2/HCl concentration ratios in order to ascertain the rate for V-T process (2). Following an accurate determination of this rate, runs would be made for mixtures of high H_2/HCl concentration, where the relaxation is expected to be strongly dependent on the rate for the V-V coupling process.

A series of data was taken on a mixture of 8.3% HCl-16.7% H_2-75% Ar over a temperature range from 1000°K - 2000°K. Figure 2.1a is a sample oscillogram of one such run. A few of these runs were analyzed for the rate of V-T process (2), and the results are shown as the square data points in Figure 2.6. A curve fit to these results combined with the established room temperature measurement is best described by the expression:

$$k_2 = 2.5 \times 10^{-11} \exp(-55.9/T^{1/3}) \text{ cm}^3/\text{particle}^{-1}\text{-sec}^{-1} \qquad (8)$$

The circles shown on Figure 2.6 represent the data of Bott and Cohen[7] between 300°K and 800°K. On comparing these two independent results, there appears to be a discrepancy. Better agreement between the two sets of data is possible if one takes into account the possible contribution of the H_2-HCl V-V rate process (5) to Bott and Cohen's observed HCl relaxation. Such an anlysis of Bott and Cohen's high temperature data is shown in Figure 2.7 and described later. As can be seen, assuming a combination of a V-V rate based on our theoretical estimate and an HCl-H_2 V-T rate based on the present results extrapolated to 770°K, one can predict a relaxation profile that follows Bott's observed decay quite closely over nearly two e-folding times. While such an interpretationof Bott's data is premature pending the experimental determination of the V-V rate constant, it does provide a preliminary explanation for the apparent discrepancy between the two experiments.
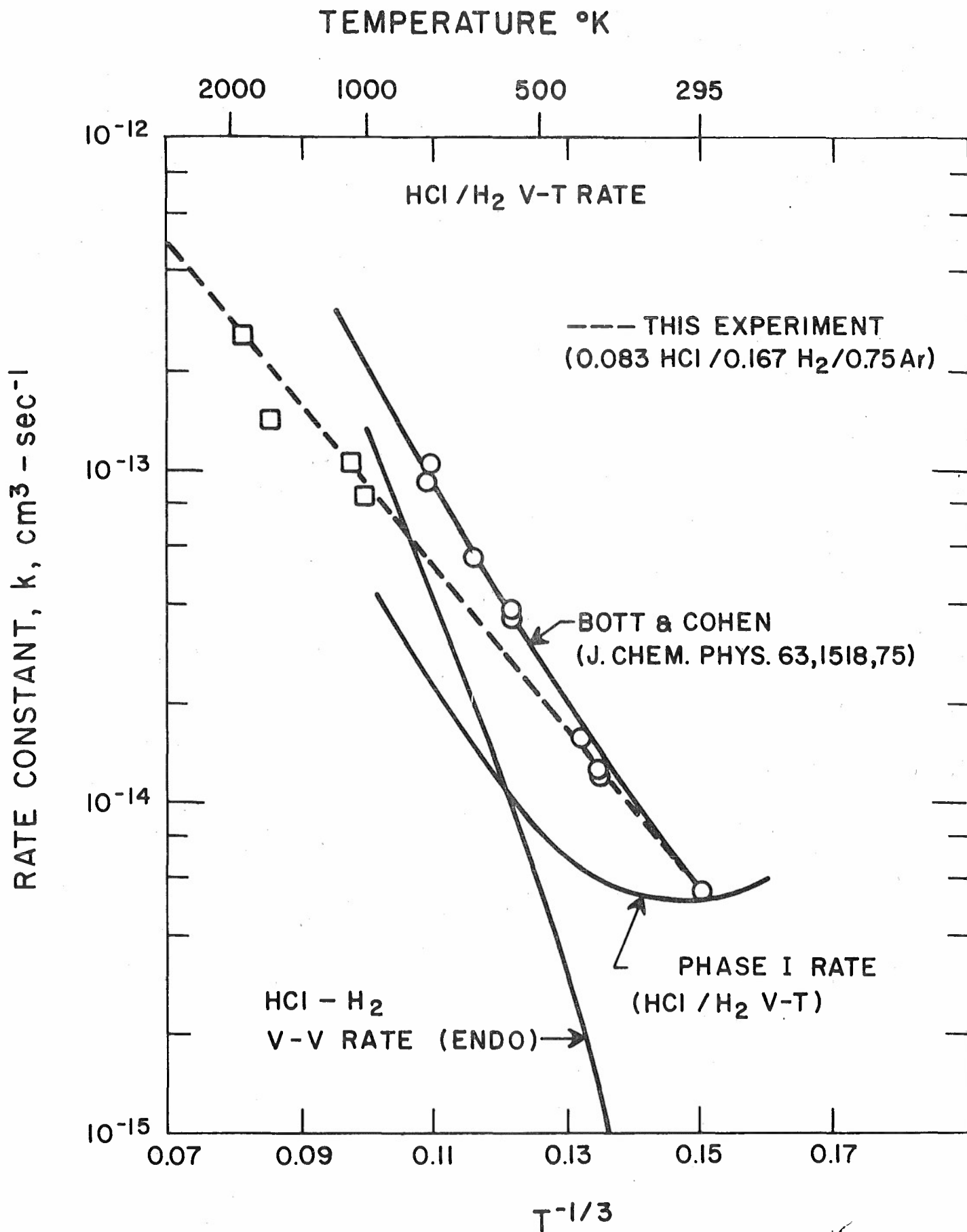
Figure 2.6 Comparison of Present Experimental Data for HC1/H_2 V-T rate with Other Rate Expressions

15
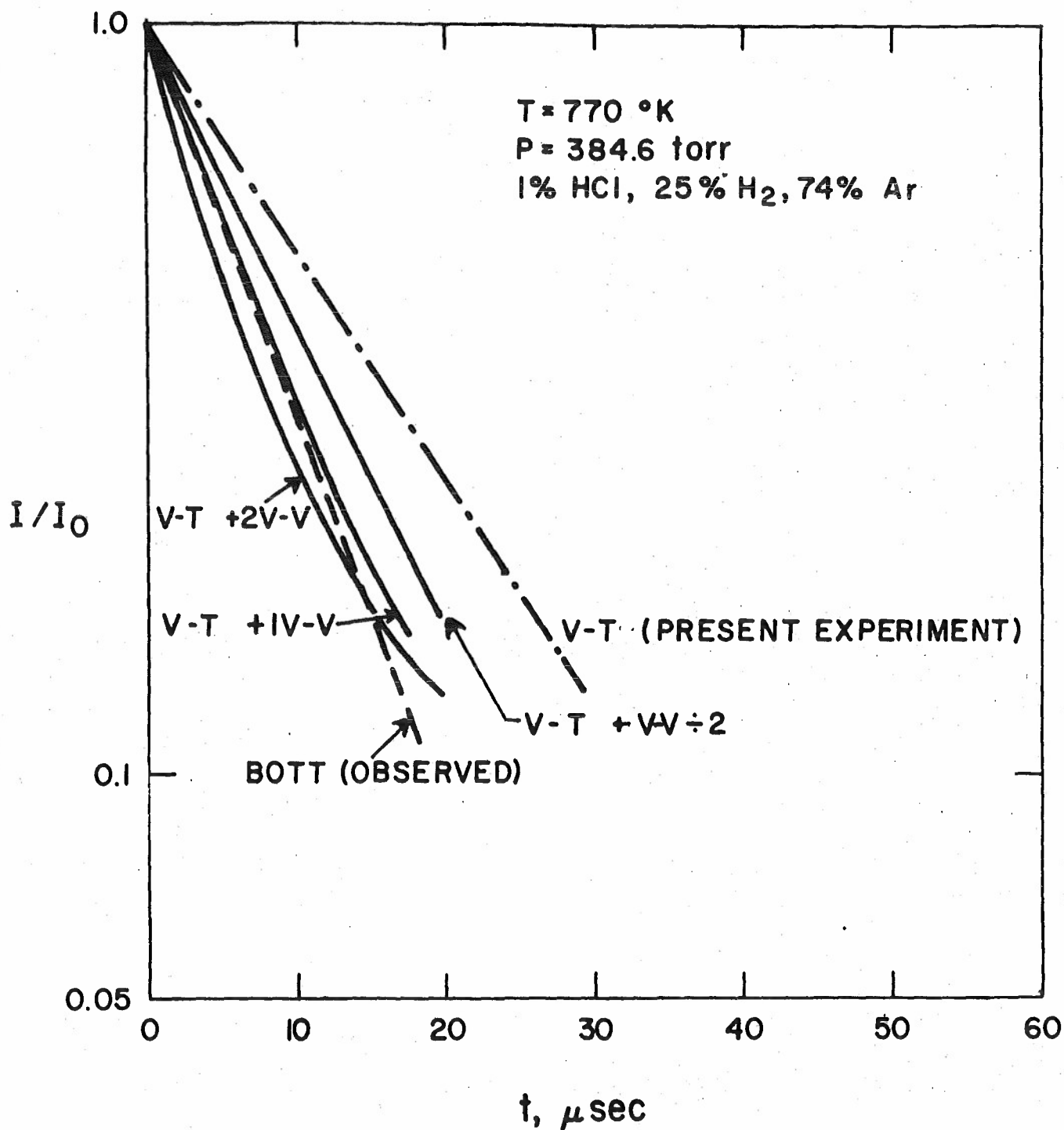
Figure 2.7. Interpretation of Bott's Observed HCl/H_2 Data in Terms of V-V and V-T Processes

Using the value for the HCl-H_2 V-T rate constant established from the present experiment, runs made in mixtures of high H_2/HCl concentration were analyzed to obtain information on the value of the V-V rate constant. Plotted in Figure 2.8 is the intensity data from the oscillogram shown in Figure 2.1b taken in a 3% HCl-57% H_2-40% Ar mixture at a post shock temperature of 1170°K. The solid lines are computed curves for various values of the assumed V-V rate, the baseline value being the theoretically estimated rate expression. The dashed line indicates the relaxation predicted if the contribution from the V-V process were negligible. It is clear that the data plotted in Figure 2.8 indicate a V-V rate constant between 1/5 to 5 times the theoretical baseline value at 1170°K, with the best fit shown being that utilizing the baseline value. Figure 2.9 is another similar plot for a 2.6% HCl-47.4% H_2-50% Ar mixture at a post shock temperature of 1070°K. Again, the solid lines are computed temporal histories for various assumed values of the V-V rate, and the dashed line represents the relaxation profile that would be expected for a negligible contribution from the V-V process. It would appear that the experimental data obtained from this run would best be fit with a value of the V-V rate constant approximately 1/3 of the baseline value. Analysis of other shock tube data taken for mixtures of high H_2/HCl concentrations at various post shock temperatures indicated similar results; that is, the experimental data are best fit with a value of the V-V rate constant between 1/3 to 3 times the theoretically derived baseline value. Determination of the V-V rate constant to better precision will require; (a) a more precise determination of the HCl-H_2 V-T rate constant and, (b) acquisition of more highly resolved data taken for higher H_2/HCl concentration ratios.

An additional test may be applied as a constraint on the value of the V-V rate constant. Using the value for the HCl-H_2 V-T rate obtained from the present experiments, one can analyze the data of Bott and Cohen near 800°k to see what value of the V-V rate constant is required to best fit their data. Presented in Figure 2.7 are the results of such an analysis. The three solid curves shown are predicted temporal profiles of the HCl laser induced fluorescence decay calculated for assumed values of the V-V rate constant of 1/2, 1 and 2 times the baseline theoretical value at 770°K. The dashed curve is the relaxation profile observed by Bott. It is apparent that the data can best
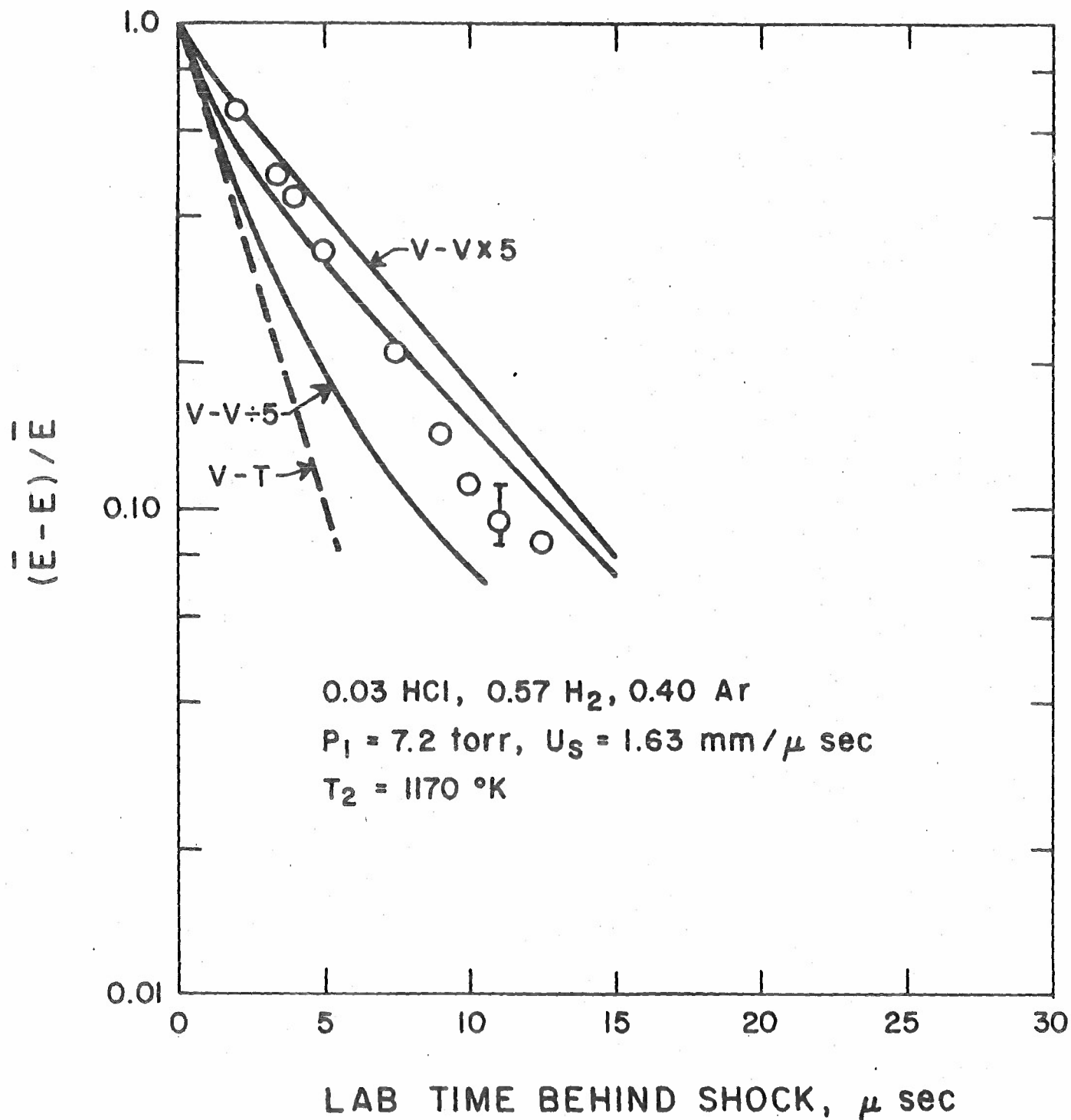
Figure 2.8   Semilogarithmic Plot of Observed
HCl Vibrational Relaxation for
Mixture of High H_2/HCl Concen-
tration Ratio and Comparison with
Calculation for V-V Rate
Determination

- 18 -
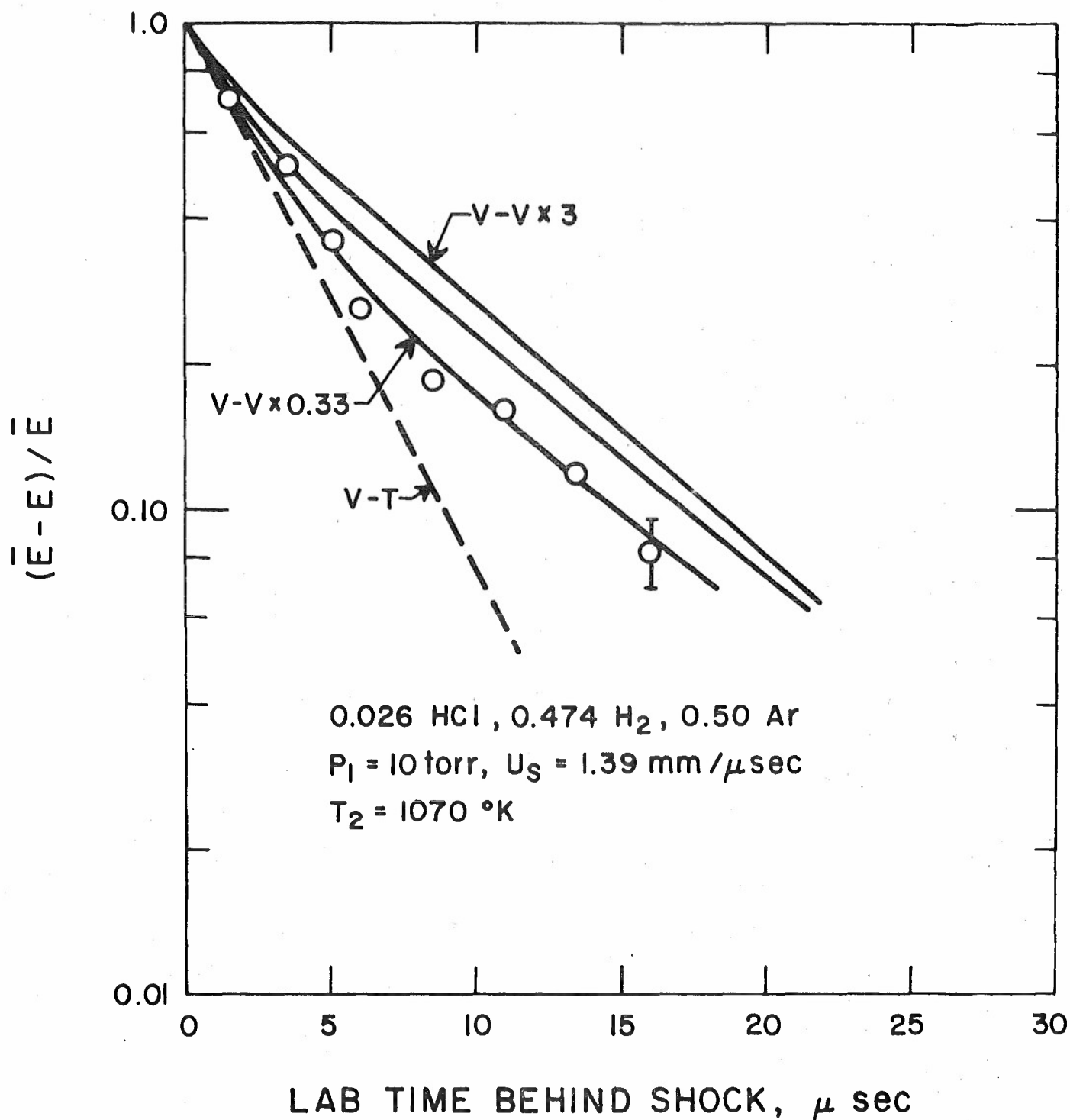
Figure 2.9   Semilogarithmic Plot of Observed
HCl Vibrational Relaxation for
Mixture of High H_2/HCl Concen-
tration Ratio and Comparison with
Calculation for V-V Rate
Determination

- 19 -

be fit with a value for the V-V rate constant very near the baseline value. A similar comparison made with Bott's data taken at $T = 554°K$ is shown in Figure 2.10 and indicates essentially the same result - the data are best fit with a value for the V-V rate constant very near our previously assumed theoretical value. In addition, a recent as yet unpublished, laser fluorescent experiment in a $HF-HCl-H_2$ mixture at room temperature was reported by Bott[27]. Analysis of these data for the rate of the H_2/HCl V→V process yields a value which is within 70% of the base line value at 300°K. Therefore, it is concluded that the present experimental data support our theoretically derived H_2/HCl V→V rate constant from 300 to ~1000°K. Table 2.2 lists the current values of rate constants for the vibrational energy exchange processes for the H_2/HCl system.

2.4   H-Atom Kinetics

In the Phase I investigation the potentially serious performance degradation of atoms, particularly the H-atom, produced in the high temperature stagnation region and subsequently frozen in the rapid expansion, was discussed. At that time only one measurement of HCl (v = 1) deactivation by H-atoms was available[18], and that measurement was at room temperature. Hence, a large and uncertain temperature extrapolation was necessary. Table 2.3 summarizes the previously derived rate expressions for the atomic rate processes.

Early in the current program an unpublished result was brought to our attention* that the rate in reference 18 had been confirmed[20]. Working over the limited temperature range of 200 - 400°K, an activation energy of about 1 kcal/mole had also been determined. This information has been converted into a temperature dependent rate constant and is shown on Figure 2.11 and compared to the rate based on Equation (9) of Table 2.3. Clearly, the data of Glass et al, lead to a steeper temperature dependence and larger rate for temperatures above 300°K. Also shown in Figure 2.11 is the theoretical calculation by R. Wilkens[21], which has been divided by 10. More recently, another measurement at room temperature[19] has provided a further confirmation of the low temperature rate. This result is also shown in Figure 2.11.

*Private communication with Dr. Thomas Barr (USAMICOM)
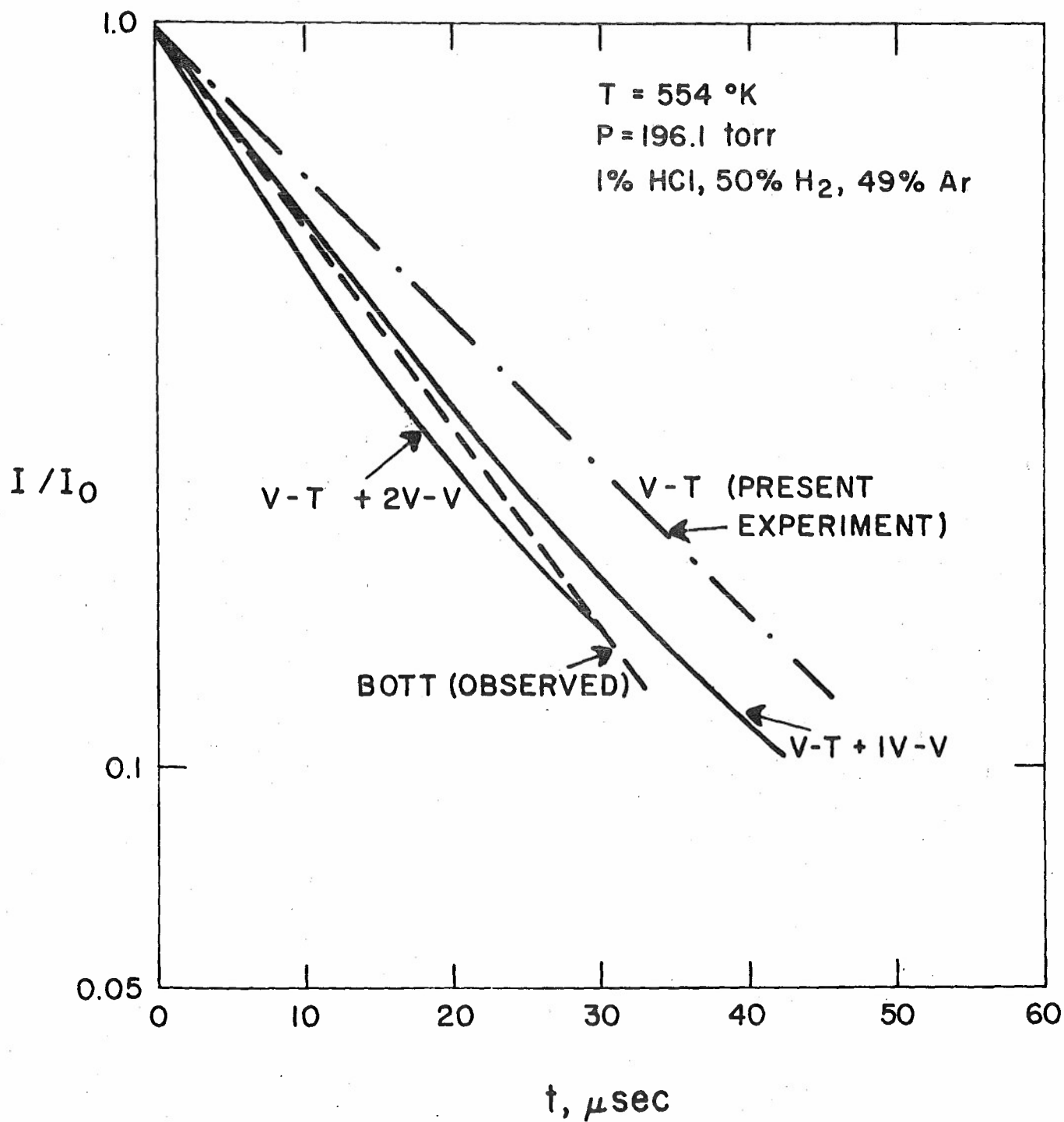
Figure 2.10 Interpretation of Bott's Observed
HCl/H_2 Data in Terms of V-V
and V-T Processes

TABLE 2.2

SUMMARY OF UPDATED VIBRATIONAL RATE CONSTANTS

FOR HARMONIC OSCILLATOR MODEL

$V \to T$ Processes	k ($cm^3 - part^{-1} - sec^{-1}$)
(1) HCl ($v = 1$) + HCl ($v = 0$) $\to$ HCl ($v = 0$) + HCl ($v = 0$)	$k_1 = 4.68 \times 10^{-10} \exp(-76.8T^{-1/3})$ $+ 3.13 \times 10^{-16} \exp(27.9\ T^{-1/3})$
(2) HCl ($v = 1$) + H_2 ($v = 0$) $\to$ HCl ($v = 0$) + H_2 ($v = 0$)	$k_2 = 2.5 \times 10^{-11} \exp(-55.9\ T^{-1/3})$
(3) H_2 ($v = 1$) + H_2 ($v = 0$) $\to$ H_2 ($v = 0$) + H_2 ($v = 0$)	$k_3 = 2.18 \times 10^{-9} \exp(-114.9\ T^{-1/3})$
(4) H_2 ($v = 1$) + HCl ($v = 0$) $\to$ H_2 ($v = 0$) + HCl ($v = 0$)	$k_4 = 4.35 \times 10^{-10} \exp(-114.9T^{-1/3})$

$V \to V$ Process

(5) H_2 9v = 1) + HCl ($v = 0$) $\to$ H_2($v = 0$) + HCl ($v = 1$)	$k_5 = 1.71^{+1.71}_{-0.86} \times 10^{-14}\ T \exp(-30.0\ T^{-1/3})$

TABLE 2.3

VIBRATION RATE CONSTANTS FOR ATOMIC SPECIES FOR

H_2/HCl SYSTEM

(Rate constants in units of cm^3 - particle^{-1} - sec^{-1})

(Rate expressions are for the forward process)

V → T Processes

$$HCl \ (v = 1) + H \ \underset{\leftarrow}{\rightarrow} \ HCl \ (v = 0) + H \qquad (9)$$

$$k = 3.75 \times 10^{-13} \ T^{1/2}$$

$$HCl \ (v = 1) + Cl \ \underset{\leftarrow}{\rightarrow} \ HCl \ (v = 0) + Cl \qquad (17)$$

$$k = 7.50 \times 10^{-13} \ T^{1/2}$$

$$H_2 \ (v = 1) + H \ \underset{\leftarrow}{\rightarrow} \ H_2 \ (v = 0) + H \qquad (18)$$

$$k = 1.73 \times 10^{-14} \ T^{1/2}$$

$$H_2 \ (v = 1) + Cl \ \underset{\leftarrow}{\rightarrow} \ H_2 \ (v = 0) + Cl \qquad (19)$$

$$k = 1.73 \times 10^{-15} \ T^{1/2}$$
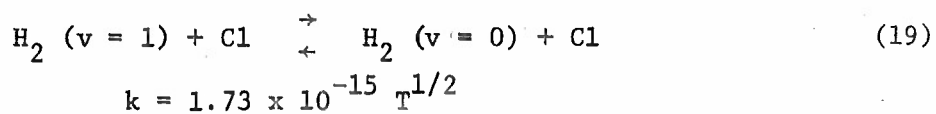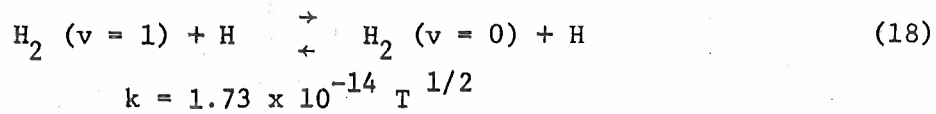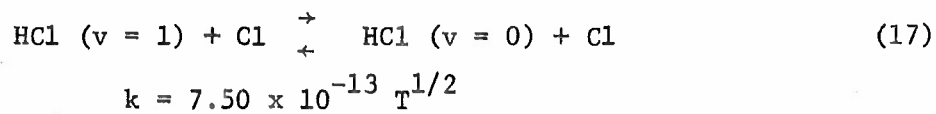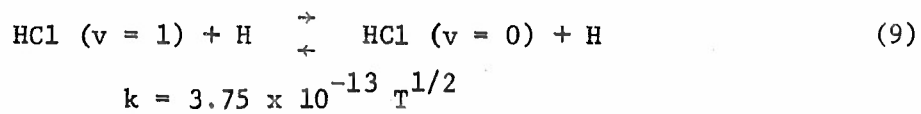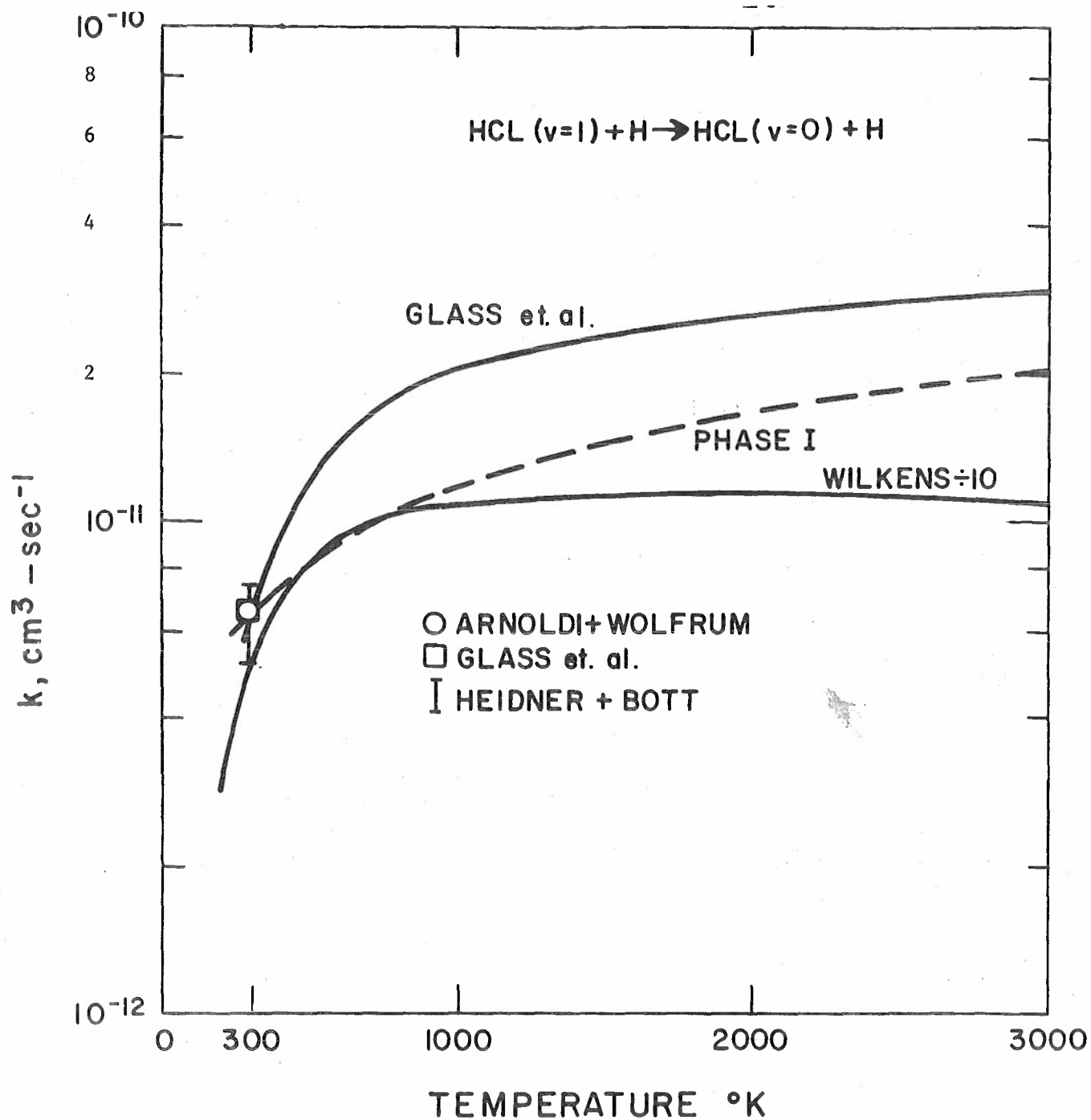
Figure 2.11 Rate of Deactivation of HCl (v = 1)
by H-atoms. Comparison of
Experimental Data, Temperature
Extrapolations, and Theory

Clearly, the data at and around room temperature are in close agreement and support a large rate for the deactivation of HCl (v = 1) by H-atoms. The discrepancy between the measured values for HCl/H and HF/H still exists and requires adequate theoretical explanation. Nevertheless, the large room temperature value of HCl/H combined with the uncertainty in temperature dependence make this process of key importance in understanding potential laser performance. No additional data on the rates of other processes shown in Table 2.2 or 2.3 have become available during this program.

2.5   H-HCl Deactivation Experiment Design

An experiment to measure the rate of H-atom deactivation of HCl for T > 1000°K is shown schematically in Figure 2.12. The basic concept consists in converting the present 1.5 inch diameter shock tube into a glass flow reactor/shock tube. A primary flow of H_2 and Ar will be passed through a microwave discharge and mixed upstream with a secondary flow of HCl external to the shock tube. This mixture will then pass through the shock tube. Flow rates of H_2, Ar, and HCl will be measured using mechanical flow meters. H-atom concentrations will be determined by the standard NOCl titration technique[22]. Once a steady flow of determined concentration is established, fast acting valves will close off the tube, and a shock wave will be initiated. I.R. emission from the HCl will then be monitored behind the incident shock wave using the InSb detector as in the present experiment

In designing the above experiment, various prereactions that might occur in the flow must be considered. These chemical reactions are:

$$H + HCl \; \underset{\leftarrow}{\rightarrow} \; H_2 + Cl \tag{10}$$

$$Cl \; \overset{wall}{\rightarrow} \; 1/2 \; Cl_2 \tag{11}$$

$$H \; \overset{wall}{\rightarrow} \; 1/2 \; H_2 \tag{12}$$

$$H + Cl_2 \; \underset{\leftarrow}{\rightarrow} \; HCl + Cl \tag{13}$$

$$H + H + M \rightarrow H_2 + M \tag{14}$$

$$Cl + Cl + M \rightarrow Cl_2 + M \tag{15}$$

$$H + Cl + M \rightarrow HCl + M \tag{16}$$
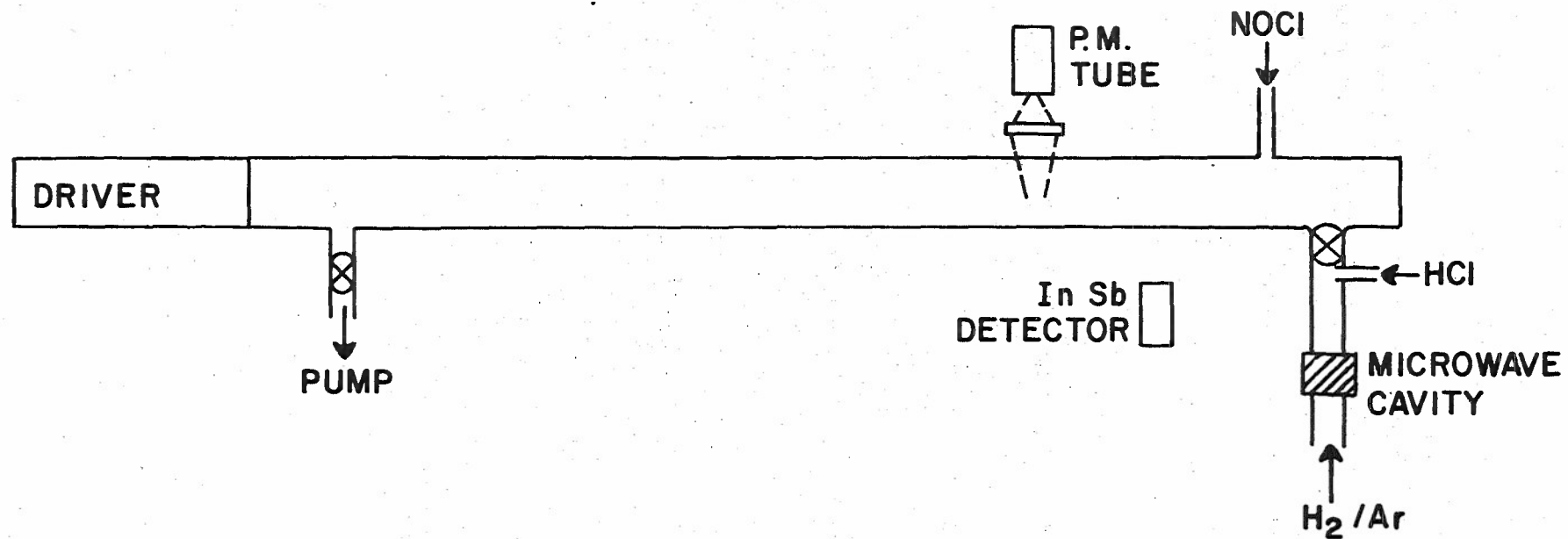
Figure 2.12 Shock Tube Flow Reactor for
H-Atom Deactivation Experiment

Rate constants for these various reactions were obtained and a computer program used to calculate the flow history of the relevant species. Table 2.4 lists the values of the rate constants utilized in the program. For the flow pressures of interest, and wall accomodation coefficients, γ, for H and Cl atoms of less than 10^{-3} [22,23], the rate limiting processes for wall removal of atoms are calculated to be reactions (11) and (12) and not diffusion. See reference (24) for a fuller explanation of the theory of wall effects on active species.

One of the principal results of the above flow kinetics calculations was that even at the lowest HCl concentrations permissible for adequate fluorescence signal and for the fastest flow speeds reasonably attainable through the shock tube, the time constant associated with reaction (10) is expected to be short compared to the flow time between the HCl injector and the test region. Such a situation is undesirable because it produces both a depletion of H-atoms and an undesirable concentration of Cl atoms. Concluding that it is not possible to design a practical shock tube flow experiment to compete with the rapid rate of reaction (10), it was decided to prevent reaction (10) from proceeding too far in the forward direction by operating under conditions where the H_2 concentration is large compared to HCl, and the backward reaction is favored. Shown in Figure 2.13 are the results of a calculation for a pre-shock pressure of 10 torr, an ambient temperature of 300°K, a flow velocity of 10^3 cm/sec, and a mixture of 1% HCl - 33% H_2 - 0.3% H - 65.7% Ar. Plotted are the concentration profiles as a function of flow distance down the tube. As can be seen, for a wall accomodation coefficient, $\gamma = 10^{-5}$ or 10^{-4} (values that can easily be achieved on a properly treated glass wall)[22], the H-atom concentration will remain essentially constant, and there will be negligible formation of Cl-atoms.

Operating in mixtures of high H_2/HCl ratios does, however, present an additional potential problem. The energy sharing between H_2 and HCl due to the V-V process can complicate the interpretation of the effect of H-atom deactivation. That is, if HCl and H_2 are strongly coupled together, does one have to consider the contribution from H-atom deactivation of H_2, as well? Figure 2.14 shows the results of a calculation which indicates an experimental regime where the interpretation of the observed HCl relaxation is essentially independent of the effect of the H on H_2. The calculation

TABLE 2.4

LIST OF RELEVANT RATE CONSTANTS FOR H-ATOM FLOW EXPERIMENT

		Ref.

$H + HCl \overset{\rightarrow}{\leftarrow} H_2 + Cl$ (10) 22,23

$$k_{10} = 5.8 \pm 2.5 \times 10^{-13} \, T^{1/2} \exp \left[(-1450 \pm 150)/T \right]$$

$Cl \overset{wall}{\rightarrow} 1/2 \, Cl_2$ $k = \frac{\gamma \overline{c}}{2r}$; where γ is the wall accomodation   (11)   22
coefficient, $\overline{c}$ is the mean velocity of recom-
bining species, and r is the tube radius.

$H \overset{wall}{\rightarrow} 1/2 \, H_2$ (12) 22,24

$H + Cl_2 \overset{\rightarrow}{\leftarrow} HCl + Cl$ (13) 25

$$k_{13} = 7 \times 10^{-10} \exp (-1500/T)$$

$H + H + M \rightarrow H_2 + M$ (14) 26

$$k_{14} = 4.5 \times 10^{-31} \, T^{-0.7}$$

$Cl + Cl + M \rightarrow Cl_2 + M$ (15) 25

$$k_{15} = 3 \times 10^{-29} \, T^{-1}$$

$H + Cl + M \rightarrow HCl + M$ (16) 25

$$k_{16} = 4 \times 10^{-26} \, T^{-2}$$
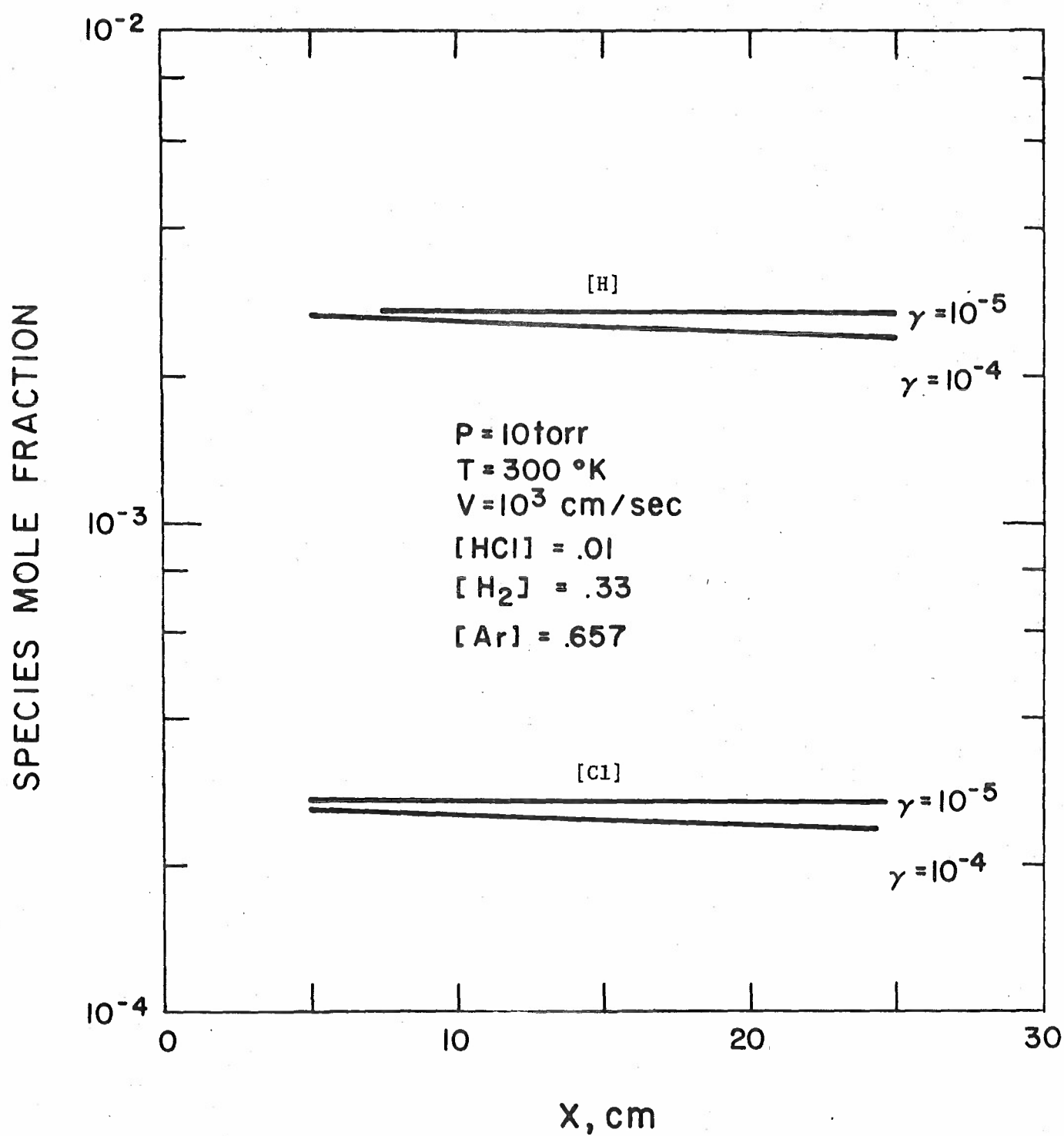
Figure 2.13 Results of Flow Tube Kinetics
Calculation for Design of H-Atom
Deactivation Experiment
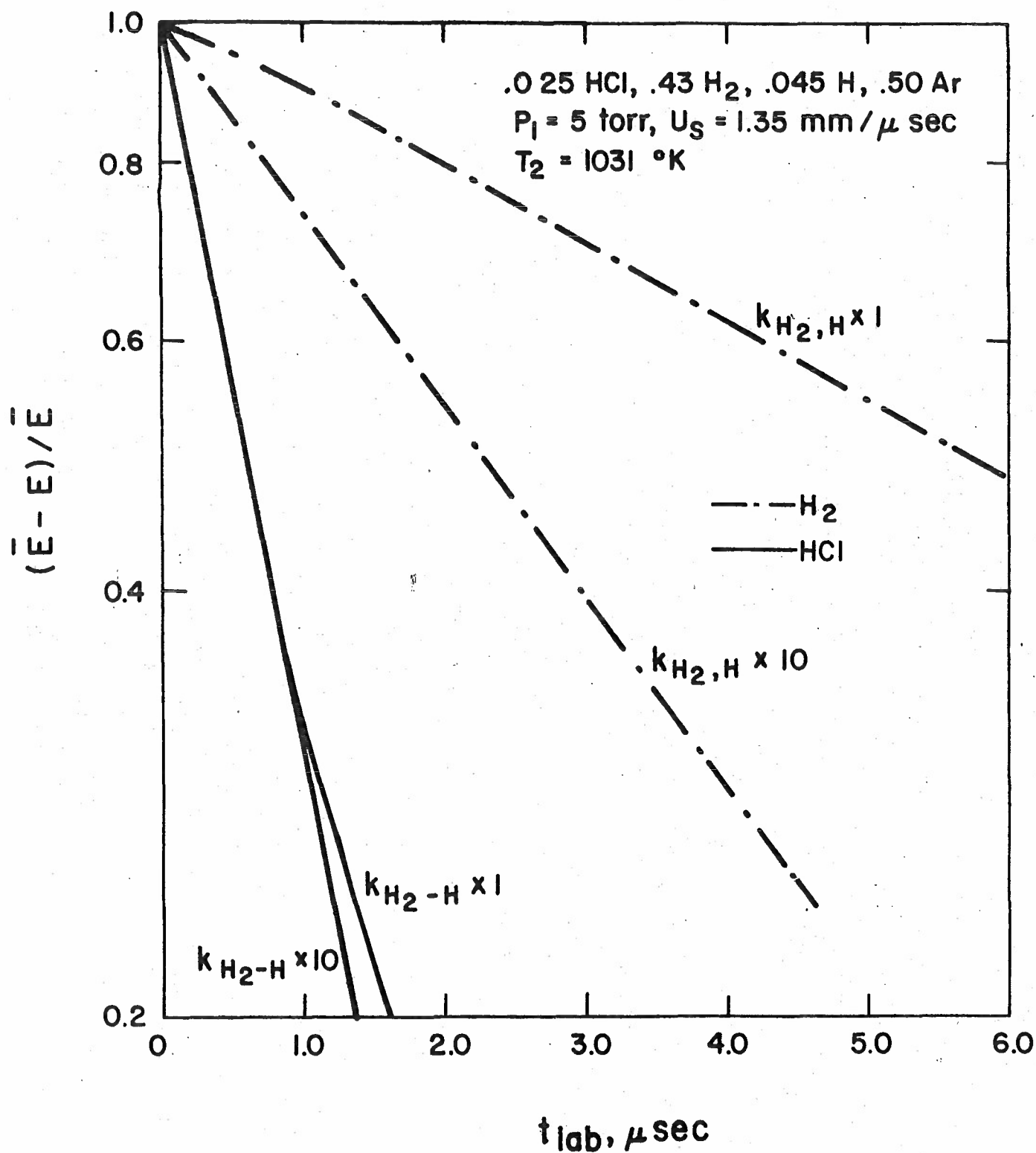
Figure 2.14   Shock Tube Relaxation Calculation
with H-Atoms Showing Decoupling
of HCl and H₂ Relaxation

was performed for an incident shock speed of 1.35 mm/μsec in a 5 torr mixture of 2.5% HCl - 4.5% H - 43% H_2 - 50% Ar. Such conditions yield a post shock temperature of 1030°K. Even at this increased H-atom concentration, calculations indicate that 3 body recombination of H is still slow compared to the pertinent flow time. The two dash-dot curves plotted in Figure 2.13 show the predicted relaxation profile of the H_2 vibrational energy assuming our present base line value for the H_2/H rate[1] (upper curve), and a rate ten times that value (lower curve). The two solid curves plotted show the predicted relaxation of the HCl vibrational energy for, again, an assumed value of the H_2/H deactivation rate equal to our baseline rate, and 10 times that value. Clearly, the value for the rate of H-atom deactivation of H_2 has little effect on the HCl relaxation profile under these conditions. Similar calculations were performed for other conditions, and the conclusion is reached that a determination of the rate for H-atom deactivation of HCl can be made independent of the rate for H-atom deactivation of H_2 provided that the energy sharing between H_2 and HCl is not allowed to progress appreciably. Such a condition can be achieved by operating at the lower shock temperatures and/or creating sufficient H-atom loading to make the V-T processes fast compared to the rate for V-V coupling.

2.6   HCl Spectral Characteristics

Besides the basic kinetic processes discussed above, it was decided to assess two other important parameters used in the modeling - the Einstein coefficients and line broadening cross-sections for HCl. Both of these latter parameters are needed in the calculation of gain and subsequent power extraction.

The experimental data on Einstein coefficients for the fundamental vibration/rotation band of HCl exist for only the lower vibrational levels. Theory must be used to extrapolate these data to the upper levels. The results of two such theoretical extrapolations [28,29] are shown in Figure 2.15. These results are in close agreement at the lower vibrational levels but exhibit an increasing divergence with increasing v. While this descrepancy is of some fundamental importance, its impact on the present laser modeling is small, since the emphasis is on energy extraction from the lower vibrational levels to provide laser wavelengths with good atmospheric transmission. For the present modeling, the Einstein coefficients of Smith[28] are used.

Figure 2.15 Einstein Coefficient for HCl
v → v-1 transitions

Chart axes:
- Y-axis: EINSTEIN COEFFICIENT, $A_{v, v-1}$, sec^{-1}
- X-axis: VIBRATIONAL LEVEL, v

Legend:
○ HERBELIN AND EMANUAL
□ SMITH
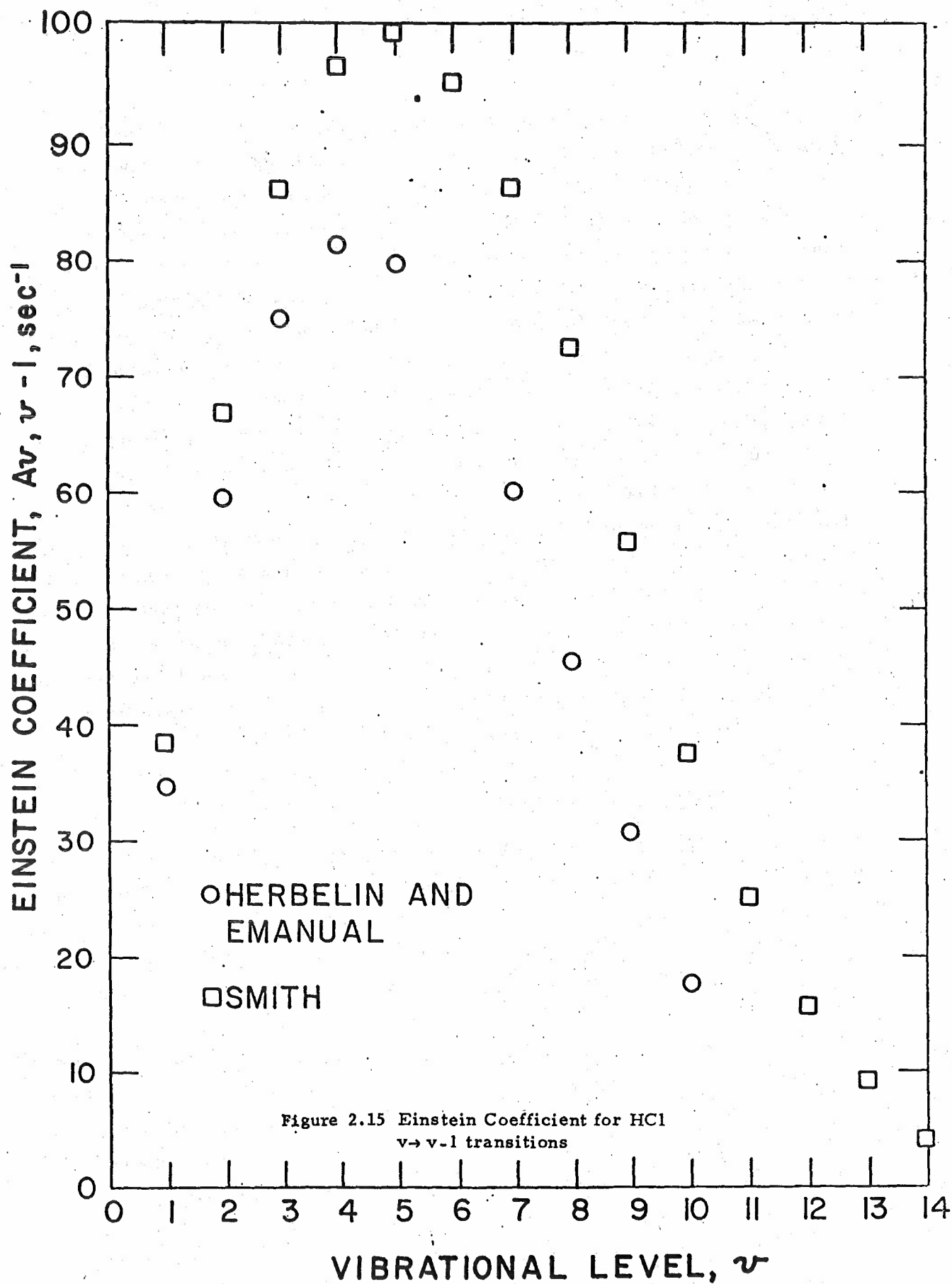
Another important physical parameter required in the laser modeling is the optical broadening cross-section. The experimental data base for HCl is somewhat limited and is shown in Figure 2.16 as the half width, γ, for the P-branch $v = 1 \rightarrow 0$ transition[30,31]. The collision broadening shows an interesting variation with rotational level. This type of variation has also been noted with other hydrogen halides such as HF[32]. Also, the self-broadening (HCl by HCl) is considerably larger than other homonuclear species such as H_2. Finally, the data of these two investigations for similar species are in close agreement. No data exist for the higher vibrational levels of HCl and for higher temperature.

Meredith and co-workers have extensively modeled the optical broadening cross-sections for HF and DF in response to the needs of chemical laser development. For example, they have shown[32] that the cross-section can vary as $T^{-1/2}$ to $T^{-1/4}$ depending upon the type of molecular interaction involved. Lacking this type of theoretical calculation for HCl, we have determined an optical broadening cross-section from the data base of Figure 2.16 and assumed no temperature or vibrational level dependence. For high J transitions ($J > 8$), we have assumed that the cross-section is constant and equal to its value at $J = 8$. Clearly, refinement of those assumptions is necessary as the concept of an H_2/HCl GDL advances.

Figure 2.16 Pressure broadened spectral line
half widths for HCl P-branch
fundamental bands
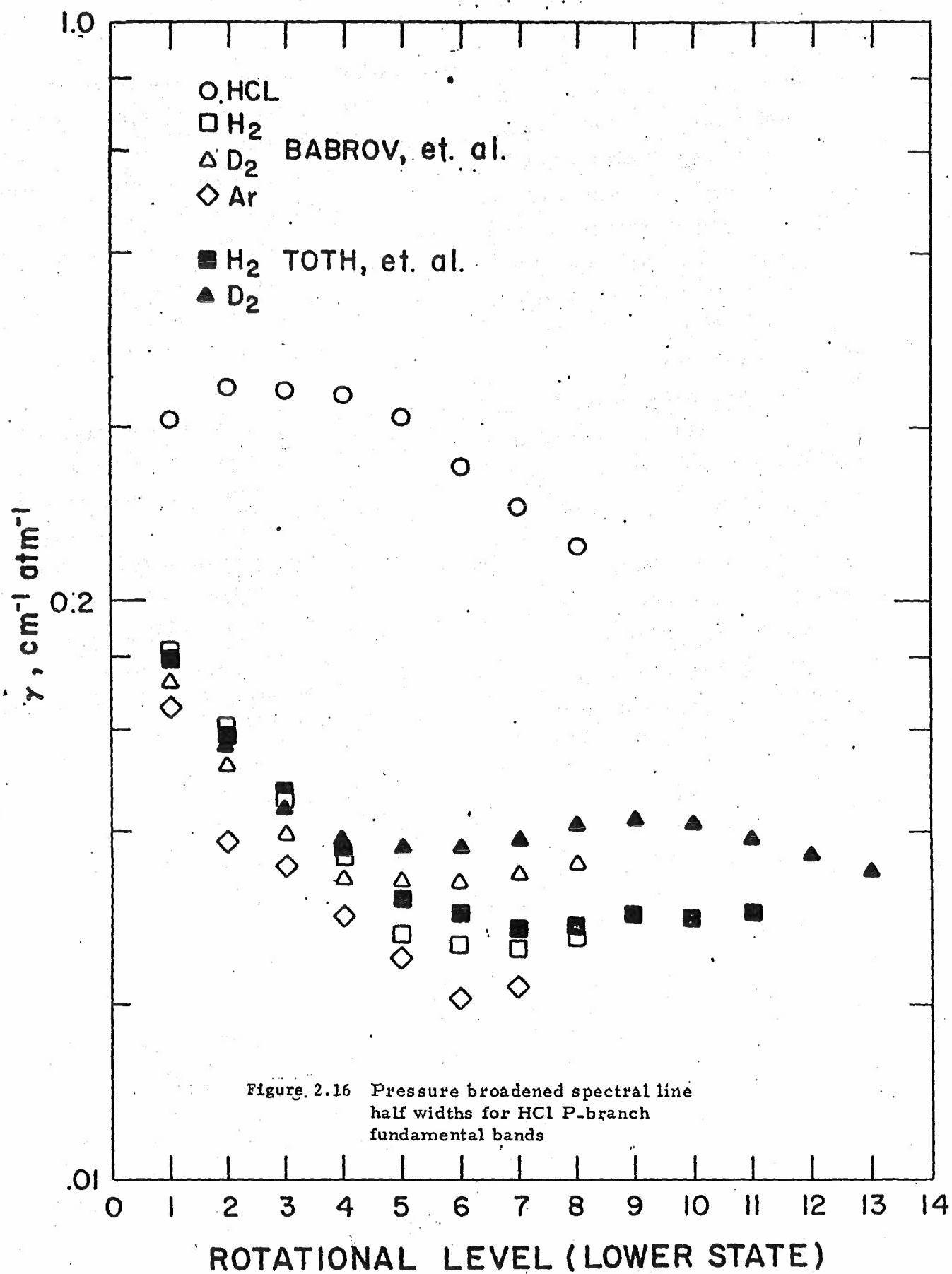
3.0 PROPELLANT DEVELOPMENT

3.1 Objective

The objective of the propellant development is to develop solid propellant gas generators that yield combustion products suitable for use as the working fluid in an advanced H_2-HCl gas dynamic laser. There are certain basic constraints concerning the properties of the combustion products produced by the gas generators. These constraints are enumerated below:

1. **Flame Temperature**

Initially, in Phase I it was believed that the required flame temperature value was 3000°K, but nozzle optimization calculations for available power indicated that a decrease in flame temperature was permissable. In addition, at lower temperatures there are less H-atoms present. As shown in Figure 3.1, H-atoms increase with temperature due to H_2 dissociation. Thus, at a lower temperature the H-atom problem is somewhat alleviated. A parametric study of available power for a range of flame temperatures in the range 2400 to 3000°K indicated 2800°K to be the best compromise value.

2. **Combustion Pressure**

A chamber or combustion pressure of 750 psia was selected. This pressure, and the above flame temperature, are the stagnation values for the working fluid.

3. **Gas Composition**

The molar ratio selected (H_2/HCl) in the combustion products is 97/3. Initially, values as low as 90/10 were considered. More recent results indicate that an optimum (H_2/HCl) value is 97/3 and values as high as 98/2 may be desirable.

4. **Gas Purity (Molar Content)**

The H_2/HCl purity in the combustion products must be >90%. Initially, the requirement was for a best possible value, and hydrocarbons - which are an excellent off-the-shelf source of hydrogen - were considered seriously as propellant ingredients. However, subsequent calculations of the effect of contaminants primarily CO and N_2 on gain coefficient and available power indicated that a relatively pure gas composition for the combustion products is required.

5. Condensed Species

The only way to generate the flame temperatures of interest is by the use of metal fuels (principally Al and Zr). Hydrocarbons are not good fuels because combustion to CO is not energetic enough while combustion in excess of CO yields H_2O, which is detrimental to laser performance. Combustion of Al and Zr results in the production of Al_2O_3 and ZrO_2, both of which are condensed at the flame temperatures and pressure of interest, and must be removed from the combustion products, either by clinker formation or by mechanical means (filtration and/or inertial separation).

6. Weight Yield

The weight yield of the H_2/HCl mixture should be as high as possible by weight of propellant. The results of a preliminary laser systems analysis indicates that a 5% yield is desirable. This 5% yield, however, was not considered to be a hard requirement, and two propellants were developed which were satisfactory and feasible in all respects except with respect to weight yield.

The one propellant ingredient that is necessary to meet all of the above requirements is hydrazine diborane ($B_2N_2H_{10}$ referred to as HDB throughout this report). The compound is available in limited quantities on a special order basis, but synthesis is a straightforward and a well-known process.

Three candidate propellant compositions were developed under this program. The three are pressed compositions comprised of an oxidizer, a fuel, a coolant and a chloride. Candidates are based upon selection of ingredients and computed values of theoretical flame temperature and combustion product composition. For a given set of ingredients, propellant composition is systematically varied to map (H_2 + HCl) weight yield and purity versus the molar ratio (H_2/HCl) within the constraint $T_f = 2800°K$. Candidate compositions were then characterized for safety and ballistic properties and fired in subscale motors. Additionally, various filter arrangements were evaluated to retain condensed combustion products in the motor. The methodology and results of this work are described below.

TABLE 3.1

EQUILIBRIUM YIELD VALUES AND HEATING VALUES @ P_c = 750 PSIA FOR SELECTED PROPELLANT INGREDIENTS

PROPELLANT COMPOSITION, WT % *	Equilibrium Yields, mol/100 gms @ 2800°K			Equilibrium Heating Values, K cal/100 gms, @ T, °K			
	H_2	HCl	Σng	3000	2800	2600	2400
40.467% $N_2H_5NO_3$ + 59.533% ZrH_2	1.685	–	2.351	-19.98	-40.91	-47.98	-54.66
36.402% NH_4NO_3 + 63.598% ZrH_2	1.576	–	2.055	-18.77	-40.13	-46.78	-53.06
38.654% NH_4ClO_4 + 61.346% ZrH_2	1.144	0.3048	1.649	-47.50	-67.44	-73.25	-78.74
63.078% $Zr(OH)_4$ + 36.922% ZrH_2	1.181	–	1.195	52.70	30.48	25.17	20.11
45.025% $ZrO(NO_3)_2 \cdot 2H_2O$ + 54.975% ZrH_2	0.9180	–	1.100	-19.74	-40.82	-45.78	
38.041% $Zr(NO_3)_4 \cdot 5H_2O$ + 61.959% ZrH_2	1.098	–	1.291	-33.73	-55.14	-60.48	
62.375% WO_3 + 37.625% ZrH_2	0.4012	–	0.4059	6.762	-4.599	-7.347	-9.986
57.264% H_2WO_4 + 42.726% ZrH_2	0.6835	–	0.6915	11.74	-1.565	-5.030	-8.334
59.972% NC + 40.028% ZrH_2	1.241	–	2.855	1.287	-15.40	-22.58	-29.42
57.776% TMETN + 42.224% ZrH_2	1.450	–	2.948	-8.813	-26.35	-33.83	-40.94
69.064% NitroGuanidine + 30.936% ZrH_2	1.635	–	3.657	28.75	12.68	4.269	-3.691
32.783% $Al(NO_3)_3 \cdot 9H_2O$ + 67.217% ZrH_2	1.492	–	1.650	-6.505	-29.01		
52.730% $Al(OH)_3$ + 47.270% ZrH_2	1.506	–	1.533	67.03	47.67		

* See Table 3.2 for Glossary of Terms

3.2   Selection of Propellant Ingredients

The propellants are comprised of oxidizer, fuel, coolant and chloride, each ingredient selected on the basis that the constraints of the problem are achieved. Candidate ingredients were selected on the basis of hydrogen content, chemical energy content, commercial availability, ease of use, stability of propellant ingredients and stability of combustion products.

For any given set of propellant ingredients, there is a unique composition that yields the desired values of flame temperature and H_2/HCl composition. To minimize the appearance of H_2O as a combustion product, the stoichiometry of candidate propellants was constrained to an oxidation ratio (O_R) of unity, i.e., the oxygen in the propellant is equal to that required to burn the metals to the metal oxides (ZrO_2, Al_2O_3) and the carbon (if present) to CO. The oxides must be stable with respect to H_2 at the stagnation or chamber conditions to prevent formation of H_2O. The resultant stoichiometry is referred to throughout this report as the OMOX point. Compositions fuel-rich of this stoichiometry are not particularly desirable because metal vapors and suboxides are produced as combustion products, which may interfere with lasing or result in condensed species in the optical cavity.

Equilibrium values of H_2 yield, HCl yield, total gas yield (Σng), and heating value (ΔH_T°) were computed for selected OMOX combustions of:
(1) oxidizer and fuel; (2) coolant and either oxidizer or fuel, and (3) chloride (and fuel if necessary). Calculations were carried out with the ARC equilibrium program using JANAF thermochemical data on an IBM 370/168 computer at assigned values of 750 psia combustion pressure and temperatures of 3000 to 2400°K with 200°K increments. The results of these calculations are given in Table 3.1. The heating values in the table are derived quantities which are defined as the enthalpy at equilibrium of the combustion products at a temperature T and 750 psia less the enthalpy of the propellant. Negative values of ΔH_T° indicate available heat while positive values indicate that heat is required to attain the temperature T. For example, the OMOX composition

$$N_2H_5NO_3 + 1.5 \ ZrH_2 \rightarrow 1.5 \ ZrO_2 + 4H_2 + 1.5 \ N_2$$

is comprised of 40.467% $N_2H_5NO_3$ + 59.533% ZrH_2, (by weight) and has heating

TABLE 3.1
(Continued)
EQUILIBRIUM YIELD VALUES AND HEATING VALUES @ P_c = 750 PSIA FOR SELECTED PROPELLANT INGREDIENTS

PROPELLANT COMPOSITION, WT %	Equilibrium Yields, mol/100 gms @ 2800°K			Equilibrium Heating Values, K cal/100 gms, @ T, °K			
	H_2	HCl	Σng	3000	2800	2600	2400
40.995% $N_2H_5NO_3$ + 59.005% Zr	1.066	–	1.732	-59.96	-79.64	-85.44	-90.99
36.909% NH_4NO_3 + 63.091% Zr	0.9124	–	1.389	-61.49	-86.81	-86.81	-91.88
39.174% NH_4ClO_4 + 60.826% Zr	0.4972	0.3051	1.000	-89.06	-107.7	-112.2	-116.5
63.581% $Zr(OH)_4$ + 36.419% Zr	0.7938	–	0.8031	28.625	7.156		- 1.699
62.886% WO_3 + 37.114% Zr	0.0	–	0.0	-18.15	-28.64	-30.56	-32.45
57.798% H_2WO_4 + 42.202% Zr	0.2300	–	0.2326	-16.54	-28.87	-31.40	-33.87
60.495% NC + 39.505% Zr	0.8233	–	2.446	-25.32	-41.10	-47.42	-53.49
58.308% TMETN + 41.692% Zr	1.011	–	2.517	-36.96	-53.56	-60.15	-66.45
69.529% Nitroguanidine + 30.471% Zr	1.315	–	3.346	8.407	- 6.956	-14.72	-22.09
63.791% $N_2H_5NO_3$ + 36.209% Al	1.657	–	2.700	-89.38	-101.6	-112.8	-123.4
59.734% NH_4NO_3 + 40.266% Zl	1.475	–	2.252	-95.52	-107.2	-118.1	-128.5
62.021% NH_4ClO_4 + 37.979% Al	0.7689	–	1.593	-135.2	-145.7	-155.5	-164.7
74.301% $Al(OH)_3$ + 25.699% Al	1.415	–	1.440	51.79	40.20	29.30	18.84
77.643% H_2WO_4 + 22.357% Al	0.3077	–	0.3131	-20.47	-25.24	-29.82	-34.26
81.573% $Zr(OH)_4$ + 18.427% Al	1.014	–	1.032	38.76	20.63	13.72	7.126

TABLE 3.1
(Continued)

EQUILIBRIUM YIELD VALUES AND HEATING VALUES @ P_c = 750 PSIA FOR SELECTED PROPELLANT INGREDIENTS

PROPELLANT COMPOSITION, WT %	Equilibrium Yields, mol/100 gms @ 2800°K			Equilibrium Heating Values, K cal/100 gms, @ T, °K			
	H_2	HCl	Σng	3000	2800	2600	2400
69.316% $N_2H_5NO_3$ + 30.684% CH_2	3.955	–	7.305	163.8	147.8	133.2	119.5
65.544% NH_4NO_3 + 34.456% CH_2	4.038	–	7.383	188.7	172.4	157.7	143.8
67.680% NH_4ClO_4 + 32.320% CH_2	3.129	0.5697	6.353	125.5	111.4	98.54	86.61
85.022% $Zr(OH)_4$ + 14.978% CH_2	2.114		3.214	167.9	147.5	139.1	131.1
84.638% WO_3 + 15.362% CH_2	1.082	–	2.196	108.4	102.9	97.92	93.21
81.662% H_2WO_4 + 18.338% CH_2	1.616	–	2.950	135.2	128.1	121.6	115.5
73.134% $ZrO(NO_3)_2 \cdot 2H_2O$ + 26.866% CH_2	2.428	–	4.660	141.5	124.6	114.3	
67.112% $Zr(NO_3)_4 \cdot 5H_2O$ + 32.888% CH_2	3.074	–	5.804	154.0	136.4	124.2	
68.857% $N_2H_5NO_3$ + 31.143% HTPB	3.414	–	6.796	138.0	123.1	109.6	96.92
65.056% NH_4NO_3 + 34.944% HTPB	3.430	–	6.812	159.4	144.6	131.0	118.3
67.208% NH_4ClO_4 + 32.792% HTPB	2.565	0.5654	5.824	98.54	85.75	73.96	63.03

TABLE 3.1
(Continued)
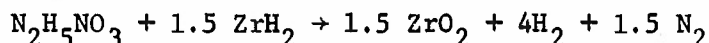EQUILIBRIUM YIELD VALUES AND HEATING VALUES @ P_c = 750 PSIA FOR SELECTED PROPELLANT INGREDIENTS

PROPELLANT COMPOSITION, WT %	Equilibrium Yields, mol/100 gms @ 2800°K			Equilibrium Heating Values, K cal/100 gms, @ T, °K			
	H_2	HCl	Σng	3000	2800	2600	2400
29.465% NH_4NO_3 + 70.525% PEG 200	3.949	–	7.299	183.5	167.4	152.8	139.1
31.493% NH_4ClO_4 + 68.507% PEG 200	3.530	0.2652	6.823	154.2	139.2	125.4	112.6
52.223% NC + 47.777% PEG 200	2.894	–	6.306	135.7	122.0	109.5	97.77
49.957% TMETN + 50.043% PEG 200	3.153	–	6.550	133.3	119.1	106.1	93.84
61.959% Nitroguanidine + 38.041% PEG 200	2.907	–	6.319	132.9	119.2	106.7	94.95
55.552% NH_4NO_3 + 44.448% TCE	1.360	–	4.863	63.21	53.10	43.68	34.73
57.910% NH_4ClO_4 + 42.090% TCE	0.7264	0.4838	4.115	45.22	36.49	28.41	20.77
76.589% NC + 23.411% TCE	1.038	–	4.558	49.93	40.58	31.81	23.44
74.923% TMETN + 25.077% TCE	1.294	–	4.800	40.37	30.40	21.11	12.27
100% NH_4Cl	2.791	1.849	5.641	227.6	214.4	202.7	192.0
100% N_2H_5Cl	2.903	1.444	5.870	169.1	155.6		
100% HDB	8.200	–	8.546	227.7	128.9	87.65	59.99

TABLE 3.1
(Continued)

EQUILIBRIUM YIELD VALUES AND HEATING VALUES @ P_c = 750 PSIA FOR SELECTED PROPELLANT INGREDIENTS

PROPELLANT COMPOSITION, WT %	Equilibrium Yields, mol/100 gms @ 2800°K			Equilibrium Heating Values, K cal/100 gms, @ T, °K			
	H_2	HCl	Σng	3000	2800	2600	2400
79.923% $Zr(OH)_4$ + 20.077% AlH_3	1.988	–	2.023	64.16	42.60	34.52	26.07
57.154% NH_4NO_3 + 42.846% AlH_3	3.532	–	4.313	-37.62	-54.82	-70.16	-84.34
79.439% WO_3 + 20.561% AlH_3	1.018	–	1.036	4.110	- 2.143	- 7.844	-13.19
75.745% H_2WO_4 + 24.255% AlH_3	1.501	–	1.527	10.45	2.422	- 4.823	-11.56
61.303% $N_2H_5NO_3$ + 38.697% AlH_3	3.508	–	4.544	-37.31	-54.44	-69.68	-83.75
59.489% NH_4ClO_4 + 40.511% AlH_3	2.727	0.4244	3.578	-77.42	-93.34	-107.74	-120.99
72.221% $Al(OH)_3$ + 27.779% AlH_3	2.750	–	2.799	85.18	70.05	56.26	43.34

TABLE 3.2
GLOSSARY OF CANDIDATE PROPELLANT INGREDIENTS

INGREDIENT	Chemical Formula or Acronym
A. OXIDIZER	
1. Hydrazine Nitrate	$N_2H_5NO_3$
2. Ammonium Nitrate	NH_4NO_3
3. Ammonium Perchlorate	NH_4ClO_4
4. Tungsten Oxide	WO_3
5. Tungstic Acid	H_2WO_4
6. Zirconyl Nitrate Dihydrate	$ZrO(NO_3)_2 \cdot 2H_2O$
7. Zirconium (IV) Nitrate Pentahydrate	$Zr(NO_3)_4 \cdot 5H_2O$
8. Nitrocellulose (A Resin used in Solid Propellant Binders)	NC
9. Trimethylolethane Trinitrate (A co-plasticizer for Nitrocellulose)	TMETN
B. FUELS	
1. Zirconium	Zr
2. Zirconium Hydride	ZrH_2
3. Aluminum	Al
4. Aluminum Hydride	AlH_3
5. Tetracyanoethylene (A High-energy Organic Compound, $C_2(CN)_4$)	TCE
C. COOLANTS	
1. Zirconium (IV) Hydroxide	$Zr(OH)_4$
2. Aluminum Hydroxide	$Al(OH)_3$
3. Hydrazine Diborane ($B_2N_2H_{10}$)	HDB
4. Polyethylene, Wax, or Long-chain Hydrocarbon	CH_2

TABLE 3.2

(GLOSSARY OF CANDIDATE PROPELLANT INGREDIENTS - CONTINUED)

Ingredient	Chemical Formula or Acronym
5. Hydroxy Terminated Polybutadiene (An Isocyanate-cured Polyurethane Binder System Widely used in the Propellant Industry)	HTPB
6. Polyethylene Glycol with a Molecular Weight of 200 a.m.u.	PEG-200
7. Nitroguanidine	

D. CHLORIDES

1.	Ammonium Chloride	NH_4Cl
2.	Hydrazine Chloride	N_2H_5Cl
3.	Zirconium (IV) Chloride	$ZrCl_4$

values, ΔH_T^o = -19.98, -40.91, -47.98 and -54.66 Kcal/100 gm @ 3000, 2800, 2600 and 2400°K, respectively. These heating values indicate the heat available at the indicated temperature. Similarly, the OMOX composition

$$Zr(OH)_4 + ZrH_2 \rightarrow 2\ ZrO_2 + 3\ H_2$$
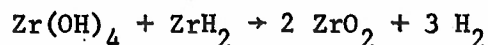
is comprised of 63.078% $Zr(OH)_4$ + 36.922% ZrH_2 (by weight) and has heating values of 52.70, 30.48, 25.17 and 20.17 Kcal/100 gm at 3000, 2800, 2600 and 2400°K, respectively, indicating that heat is required to attain these temperatures. Note that in the above two examples the discontinuity in ΔH_T^o vs temperature between 2800°K and 3000°K. This is due to the heat of fusion of ZrO_2, which takes place at 2950°K. Note that the tabulated values of H_2, HCl and Σng are equilibrium values at 2800°K, not the stoichiometric values expressed above. The two do not differ much, especially at the lower temperatures and differ primarily due to H_2 dissociation.

The results in Table 3.1 are discussed in terms of H_2 yield, H_2 yield purity (H_2/Σng), heat release and oxygen content (of oxidizers). At the start of the program, H_2 yield was held most important and the effort was directed primarily toward maximizing this parameter. For this reason organic propellant ingredients were initially favored. Later on in the program, it became apparent that contaminants such as CO greatly reduce lasing performance, and for this reason the effort was redirected toward maximizing H_2 yield at values of H_2 yield purity >95% and the use of organics was eliminated. Heat release and oxygen content of oxidizers are most important when high-H_2-content compounds such as HDB or AlH_3 are used in the propellants. Salient features of the results in Table 3.1 are discussed below.

3.2.1   Oxidizers

In terms of H_2 yield the ingredients that generate the most H_2 in descending order are $N_2H_5NO_3$ > NH_4NO_3 > NH_4ClO_4 > H_2WO_4 > WO_3. In addition to the above there are other oxidizers which are less effective than NH_4NO_3 and are valued in the order $Al(NO_3)_3 \cdot 9H_2O$ > TMETN > NC > NH_4ClO_4 > $Zr(NO_3)_4 \cdot 5H_2O$ > $ZrO(NO_3)_2 \cdot 2H_2O$ > H_2WO_4. In terms of gas purity of H_2 yield (H_2/Σng), H_2WO_4 = WO_3 > NH_4ClO_4 > NH_4NO_3 > $N_2H_5NO_3$; in terms of heating value, NH_4ClO_4 > NH_4NO_3 > $N_2H_5NO_3$ > WO_3 > H_2WO_4, and in terms of oxygen content, NH_4NO_3 > NH_4ClO_4 > $N_2H_5NO_3$ > H_2WO_4 > WO_3.

All of these oxidizers are commercially available and relatively easy to use, although both non-metallic nitrates require specially-dried processing facilities (relative humidity <50% at 70°F) for use. Of the two nitrates, $N_2H_5NO_3$ is preferred because this compound does not undergo a low-temperature phase transition as does NH_4NO_3. Both of the nitrates, as well as NH_4ClO_4 yield substantial amounts of N_2 as a combustion product, which is a contaminant. This problem, however, is not severe with NH_4ClO_4 because typically only small amounts of this oxidizer are used in any given composition due to the constraint $H_2/HCl = 97/3$. Best (H_2 + HCl) purity values are obtained by use of either WO_3 or H_2WO_4 with hydrogen-containing fuels, coolants and chlorides. Both of these oxidizers yield the metal W(c) (condensed phase) as a combustion product which can be filtered out or retained in the motor, to prevent contamination of the working fluid. Tungsten is thermodynamically stable at the temperatures of interest (2800°K) with respect to H_2, HCl, and metal oxides, so that contamination of the working fluid with tungsten reaction products is not a problem. Other possible oxidizers include aluminum nitrate, $Al(NO_3)_3 \cdot 9H_2O$, zirconium nitrate, $Zr(NO_3)_2 \cdot 5H_2O$ and zirconyl nitrate, $ZrO(NO_3)_2 \cdot 2N_2O$. The best of these is Al-nitrate, yielding 2.4 mols H_2/100 gm, which is seen to be inferior to both $N_2H_5NO_3$ and NH_4NO_3. The use of hydrates as propellant ingredients is not good practice. The organic oxidizers, NC and TMETN, received only minor attention here because contamination of the H_2 yield with CO and N_2 is significant. Calcium and magnesium nitrates were not considered because of the instability at 2800°K of CaO(c) and MgO(c), which are major combustion products of these oxidizers. Both oxides react significantly with H_2 and HCl at high temperatures to yield H_2O and other contaminants (Ca, Mg, CaOH, MgOH, CaCl, $CaCl_2$, $MgCl_2$). Similarly, the other alkaline earth nitrates, $Sr(NO_3)_2$ and $Ba(NO_3)_2$, which are well-known oxidizers used in colored flare signals, are not considered usable here. Alkali metal nitrates and perchlorates (e.g., $NaNO_3$, $CaClO_4$, KNO_3, etc.) yield the chlorides quantitatively in combustion products. These species, although gaseous at stagnation or chamber conditions, would condense in the cavity and for this reason these oxidizers are not considered as propellant ingredient candidates.

3.2.2 Fuels

As mentioned previously, hydrocarbons are not desirable as fuels, because combustion to CO is not energetic enough to yield a flame temperature of 2800°K, and combustion to CO_2 yields H_2O due to the water-gas reaction. For the attainment of high temperature without H_2O contamination, metallic fuels must be employed.

In terms of H_2 yield, $AlH_3 > ZrH_2 > Al > Zr$; in terms of H_2 yield purity, $AlH_3 > ZrH_2 > Al = Zr$, and in terms of heating value, $Al > Zr > ZlH_3 > ZrH_2$. Since AlH_3 has stability and sensitivity problems, it is not a viable candidate. Consequently, the value of the fuels in propellant compositions is considered primarily as the source of energy rather than of H_2. Either ZrH_2 or Zr are favored in preference to Al. This is because ZrO_2, the major Zr combustion product at the OMOX point, is thermodynamically more stable than Al_2O_3. Even though the use of Al compares favorably with Zr and ZrH_2 in terms of H_2 yield purity, Al_2O_3 dissociates somewhat and reacts with H_2O as a combustion product. In Zr-containing propellants, the H_2/H_2O molar ratio is ∿250, but is only ∿80 in the combustion products of propellants containing Al. The additional effect of this phenomenon on the combustion products composition at throat conditions is discussed in Section 3.3.

For reasons stated previously, due to CaO and MgO stability, neither CaH_2 nor MgH_2 were considered as fuels.

3.2.3 Coolants

The combustion of stoichiometric mixtures of candidate oxidizers and fuels yields values of flame temperature greater than 2800°K. In order to reduce the flame temperature to 2800°K, coolants are required and those of choice include $Zr(OH)_4$, $Al(OH)_3$, $(CH_2)_2$ and HDB. Stoichiometric mixtures of the hydroxides with candidate fuels serve as coolants to obtain a flame temperature of 2800°K, and yield H_2 as the only gaseous combustion product. The as-received form of $Zr(OH)_4$ is the hydrate $Zr(OH)_4 \cdot nH_2O$ (n = 4 to 5) which must be dried carefully prior to use (48 hours at 145°F in a forced-draft oven has been found to be satisfactory). Care must be used because excessive drying at too high a temperature drives the as-received product to ZrO_2.

Stoichiometric mixtures of $(CH_2)n$ and candidate oxidizers are coolants if the oxidation ratio (O_R) of the mixture, defined as the molar ratio of oxygen to carbon, is unity. At values of $O_R < 1$, soot and hydrocarbon (HC) fragments (CH, CH_2, CH_3, CH_4, etc.) appear as combustion products, while at $O_R > 1$, CO_2 and H_2O appear as combustion products. Note that while the H_2 yield of $(CH_2)n$ is second only to HDB in terms of mols/100 gm, the molar purity of the H_2 yield, assuming $C \rightarrow CO$ is only 50%, ($CH_2 \rightarrow CO + H_2$, $H_2/(H_2 + CO)$ = 1/2). Because of the high degree of purity required, the use of hydrocarbons in candidate propellants was given only minor consideration. The purity effect can be minimized by using the hydrocarbon in propellants containing no oxygen for burning the carbon. However, soot and HC fragments would result. It is possible to filter out the soot, depending on the ability of the composition to form a clinker on combustion (if the composition does not clink, the soot will be generated as angstrom-sized particles and aggomerates thereof, which will probably be very difficult to remove). Due to this and the unknown effect that HC fragments would have on gain and available power, hydrocarbons were ruled out.

Of the three coolants, only HDB is not commercially available in large quantities. However, synthesis of this compound is straight forward and results in a product of good yield and high purity. It is the best H_2 gas generator ingredient of all the candidate ingredients. It is capable of self-sustained combustion, with an adiabatic flame temperature of 1877°K ($B_2N_2H_2 \rightarrow 5H_2 + 2BN(c)$). The compound is not a good candidate for systems of flame temperature equal to 3000°K because of significant dissociation of BN(c) at this temperature, and subsequent recombination in the throat, resulting in a dirty dust-laden working fluid. However, BN(c) is essentially undissociated at 2800°K and the H_2 yield is essentially clean. HDB is a fairly reactive solid, and has exhibited chemical incompatibility with many propellant ingredients of interest. Storage and use is limited to very dry facilities (<40% relative humidity at 70°F). Its use with NH_4ClO_4 may result in explosions on ignition, though this seems to be a phenomenon dependent on HDB purity and the absolute and relative contents of each component in the propellant composition.

The oxidizers and the coolants are the primary H_2 sources in the propellants. The requirement (see Section 3.1) that (H_2 + HCl) yield be >5% by weight @ (H_2/HCl) = 97/3 (molar) dictates that the H_2 yield values as tabulated in Table 3.1) be >1.59 mol/100 gm of propellant. Disregarding the organics and AlH_3, it is seen that the only oxidizer-fuel combinations that

qualify are $N_2H_5NO_3$ + either ZrH_2 or Al. The only coolant that qualifies is HDB. Of the two H_2 sources, HDB is obviously superior, not only in terms of H_2 yield, but also H_2 gas purity.

3.2.4 Chlorides

The chlorides are included in propellants as Cl-donors to yield HCl in the combustion products. All are commercially available and easily used and handled. The H-containing compounds also yield N_2 as a combustion product, but this is not too important because the chloride content of propellants is not high due to the requirement for a high value of H_2/HCl (97/3). For compositions in which no contaminants are permitted in the combustion products, $ZrCl_4$ can be used as the Cl-donor. For example, the equimolar mixture of $ZrCl_4$ and $Zr(OH)_4$ yields HCl and ZrO_2(c) as the only combustion products.

In terms of H_2 yield, N_2H_5Cl > NH_4Cl > $(NH_4ClO_4 + ZrH_2)$ > $(NH_4ClO_4 + Al)$ > $(NH_4ClO_4 + Zr)$. In terms of HCl yield, NH_4Cl > N_2H_5Cl > $(NH_4ClO_4 + Al)$ > $(NH_4 ClO_4 + Zr)$ = $(NH_4 ClO_4 + ZrH_2)$. Values of (H_2 + HCl) yield purity range from 74% for N_2H_5Cl up to 88% for $NH_4ClO_4 + ZrH_2$. The NH_4ClO_4-fuel combinations are of course more energetic than either of the chlorides.

3.3   Calculation of Theoretical Yield

3.3.1   Procedure

The selection of candidate propellant compositions is based primarily on computed values of theoretical flame temperature and desired combustion product composition. Basically the propellant can be constructed from any combination of oxidizer, fuel, coolant and chloride from the binary combinations in Table 3.1 by means of two equations for a heat and molar ratio balance; these equations are:

$$\Sigma (X\Delta H^{\circ}_{2800})_i = 0 \qquad \text{Heat Balance} \qquad (1)$$

$$\frac{\Sigma (XH_2)_i}{\Sigma (XHCl)_i} = \frac{H_2}{HCl} \qquad \text{Molar Ratio Balance} \quad (2)$$

where X_i are multipliers. In (1) the condition is that combustion is adiabatic, while in (2), $H_2/HCl = 97/3$ generally. In all cases, there are three multipliers (e.g., one for oxidizer-fuel, one for fuel-coolant, and one for chloride) any one of which is arbitrary and can be set to unity. Simultaneous solution of (1) and (2) for the other two multipliers and normalization to 100 result in propellant compositions that yield the flame temperature and H_2 and HCl very close to the desired values. Equilibrium calculations of resulting compositions yield slightly different values than predicted by using (1) and (2) because of mixing effects on entropy and the resultant equilibria. If required, compositions are then sometimes varied slightly to attain the desired results. For example, consider the system $N_2H_5NO_3 + Zr\,H_2 + Zr(OH)_4 + NH_4ClO_4$. What is the OMOX composition with a flame temperature of 2800°K and $H_2/HCl = 97/3$? Consider the three binaries:

A.   40.467% $N_2H_5NO_3$ + 59.533% $Zr\,H_2$, $\Delta H^{\circ}_{2800} = -40.91$,
     $H_2 = 1.685$, HCl = 0

B.   63.078% $Zr(OH)_4$ + 36.922% $Zr\,H_2$, $\Delta H^{\circ}_{2800} = 30.48$,
     $H_2 = 1.181$, HCl = 0

C.   38.654% NH_4ClO_4 + 61.346% ZrH_2, $\Delta H^{\circ}_{2800} = -67.44$,
     $H_2 = 1.144$, HCl = .3048

Let X_A, X_B and X_C be the multipliers for compositions A, B and C, respectively, and set $x_A = 1$.

From (1)

$$- 40.91 + 30.48X_B - 67.44X_C = 0$$

From (2)

$$\frac{1.685 + 1.181X_B + 1.144X_C}{0.3048X_C} = \frac{97}{3}$$

From which we determine

$$X_B = 2.5287$$

$$X_C = 0.53625$$

The resultant composition is comprised of $100X_A = 100$ gm of Composition A plus $100X_B = 252.87$ gm of Composition B and $100X_C = 53.625$ gm of Composition C, and the weight percentages of each ingredient are obtained by normalizing to the sum $X_A + X_B + X_C = 4.0650$:

$$N_2H_5NO_3 = 40.467X_A/(X_A + X_B + X_C)$$

$$= 40.467/4.0650$$

$$= 9.955$$

$$ZrH_2 = (59.533X_A + 36.922X_B + 61.346X_C)/(X_A + X_B + X_C)$$

$$= 185.79 / 4.065$$

$$= 45.706$$

$$Zr(OH)_4 = 63.078X_B/(X_A + X_B + X_C)$$

$$= 159.50/4.065$$

$$= 39.239$$

$$NH_4ClO_4 = 38.654X_C/(X_A + X_B + X_C)$$

$$= 20.728/4.065$$

$$= 5.100$$

Slight variations in the composition to compensate for mixing effects, as above, are generally derived by solving for NH_4ClO_4 content ($[NH_4ClO_4]$) around the above value. Thus, replace (2) with

$$\frac{38.654X_C}{X_A + X_B + X_C} = [NH_4ClO_4]$$

and solve for selected values of $[NH_4ClO_4]$, say $[NH_4ClO_4] = 3, 4, 5, 6$ and 7%.

Calculations of theoretical flame temperature and combustion product composition were carried out for adiabatic combustion at 750 psi followed by isentropic expansion of the gaseous combustion products to throat conditions. The condensed species (Al_2O_3, ZrO_2, W, BN, etc.) in these calculations were assumed to be retained in the combustion chamber and not allowed to undergo the expansion process with the gases. Tabulated values for H_2 yield, HCl yield, and other gaseous species are throat values.

The results of these calculations and the finalized compositions, for H_2/HCl $\sim$ 97/3 are summarized in Tables 3.3 to 3.10. Results are discussed below.

3.3.2   Discussion of Results

The results of the thermochemistry calculations are summarized by oxidizer for compositions containing NH_4NO_3 (Tables 3.3 and 3.4), $N_2H_5NO_3$ (Tables 3.5 and 3.6), NH_4ClO_4 (Table 3.7), H_2WO_4 (Table 3.8), WO_3 (Table 3.9) and $ZrO(NO_3)_2 \cdot 2H_2O$ (Table 3.10). Some calculations were carried out for temperatures other than 2800°K and these also are presented in the Tables, but without discussion.

3.3.2.1 Compositions Containing NH_4NO_3

The results for compositions containing either Zr or ZrH_2 are shown in Table 3.3 whereas results for either Al or AlH_3 are shown in Table 3.4. All of the compositions containing organic coolants (CH_2 or HTPB) easily meet the (H_2 + HCl) weight yield requirement and are easily reduced to practice, but are very poor from the standpoint of (H_2 + HCl) gas purity. The composition that contains off-the-shelf ingredients and that comes closest to meeting the yield requirement (>90%) is 3.3.4, which is comprised of NH_4NO_3, ZrH_2, $Zr(OH)_4$, and NH_4ClO_4. This composition was selected as one of the candidates and is considered to be representative of the best that can be done, in terms of yield and purity, with off-the-shelf ingredients. Notice though that the use of HDB as a coolant (Compositions 3.3.21 and 3.3.22) greatly increases both yield and gas purity.

One of the most serious drawbacks to the use of Al or AlH_3 as a fuel is the recombination of reaction products in the throat. As noted previously, Al_2O_3 is less stable than ZrO_2 at the desired stagnation conditions which result in the reactions

$$Al_2O_3(c) + 2H_2 + 2HCl \rightarrow 2AlCl + 3H_2O \qquad (1)$$

$$Al_2O_3(c) + H_2 + 4HCl \rightarrow 2AlCl_2 + 3H_2O \qquad (2)$$
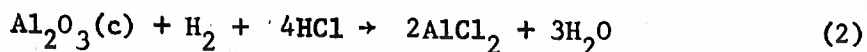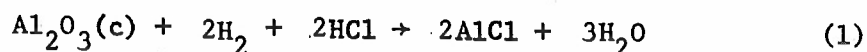
in the combustion chamber. The reverse of these reactions occurs at the throat. Although only gaseous species are expanded to throat conditions, recombination of AlCl or $AlCl_2$ with H_2O results in small amounts of $Al_2O_3(c)$ formation at throat conditions. The yield of Al_2O_3 through recombination is 1-2% by weight of the working fluid. Since the nozzle does not allow time for equilibrium to be obtained, these are strictly thermodynamic results and the amount of Al_2O_3 that actually forms and the extent of interference this phenomenon may have on nozzle and/or laser performance is not known. A similar phenomenon is found for HDB-containing propellants due to recombination of the decomposition and reaction products of BN(c). However, this compound can be used in a two-compartment motor system, and the BN can be filtered prior to admixture of the H_2 with the other combustion products. In this way, the recombination phenomenon is obviated.

Table 3.3
Theoretical Values of Flame Temperature and Yield for Selected OMOX Compositions:
Compositions Containing NH_4NO_3 and Either Zr or ZrH_2

Comp ID	Propellant Composition, Wt %								T_f, °K,* @750 psia	H_2/HCl* (molar)	Yield $(H_2$+HCl) * Wt %	Vol %
	Oxidizer		Fuel		Coolant		Chloride					
3.3.1	29.144	NH_4NO_3	57.325	ZrH_2	10.948	$Zr(OH)_4$	2.583	NH_4Cl	3000	32.1	4.85	79.4
3.3.2	17.950		49.203		30.482		2.365		2799	32.2	4.46	85.1
3.3.3	20.241	NH_4NO_3	54.914	ZrH_2	19.845	$Zr(OH)_4$	5	NH_4ClO_4	3000	33.1	4.35	83.0
3.3.4	10.482		47.132		38.386		4		2801	38.2	3.84	89.5
3.3.5	4.008		42.838		48.440		4.714		2400	30.7	3.93	94.6
3.3.6	36.955	NH_4NO_3	58.194	ZrH_2	1.917	$(CH_2)_n$	2.934	NH_4Cl	3000	32.2	5.51	73.5
3.3.7	39.538		52.007		5.137		3.318		2801	32.3	6.27	69.4
3.3.8	40.574		49.532		6.426		3.468		2602	32.3	6.57	68.2
3.3.9	34.015	NH_4NO_3	56.126	ZrH_2	3.859	$(CH_2)_n$	6	NH_4ClO_4	3000	36.3	6.45	70.9
3.3.10	35.990		49.702		7.308		7		2802	34.2	6.26	67.3
3.3.11	37.162		47.145		8.693		7		2602	35.9	6.47	66.2
3.3.12	33.918	NH_4NO_3	54.736	ZrH_2	4.655	HTPB	6.691	NH_4ClO_4	3000	31.0	5.58	69.0
3.3.13	36.803		47.670		8.527		7		2802	33.1	6.11	64.4
3.3.14	38.122		44.740		10.137		7		2602	34.5	6.30	63.0
3.3.15	39.461		41.768		11.771		7		2402	35.9	6.47	61.5
3.3.16	39.628	NH_4NO_3	43.982	Zr	10.394	HTPB	6	NH_4ClO_4	3000	31.7	5.07	56.1
3.3.17	41.904		38.876		13.220		6		2801	35.6	5.51	55.2
3.3.18	42.118		36.226		14.656		7		2601	32.1	6.02	54.9
3.3.19	43.208		33.784		16.008		7		2401	33.7	6.21	54.5
3.3.20	23.507	NH_4NO_3	40.182	Zr	30.311	HDB	6	NH_4Cl	2825	34.0	10.1	89.3
3.3.21	2.482	NH_4NO_3	33.744	Zr	44.774	HDB	19	NH_4ClO_4	2812	32.0	12.7	95.3
3.3.22	7.782	NH_4NO_3	34.896	Zr	40.322 + 1	HDB $(CH_2)_n$	16	NH_4ClO_4	2818	34.1	11.8	92.6

* Notes: T_f is adiabatic flame temperature at a combustion pressure of 750 psia.

H_2/HCl and yield (H_2+HCl) refer to combustion product values at throat conditions.

Yield (H_2+HCl), vol. % is the yield purity value.

Table 3.4

Theoretical Values of Flame Temperature and Yield for Selected OMOK Compositions: Compositions Containing NH_4NO_3 and Either Al or AlH_3.

Comp ID	Propellant Composition, Wt %								T_f, °K, @750 psia	H_2/HCl (molar)	Yield (H_2+HCl) Wt %	Yield (H_2+HCl) Vol %
	Oxidizer		Fuel		Coolant		Chloride					
3.4.1	23.140	NH_4NO_3	30.571	Al	43.289	$Al(OH)_3$	3	NH_4Cl	2989	33.8	4.56	80.6
3.4.2	18.016		29.462		50.069		2.453		2791	37.8	4.39	84.8
3.4.3	13.647	NH_4NO_3	30.219	Al	50.119	$Al(OH)_3$	6.015	NH_4ClO_4	2995	34.4	4.19	85.3
3.4.4	10.212		29.179		55.609		5		2794	38.2	4.10	89.2
3.4.5	59.033	NH_4NO_3	26.953	Al	10.014	$(CH_2)_n$	4	NH_4Cl	2971	39.4	6.67	59.9
3.4.6	58.973		25.097		11.430		4.5		2776	33.0	7.48	60.2
3.4.7	59.442		23.294		13.082		4.182		2584	34.6	7.73	60.0
3.4.8	52.190	NH_4NO_3	25.431	Al	12.379	$(CH_2)_n$	10	NH_4ClO_4	2970	34.4	7.02	58.6
3.4.9	52.463		23.541		13.996		10		2777	32.9	7.54	59.0
3.4.10	53.005		21.791		15.502		9.702		2585	33.0	7.92	59.0
3.4.11	52.234	NH_4NO_3	23.772	Al	13.994	HTPB	10	NH_4ClO_4	2970	32.2	6.76	55.5
3.4.12	53.454		21.870		15.676		9		2778	34.3	6.97	55.5
3.4.13	53.707		19.947		17.346		9		2585	33.2	7.36	55.2
3.4.14	53.952		18.100		18.948		9		2393	32.6	7.68	54.8
3.4.15	36.026	NH_4NO_3	35.610	AlH_3	22.364	$Al(OH)_3$	6	NH_4Cl	2784	33.9	10.1	85.7
3.4.16	39.289	NH_4NO_3	35.162	AlH_3	18.549 + 1	$Al(OH)_3$ CH_2	6	NH_4Cl	2783	34.5	10.2	83.6

3.3.2.2 Compositions Containing $N_2H_5NO_3$

These results are shown in Table 3.5 for compositions containing either Zr or ZrH_2 as a fuel and in Table 3.6 for Al and AlH_3 as fuels. Compared to NH_4NO_3, the use of this oxidizer in comparable formulations results in slight increases in yield and decreases in gas purity. For example, compare 3.3.2 and 3.5.2, at 2800°K the composition containing NH_4 has a weight yield of 4.46% and a purity of 85.1%, whereas the composition containing $N_2H_5NO_3$ has a weight yield of 4.64% and a purity of 81.4%.

3.3.2.3 Compositions Containing Either H_2WO_4 or WO_3

These oxidizers are ideal for use in thermite systems, resulting in excellent clinkers. Both result in high values of (H_2 + HCl) gas purity since no N_2 is introduced in the combustion products. When used in propellants made with off-the-shelf ingredients, H_2WO_4 is preferred. The composition 3.8.1, comprised of H_2WO_4, ZrH_2, Zr, and NH_4ClO_4 is representative of the best that can be attained from thermite systems made with off-the-shelf materials and was selected as one of the propellant candidates. Note that the yield of this composition, 2.59%, is very low; however, it is also very pure. When used with HDB, there is not much advantage between the two oxidizers and, in fact, the performance is comparable to the use of NH_4NO_3 or $N_2H_5NO_3$ (>10% weight yield). The composition selected as one of the candidates was composition 3.8.8.

Table 3.5
Theoretical Values of Flame Temperature and Yield for Selected OMOX Compositions: Compositions Containing $N_2H_5NO_3$ and Either Zr or ZrH_2

Comp ID	Propellant Composition, Wt %								T_f, °K, @750 psia	H_2/HCl (molar)	Yield (H_2+HCl) Wt %	Yield (H_2+HCl) Vol %
	Oxidizer		Fuel		Coolant		Chloride					
3.5.1	31.997	$N_2H_5NO_3$	53.994	ZrH_2	11.484	$Zr(OH)_4$	2.725	NH_4Cl	3000	32.1	5.11	75.1
3.5.2	19.832		47.097		30.615		2.456		2800	32.2	4.64	81.4
3.5.3	31.621	$N_2H_5NO_3$	53.292	ZrH_2	11.571	$Zr(OH)_4$	3.516	N_2H_5Cl	3000	32.1	5.15	74.6
3.5.4	22.126	$N_2H_5NO_3$	52.444	ZrH_2	20.430	$Zr(OH)_4$	5	NH_4ClO_4	3000	34.4	4.46	79.2
3.5.5	41.560	$N_2H_5NO_3$	52.696	ZrH_2	2.541	$(CH_2)_n$	3.203	NH_4Cl	2950	32.2	6.02	68.9
3.5.6	43.917	$N_2H_5No_3$	47.368		5.188		3.527		2801	32.3	6.66	66.3
3.5.7	40.759	$N_2H_5NO_3$	53.131	ZrH_2	2.056	$(CH_2)_n$	4.054	N_2H_5Cl	3000	32.2	5.94	68.9
3.5.8	37.070	$N_2H_5NO_3$	51.781	ZrH_2	4.164	$(CH_2)_n$	6.985	NH_4ClO_4	3000	32.2	5.97	67.5
3.5.9	35.114	$N_2H_5NO_3$	51.658	ZrH_2	9.290	HDB	3.938	NH_4Cl	2999	32.1	7.38	79.4
3.5.10	25.758	$N_2H_5NO_3$	37.074	Zr	29.168	HDB	8	N_2H_5Cl	2826	32.7	10.4	85.7
3.5.11	3.969	$N_2H_5NO_3$	33.661	Zr	44.370	HDB	18	NH_4ClO_4	2817	33.2	12.6	94.8
3.5.12	23.808	$N_2H_5NO_3$	34.267	Zr	31.825 +4.100	HDB $Zr(OH)_4$	6	$ZrCl_4$	2831	36.8	9.84	88.7

Table 3.6

Theoretical Values of Flame Temperature and Yield for Selected OMOX Compositions:

Compositions Containing $N_2H_5NO_3$ and Either Al or AlH_3

Comp ID	Oxidizer		Fuel		Coolant			Chloride	T_f, °K, @750 psia	H_2/HCl (molar)	Yield (H_2+HCl) Wt %	Vol %
3.6.1	25.786	$N_2H_5NO_3$	29.177	Al	42.037	$Al(OH)_3$	3	NH_4Cl	2989	35.8	4.70	76.6
3.6.2	20.438		28.294		48.268		3		2789	32.0	4.86	80.8
3.6.3	25.523	$N_2H_5NO_3$	28.876	Al	41.601	$Al(OH)_3$	4	N_2H_5Cl	2988	34.6	4.81	75.8
3.6.4	14.546	$N_2H_5NO_3$	29.383	Al	49.571	$Al(OH)_3$	6.5	NH_4ClO_4	2995	32.5	4.39	82.6
3.6.5	62.206	$N_2H_5NO_3$	23.884	Al	8.910	$(CH_2)_n$	5	NH_4Cl	2969	32.4	7.47	58.4
3.6.6	63.059		21.867		10.861		4.213		2777	37.4	7.57	58.4
3.6.7	61.228	$N_2H_5NO_3$	23.477	Al	8.796	$(CH_2)_n$	6.5	N_2H_5Cl	2968	32.1	7.54	58.3
3.6.8	54.611	$N_2H_5NO_3$	22.537	Al	11.852	$(CH_2)_n$	11	NH_4ClO_4	2967	32.5	7.49	57.3
3.6.9	36.180	$N_2H_5NO_3$	20.536	Al	34.784	HDB	8.5	NH_4Cl	2950	32.0	12.8	84.5
3.6.10	47.622	$N_2H_5NO_3$	34.316	AlH_2	11.062	$Al(OH)_3$	7	NH_4Cl	2982	32.6	10.44	78.7
3.6.11	37.348	$N_2H_5NO_3$	32.764	AlH_3	23.888	$Al(OH)_3$	6	NH_4Cl	2746	33.1	10.1	82.8
3.6.12	24.568	$N_2H_5NO_3$	30.736	AlH_3	39.588	$Al(OH)_3$	5.108	NH_4Cl	2391	34.0	9.52	87.7
3.6.13	57.759	$N_2H_5NO_3$	32.379	AlH_3	2.862	$Al(OH)_3$	7	NH_4Cl	2978	34.2	10.8	73.5
3.6.14	59.143	$N_2H_5NO_3$	29.044	AlH_3	5.813	$(CH_2)_n$	6	NH_4Cl	2780	37.2	10.7	71.5
3.6.15	18.264	$N_2H_5NO_3$	33.600	AlH_3	36.136	$Al(OH)_3$	12	NH_4ClO_4	2794	34.3	9.20	88.8
3.6.16	6.248	$N_2H_5NO_3$	31.246	AlH_3	51.506	$Al(OH)_3$	11	NH_4ClO_4	2395	32.2	8.99	95.0
3.6.17	32.337	$N_2H_5NO_3$	28.895	AlH_3	33.768	$Zr(OH)_4$	5	NH_4Cl	2784	35.6	8.63	82.9
3.6.18	12.474	$N_2H_5NO_3$	27.300	AlH_3	50.226	$Zr(OH)_4$	10	NH_4ClO_4	2794	33.5	7.56	90.0

Table 3.7
Theoretical Values of Flame Temperature and Yield for Selected OMOX Compositions:
Miscellaneous Compositions Containing NH_4ClO_4

Comp ID	Propellant Composition, Wt %								T_f, °K, @750 psia	H_2/HCl (molar)	Yield (H_2+HCl) Wt %	Vol %
	Oxidizer		Fuel		Coolant		Chloride					
3.7.1	42.794	NH_4ClO_4	26.206	Al	31	HDB			2798	42.4	9.28	76.5
3.7.2	16.725	NH_4ClO_4	9.717	Al	70.161	HDB	3.397	$ZrCl_4$	2347	34.4	18.6	98.2
3.7.3	13.317	NH_4ClO_4	20.677	Zr	66.006	HDB			2394	50.6	15.6	98.8
3.7.4	13.586	NH_4ClO_4	19.921	Zr	63.493	HDB	3	$ZrCl_4$	2393	32.9	17.0	98.7
3.7.5	3.095	NH_4ClO_4	37.850	Zr	0.205	$(CH_2)_n$			2800	30.2	2.55	96.2
3.7.6	3.000	NH_4ClO_4	35.728 +2.596	Zr ZrH_2	58.676	$Zr(OH)_4$			2800	31.6	2.54	98.0
3.7.7	16.714	NH_4ClO_4	26.526	ZrH_2	56.760	HDB			2384	37.1	15.7	98.4

Table 3.8
Theoretical Values of Flame Temperature and Yield for Selected OMOX Compositions:
Compositions Containing H_2WO_4 and Either Zr or ZrH_2

Comp ID	Propellant Composition, Wt %								T_f, °K, @750 psia	H_2/HCl (molar)	Yield (H_2+HCl) Wt %	Yield (H_2+HCl) Vol %
	Oxidizer		Fuel		Coolant		Chloride					
3.8.1	40.879	H_2WO_4	42.968	ZrH_2	13.153	$Zr(OH)_4$	3	NH_4ClO_4	2799	32.6	2.59	98.0
3.8.2	20.641	H_2WO_4	41.453	ZrH_2	34.051	$Zr(OH)_4$	3.855	NH_4ClO_4	2400	30.8	3.21	98.3
3.8.3	54.657	H_2WO_4	42.018	ZrH_2	0.825	$(CH_2)_n$	2.5	NH_4ClO_4	2800	35.9	2.30	91.4
3.8.4	57.018	H_2WO_4	41.649	ZrH_2	0.127	$(CH_2)_n$	1.206	$ZrCl_4$	2798	33.5	2.09	98.2
3.8.5	55.282	H_2WO_4	41.856	ZrH_2	0.615	$(CH_2)_n$	0.465 +1.782	$ZrCl_4$ NH_4ClO_4	2799	31.9	2.31	93.1
3.8.6	32.348	H_2WO_4	30.354 +9.827	ZrH_2 Zr	11.363 +9.292	HDB $Zr(OH)_4$	6.816	NH_4ClO_4	2780	34.6	4.92	96.4
3.8.7	47.996	H_2WO_4	35.044	Zr	14.533	HDB	2.427	NH_4Cl	2802	41.5	4.25	96.5
3.8.8	11.821	H_2WO_4	33.475	Zr	38.704	HDB	16	NH_4ClO_4	2808	33.3	10.8	95.9
3.8.9	21.952	H_2WO_4	33.623	Zr	30 +1	HDB $(CH_2)_n$	13.425	NH_4ClO_4	2802	32.2	8.91	93.7
3.8.10	48.988	H_2WO_4	7.096 +33.816	Zr ZrH_2	6.600 +1	$Zr(OH)_4$ $(CH_2)_n$	2.5	NH_4ClO_4	2800	35.2	2.26	89.9

Table 3.9
Theoretical Values of Flame Temperature and Yield for Selected OMOX Compositions:
Compositions Containing WO_3 and Either Zr or ZrH_2

Comp ID	Oxidizer		Fuel		Coolant		Chloride		T_f, °K, @750 psia	H_2/HCl (molar)	Yield (H_2+HCl) Wt %	Vol %
3.9.1	45.181	WO_3	38.685	ZrH_2	14.124	$Zr(OH)_4$	2	NH_4ClO_4	2789	36.4	1.86	98.2
3.9.2	60.983	WO_3	36.097	ZrH_2	1.084	$(CH_2)_n$	1.836	NH_4ClO_4	2800	31.4	1.55	85.1
3.9.3	62.957	WO_3	35.697	ZrH_2	0.596	$(CH_2)_n$	0.750	$ZrCl_4$	2799	33.0	1.30	90.6
3.9.4	62.143	WO_3	11.593	Zr	25.637	ZrH_2	0.627	N_2H_5Cl	3000	32.2	0.916	95.9
3.9.5	60.239	WO_3	7.178	Zr	31.199	ZrH_2	1.384	NH_4ClO_4	3000	30.2	1.13	97.2
3.9.6	9.960	WO_3	28.959	Zr	49.327 +9.254	$Zr(OH)_4$ ZrH_2	2.5	NH_4ClO_4	2800	35.4	2.28	98.1
3.9.7	53.819	WO_3	31.763	Zr	12.845	HDB	1.846	NH_4Cl	2998	32.2	3.45	97.4
3.9.8	20.113	WO_3	32.056	Zr	34.831	HDB	13	NH_4ClO_4	2811	36.2	9.27	96.0
3.9.9	17.840	WO_3	10.529 +20.032	Zr ZrH_2	37.889	HDB	13	NH_4ClO_4	2600	34.2	11.0	98.1

Table 3.10
Theoretical Values of Flame Temperature and Yield for Selected OMOX Compositions:
Compositions Containing $ZrO(NO_3)_2 \cdot 2H_2O$ and Either Zr or ZrH_2

Comp ID	Oxidizer	Fuel		Coolant		Chloride		T_f, °K, @750 psia	H_2/HCl (molar)	Yield (H_2+HCl) Wt %	Yield (H_2+HCl) Vol %
3.10.1	34.593 $ZrO(NO_3)_2 \cdot 2H_2O$	50.168	ZrH_2	13.549	$Zr(OH)_4$	1.690	NH_4Cl	3000	32.1	3.17	86.7
3.10.2	21.348 $ZrO(NO_3)_2 \cdot 2H_2O$	44.812	ZrH_2	32.024	$Zr(OH)_4$	1.816	NH_4Cl	2799	32.2	3.43	91.5
3.10.3	26.311 $ZrO(NO_3)_2 \cdot 2H_2O$	49.998	ZrH_2	19.691	$Zr(OH)_4$	4	NH_4ClO_4	3000	30.3	3.29	89.1
3.10.4	12.840 $ZrO(NO_3)_2 \cdot 2H_2O$	44.598	ZrH_2	38.562	$Zr(OH)_4$	4	NH_4ClO_4	2800	32.6	3.46	94.0
3.10.5	46.846 $ZrO(NO_3)_2 \cdot 2H_2O$	48.784	ZrH_2	2.532	$(CH_2)_n$	1.838	NH_4Cl	3000	32.2	3.45	74.4
3.10.6	50.069 $ZrO(NO_3)_2 \cdot 2H_2O$	42.045	ZrH_2	5.743	$(CH_2)_n$	2.143	NH_4Cl	2802	32.3	4.05	68.0
3.10.7	44.307 $ZrO(NO_3)_2 \cdot 2H_2O$	47.924	ZrH_2	3.769	$(CH_2)_n$	4	NH_4ClO_4	3000	34.2	3.56	71.8
3.10.8	46.725 $ZrO(NO_3)_2 \cdot 2H_2O$	41.084	ZrH_2	7.191	$(CH_2)_n$	5	NH_4ClO_4	2802	32.1	4.28	66.1

Propellant Composition, Wt %

3.4   Properties of Candidate Propellants

3.4.1   General

The three candidate compositions chosen for evaluation in motor firings are Compositions 3.3.4, 3.8.1 and 3.8.8. The first two selections are about the best that can be obtained with off-the-shelf ingredients with regard to yield and purity, while the last is a composition containing HDB. As indicated in the tables of the previous section, there are other propellant selections besides 3.8.8 that have a high yield; however, only one high-yield high-risk system was selected. This selection was based on the system that appeared to have the highest probability of success. The Composition 3.3.4 is comprised of NH_4NO_3, ZrH_2, $Zr(OH)_4$, and NH_4ClO_4; Composition 3.8.1 is comprised of H_2WO_4, ZrH_2, $Zr(OH)_4$, and NH_4ClO_4, and Composition 3.8.8 is comprised of H_2WO_4, Zr, HDB and NH_4ClO_4. The safety and ballistic properties of each composition were measured, and are given in Table 3.11. Detailed theoretical results for flame and throat temperatures for the combustion product composition at a chamber pressure of 750 psia are given for each of the compositions in Table 3.12. Burning rate curves of rate vs pressure are shown for compositions 3.3.4 and 3.8.1 in Figures 3.2 and 3.3, respectively.

All of the compositions are prepared by first blending the ingredients and then pressing them to the desired size and shape at 30 KSI. For each composition, two values of the nozzle discharge coefficient are given, one for the gas-only flow condition (which is the design condition) and the other for the flow of both gases and solids (given in parenthesis). Burning rates are for specimens ~0.5" dia x ~1"long pressed at 30 KSI in steel tubes. Burning rates derived from subscale motor firings (see Section 3.5) are also shown. Results are discussed below.

3.4.2   Properties of Composition 3.3.4

This composition is the best (in terms of gas purity) of the nitrate-containing systems comprised of off-the-shelf ingredients. The composition presses up fairly well at 30 KSI, ignites easily and burns uniformly in the pressure range 400-1500 psia. Combustion at 750 psia yields combustion products comprised of 8.04% by weight gases and 91.96% solids. At this pressure, and at higher values, the solids form a good clinker. At low pressure (<100 psia) the condensed combustion products do not adhere and are entrained by the gases.

Table 3.11

PROPERTIES OF CANDIDATE PROPELLANTS

Property	Comp 3.3.4		Comp 3.8.1		Comp 3.8.8	
A. Composition, Wt%						
Oxidizer	10.482	NH_4NO_3	40.879	H_2WO_4	11.821	H_2WO_4
Fuel	47.132	ZrH_2	42.968	ZrH_2	33.475	Zr
Coolant	38.186	$Zr(OH)_4$	13.153	$Zr(OH)_4$	38.704	HDB
Chloride	4.000	NH_4ClO_4	3.000	NH_4ClO_4	16.000	NH_4ClO_4
B. Theoreticals						
Flame Temperature, °K		2799		2799		2808
(H_2/HCl) molar		38.7		32.6		33.3
Yield (H_2+HCl)						
Wt. %		3.84		2.59		10.8
Vol. %		89.5		98.0		95.9
Discharge Coefficient, C_D, sec,$^{-1}$		0.00312 (0.01055)		0.00249 (0.01369)		0.00292 (0.00686)
C. Compaction Density, gm/cc,@30 KSI		2.60		3.35		1.53
D. Burning Rate, in/sec, vs P_c(PSIA) pressed @ 30 KSI		$0.48(P/1000)^{0.29}$		$0.21(P/1000)^{0.20}$		–
E. Sensitivity to Ignition						
Impact		225 kg-cm		>300 kg-cm		42 kg-cm
Friction		neg (Esso screw) 60°@100 psi (ABL)		neg (Esso screw) 75°@300 psi (ABL)		neg (Esso screw) 45°@100 psi (ABL)
Electrostatic Discharge		>6J @ 5000 V		>6J @ 5000 V		0.0056J @ 5000 V
Autoignition Temperature		>400°C		>400°C		229°C

TABLE 3.12

COMBUSTION PRODUCTS OF CANDIDATE PROPELLANTS

Composition 3.3.4			Composition 3.8.1			Composition 3.8.8		
Specie	Chamber	Throat	Specie	Chamber	Throat	Specie	Chamber	Throat
CL	0.00028	0.00011	CL	0.00020	0.00008	B	0.00011	0.00002
H	0.01575	0.00597	HC1	0.02487	0.02532	BCL2H	0.00052	0.00046
H2	1.28937	1.29426	H2	0.82210	0.82506	BH2	0.02901	0.01109
NH3	0.00016	0.00012	NH3	0.00004	0.00003	BN	0.00003	0.00001
N2	0.14712	0.14714	N2	0.01249	0.01250	BOH	0.00106	0.00052
OH	0.00001	0.00000	ZRCL4	0.00003	0.00001	B2O	0.00044	0.00012
ZRN8	0.00155	0.00000	ZRO28	0.54281	0.00010	CL	0.00078	0.00061
ZRCL4	0.00001	0.00000	H2O	0.00129	0.00110	HBO2	0.00074	0.00067
NH2	0.00002	0.00001	WCL2	0.00004	0.00002	H2	3.55937	3.58573
ZRCL3	0.00003	0.00000	ZRCL2	0.00002	0.00000	NH2	0.00003	0.00001
HC1	0.03363	0.03391	W8	0.16356	0.00003	WCL2	0.00015	0.00012
H2O	0.00328	0.00321	H	0.00962	0.00368	ZRCL3	0.00711	0.00410
ZRCL2	0.00001	0.00000	ZRCL3	0.00007	0.00001	ZRO	0.00011	0.00001
ZRO28	0.74496	0.00004	ZRN8	0.00050	0.00000	BN$	1.26001	0.04158
T °K	2799	2479	T °K	2799	2481	ZRO2$	0.35327	0.00525
						BCL2	0.00039	0.00027
						BH	0.00017	0.00004
						BH3	0.00249	0.00100
						BOCL	0.00204	0.00179
						B2O3	0.00015	0.00012
						H	0.04350	0.02849
						ZRCL2	0.00305	0.00096
						ZRH	0.00001	0.00000
						BC1	0.00933	0.00503
						BCL3	0.00001	0.00001
						BH2N	0.01234	0.00543
						BO	0.01106	0.00570
						B2O2	0.00422	0.00243
						B3H3O3	0.00001	0.00001
						HC1	0.09305	0.11072
						H2O	0.00093	0.00084
						NH3	0.00023	0.00014
						ZRCL	0.00032	0.00005
						ZRCL4	0.00240	0.00263
						W$	0.03831	0.00003
						N2	0.10551	0.08825
						T °K	2807	2619

$ - Condensed Specie
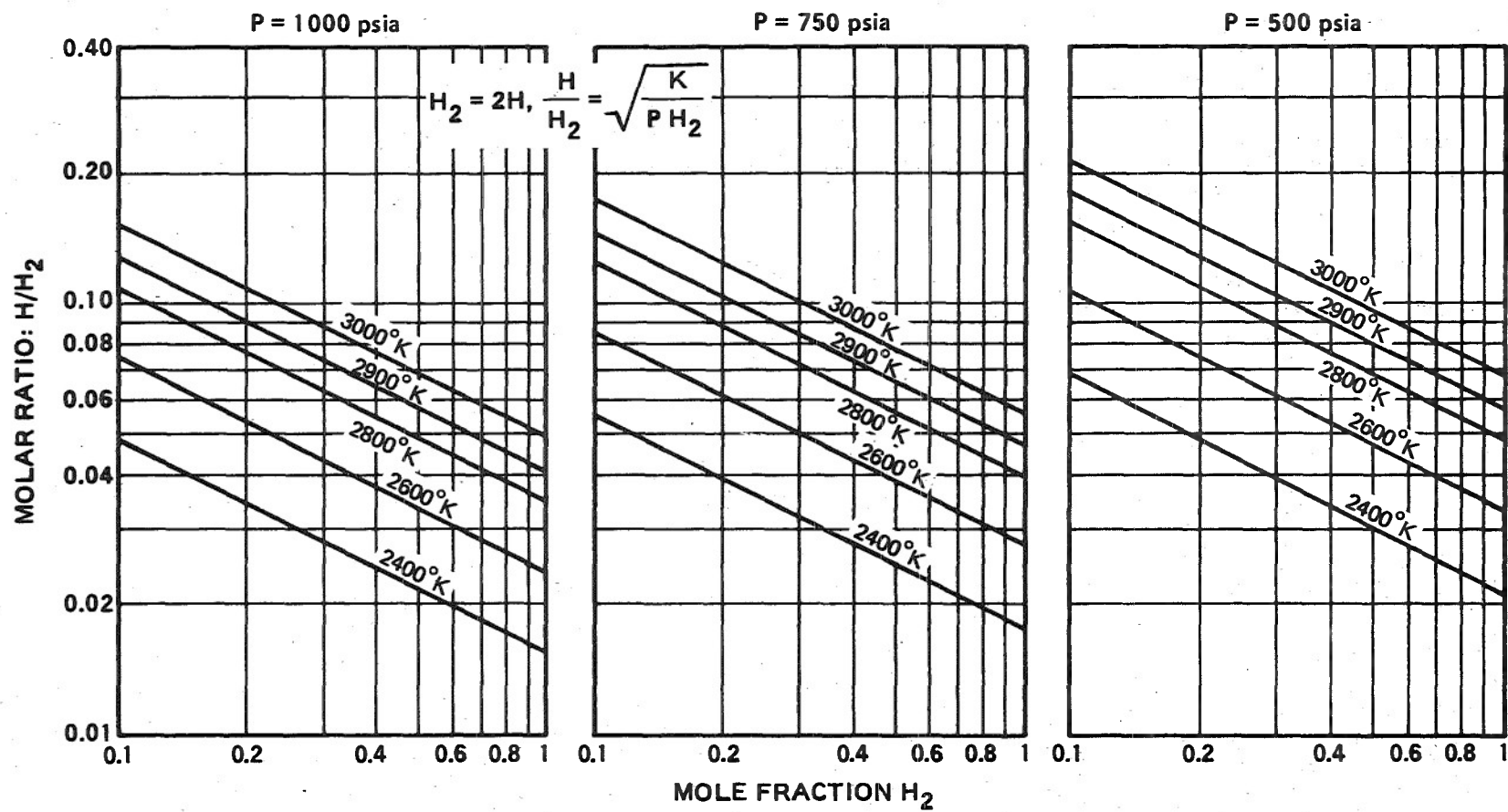
Figure 3.1. Effect of Temperature, Pressure and Concentration on H_2 Dissociation.

$$10.482\% \ NH_4NO_3 + 47.132\% \ ZrH_2 + 38.386\% \ Zr(OH)_4 + 4\% \ NH_4ClO_4$$
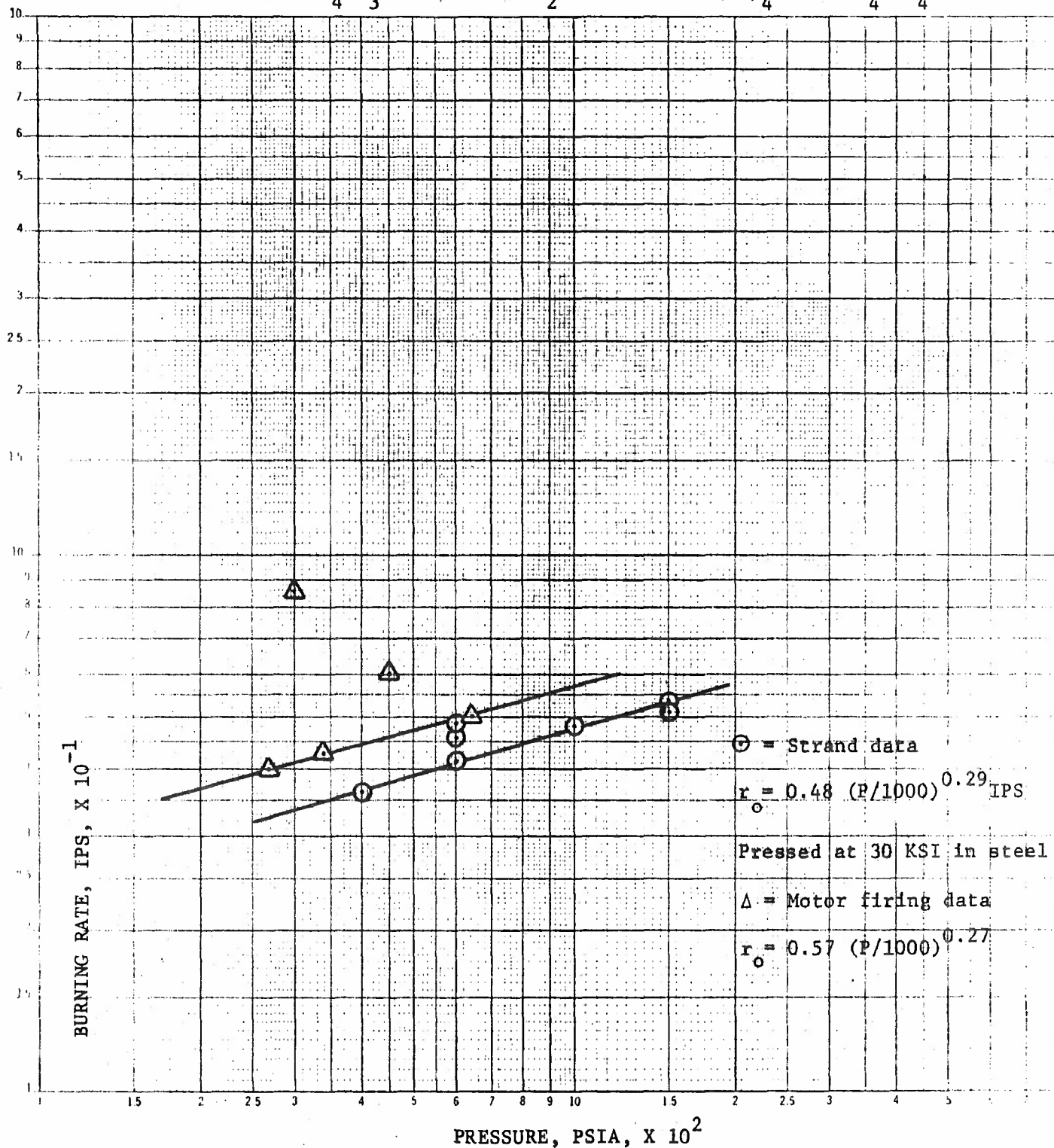
Figure 3.2. Burning Rate of Comp. 3.3.4.

$$40.879\% \text{ H}_2\text{WO}_4 + 42.968\% \text{ ZrH}_2 + 13.153\% \text{ Zr(OH)}_4 + 3\% \text{ NH}_4\text{ClO}_4$$

$\odot$ = Strand data

$r_o = 0.21 \ (P/1000)^{0.2}$ IPS

Pressed at 30 PSI in steel

$\triangle$ = Motor firing data

$r_\triangle = 0.22 \ (P/1000)^{0.2}$

BURNING RATE, IPS, X 10^{-1}

PRESSURE, PSIA, X 10^2

Figure 3.3. Burning Rate of Comp. 3.8.1.

The propellant composition has excellent safety properties. Because of the use of NH_4NO_3 and $Zr(OH)_4$, the composition must be processed in a low humidity facility (<50% relative humidity at 70°F is satisfactory). Because of the phase change exhibited by NH_4NO_3, the propellant cannot withstand temperature cycles of -40/+140°F without loss of some structural strength.

3.4.3   Properties of Composition 3.8.1

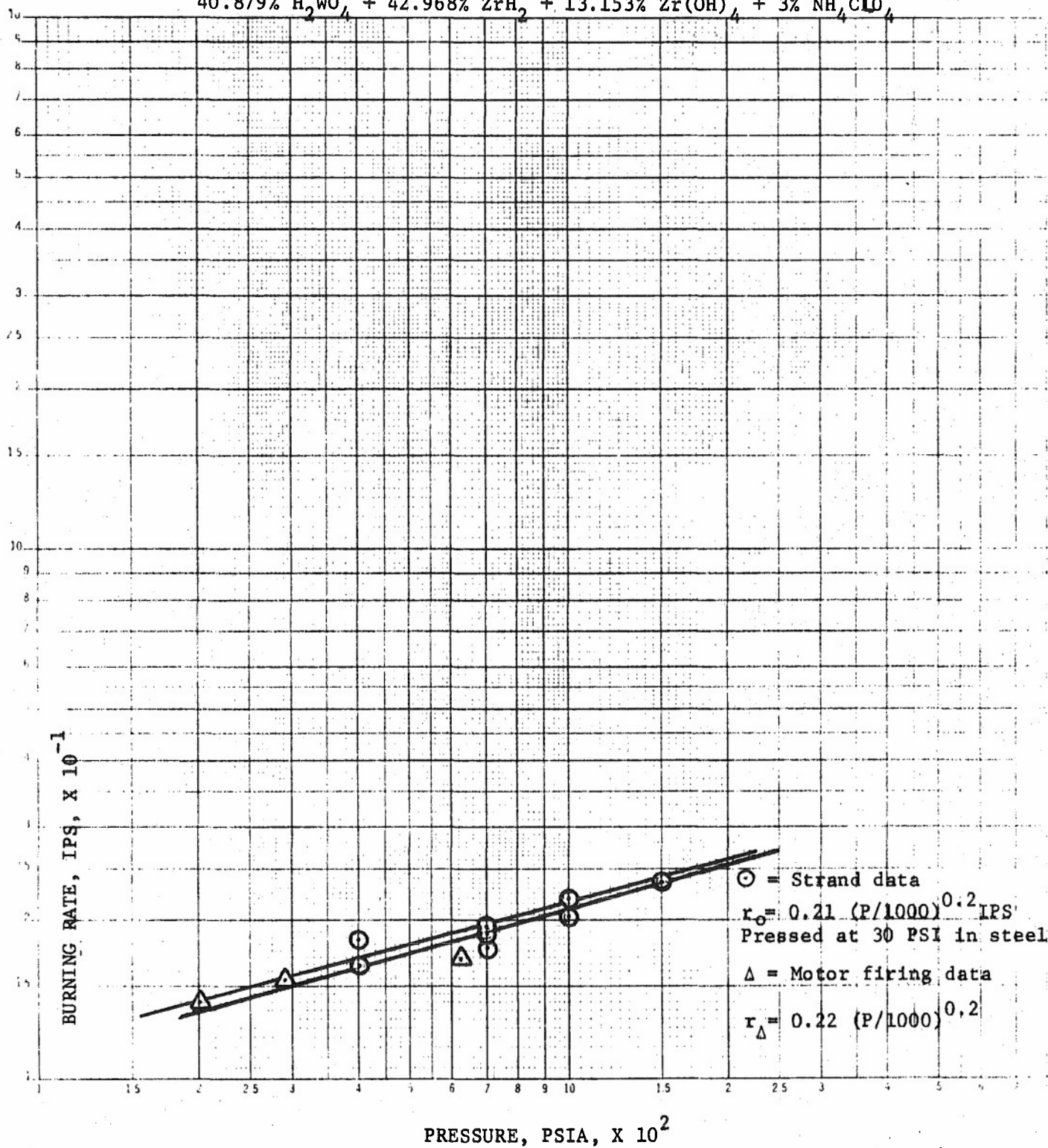This composition is the best of the thermite systems (in terms of yield and purity) comprised of off-the-shelf ingredients. An excellent clinker is formed on combustion at all pressures. The total gas yield of the composition is only 2.59% by weight, the remainder being $ZrO_2(\ell)$ and $W(c)$. This propellant also has excellent safety properties. The use of $Zr(OH)_4$ requires dry processing and handling facilities but presents no major problem. The composition can be temperature cycled with no adverse affects.

3.4.4   Properties of Composition 3.8.8

This composition is one of the best of any of the systems evaluated, in terms of yield and purity. It contains HDB, and is the result of an extensive laboratory-scale search for ways and means to use the compound in propellants. It proved to be a difficult goal to obtain, because the material on hand was from various production lots and this seemed to affect propellant properties to a great extent. The propellants studied proved to be sensitive to ignition by mechanical means and difficult to burn uniformly over a wide pressure range, and difficult to store and use, even in a dry environment.

Initially, work with the Composition 3.9.8 (WO_3/Zr/HDB/NH_4ClO_4) indicated unstable combustion when 1/2 inch diameter pellets pressed at 30 KSI were burned at 1500 psi. At combustion pressures (Pc) <1000 psi, the pellets burn uniformly at a rate $r = 2.51 (Pc/1000)^{0.58}$ in/sec. At Pc = 1500 psi, these pellets explode when ignited. When pressed at 20 KSI, the pellets exploded when burned at 400 psi. Substitution of H_2WO_4 for WO_3 (i.e., Composition 3.8.8) reveals a similar result, although there was some evidence of HDB batch effects on this phenomenon since one of the batches of HDB gave uniform burns at 1500 psi, while another exploded. Substitution of hydrazine nitrate ($N_2H_5NO_3$) for the oxidizer also resulted in explosive burning at 1500 psi. These results indicate that the substitution of oxidizer is not sufficient to stabilize high pressure combustion of HDB propellants.

The substitution of either ZrH_2 for Zr and/or NH_4Cl (or N_2H_5Cl) for NH_4ClO_4 in propellants containing HDB and either WO_3 or H_2WO_4 gives yield values in the range 3-5% by weight (Comps 3.8.6 and 3.8.7 and 3.9.7) and as a result are not particularly interesting. Neither compound is energetic and consequently results in compositions containing low values of HDB content and therefore low values of H_2 yield. Substitution of Al for Zr yields combustion products which are significantly contaminated with dissociation products of Al_2O_3 (which is not as thermally stable as ZrO_2). In these latter systems, species such as $AlBO_2$ and $BOCl$ are also important combustion products.

The use of another chloride as a substitute for NH_4ClO_4 is possible in propellants containing $N_2H_5NO_3$ as the oxidizer. For compositions containing other oxidizers, the favored chlorides are mixtures of NH_4ClO_4 and a fuel (e.g., Zr or ZrH_2) stoichiometric to the major metal oxide (e.g., ZrO_2). These are high-energy compositions that release HCl as a major combustion product and require large amounts of coolant (HDB, etc.) to maintain the flame temperature at the desired value of 2800°K. As noted above, the use of NH_4Cl in place of NH_4ClO_4 results in low values of H_2 yield with either WO_3 or H_2WO_4 as oxidizers, because the NH_4Cl is a coolant as well as an HCl donor and the HDB content is accordingly reduced. The use of $N_2H_5NO_3$ overcomes this difficulty because of the greater energy of $N_2H_5NO_3$/Zr or ZrH_2 mixtures compared to those of WO_3 or H_2WO_4/Zr or ZrH_2. Thus, the use of low-energy chlorides requires the use of a high-energy oxidizer in order to maintain acceptably high values of H_2 yield. An alternate candidate oxidizer is NH_4NO_3. Toward this end, studies were directed toward the system $N_2H_5NO_3$/Zr/HDB/N_2H_5Cl (composition 3.5.10). The commonality of the ingredients is conducive to stability and compatibility. The composition burns uniformly at pressure up to 1500 psi at a rate of $r = 1.05 (P/1000)^{0.65}$ ips, when compacted in 1/2 inch diameter steel tubes at 30 KSI (compaction density = 1.63 gm/cc). Unfortunately, the (H_2 + HCl) gas purity is (85.7%) which is too low to be of interest. Also, the composition is extremely moisture sensitive. At values of relative humidity of 40% (at 70°F), the composition physically degrades through chemical reaction. Under desiccated conditions, no evidence of chemical reaction is seen. A slight improvement in gas purity can be attained by use of the stoichiometric mixtures $Zr(OH)_4 + ZrCl_4$ as the HCl generator (Composition 3.5.12).

The best solution seemed to be through the use of HDB as a mono-propellant coupled with the oxidizer/fuel/chloride as a second component in a bipropellant motor configuration. The propellant composition 3.8.8 can be divided into two propellants, one comprised of HDB, the other comprised of the remainder of composition 3.8.8, i.e., H_2WO_4, Zr, and NH_4ClO_4 (called Mix 22). The physical, ballistic, and safety properties of these two propellants are given in Table 3.13 and 3.14 and Figures 3.4 and 3.5. The HDB presses well, and ignites and burns uniformly at all pressures. The Mix 22 burns with a zero pressure exponent, which is characteristic of thermites. By this technique, the compatibility problems of chemical reaction and unstable combustion of the HDB at high pressures are obviated. It should be noted that neither composition forms clinkers on combustion, the HDB because it is too gassy, and Mix 22 because it is too hot due to ZrO_2 boiling at 4590°K. However, it should be noted that the combustion products of Mix 22 form clinkers when mixed with the combustion products of HDB in the bipropellant configuration. This effect is described in Section 3.5.3.3 below.

3.5   Sub-Scale Motor Firings

3.5.1   General

The objective of the sub-scale motor firings was to determine a satisfactory separation technique between gases and solids for each of the candidate propellants. For these firings, two sizes of propellant grains were evaluated, one being 1-5/8" in diameter and the other being 2.5" in diameter. Both were cylindrical end-burners, inhibited on the circumferential surface and one end. The nominal grain length was 1". Since the effectiveness of filtration (or other separation technique) governs the mass discharge rate and therefore the combustion pressure, it was the practice to use oversized nozzles in first shots, with both filter design and nozzle throat size changed by steps to approach the desired value of combustion pressure. It is recalled that two values for discharge coefficient were given for each candidate in Table 3.11. They are discussed below.

TABLE 3.13

PROPERTIES OF HDB AND MIX 22

Property	HDB		Mix 22	
A. Composition, Wt. %	100	HDB	19.285	H_2WO_4
			54.612	Zr
			26.103	NH_4ClO_4
B. Theoreticals				
1. Flame Temperature, °K	1878		4590	
2. (H_2/HCl) molar	—		2.88	
3. Yield (H_2+HCl)				
Wt. %	16.9		4.39	
Vol. %	100.0		41.3	
4. Discharge coefficient, sec^{-1}.	(.00237) (.00554)		(0.00526) (0.0101)	
C. Compaction Density, gm/cc @ 30 KSI	0.837		3.18	
D. Burning Rate, in/sec, vs P (psia)	$0.70(P/1000)^{0.48}$		2.54 @ all values of P	
E. Sensitivity to Ignition				
1. Impact	41 kg-cm		125 kg-cm	
2. Friction	Neg (Esso Screw) Neg @ 90°, 400 psi		Neg (Esso Screw) Neg @ 75° 100 psi	
3. Electrostatic Discharge	0.0013 J @ 5000 V		.00135 @ 5200	

TABLE 3.14

COMBUSTION PRODUCTS OF TWO-COMPARTMENT HDB PROPELLANT

HDB				MIX 22		
SPECIE	CHAMBER	THROAT		SPECIE	CHAMBER	THROAT
BH2N	0.00009	0.00001		CL	0.06385	0.06463
NH3	0.00005	0.00001		HC1	0.09957	0.10410
BN8	3.34872	0.00048		H2	0.29424	0.29971
BH2	0.00022	0.00001		N	0.00053	0.00038
H2	8.37201	8.37296		NH3	0.00001	0.00001
BH3	0.00019	0.00002		N2	0.10961	0.11005
H	0.00078	0.00010		OH	0.01629	0.01252
N2	0.00018	0.00001		WCL	0.00008	0.00006
T °K	1877	1609		ZRCL	0.00220	0.00169
				ZRCL4	0.00002	0.00002
				ZRO2	0.00671	0.00547
				ZRO2°	0.54271	0.01171
				CL2	0.00006	0.00005
				H2O	0.02176	0.01863
				NH	0.00010	0.00007
				NO	0.00224	0.00159
				O2	0.00026	0.00016
				WCL2	0.02599	0.02386
				WO2	0.00114	0.00075
				ZRCL2	0.00140	0.00121
				ZRH	0.00008	0.00005
				H	0.29482	0.28954
				H2WO4	0.00001	0.00001
				NH2	0.00006	0.00004
				O	0.00900	0.00673
				W	0.00016	0.00010
				WO	0.00160	0.00110
				WO3	0.00003	0.00002
				ZR	0.00034	0.00021
				ZRCL3	0.00049	0.00045
				ZRO	0.04472	0.03515
				W°	0.04816	0.00313
				T °K	4608	4398

Figure 3.4. Burning Rate of HDB.

BURNING RATE, IPS

10
9
8
7
6
5
4
3
2.5
2
1.5
1

r = 2.54 IPS (Invariant with P)

Pressed at 30 KSI in steel

1   1.5   2   2.5   3   4   5   6   7   8   9   10   1.5   2   2.5   3   4   5   6   7   8   9   10
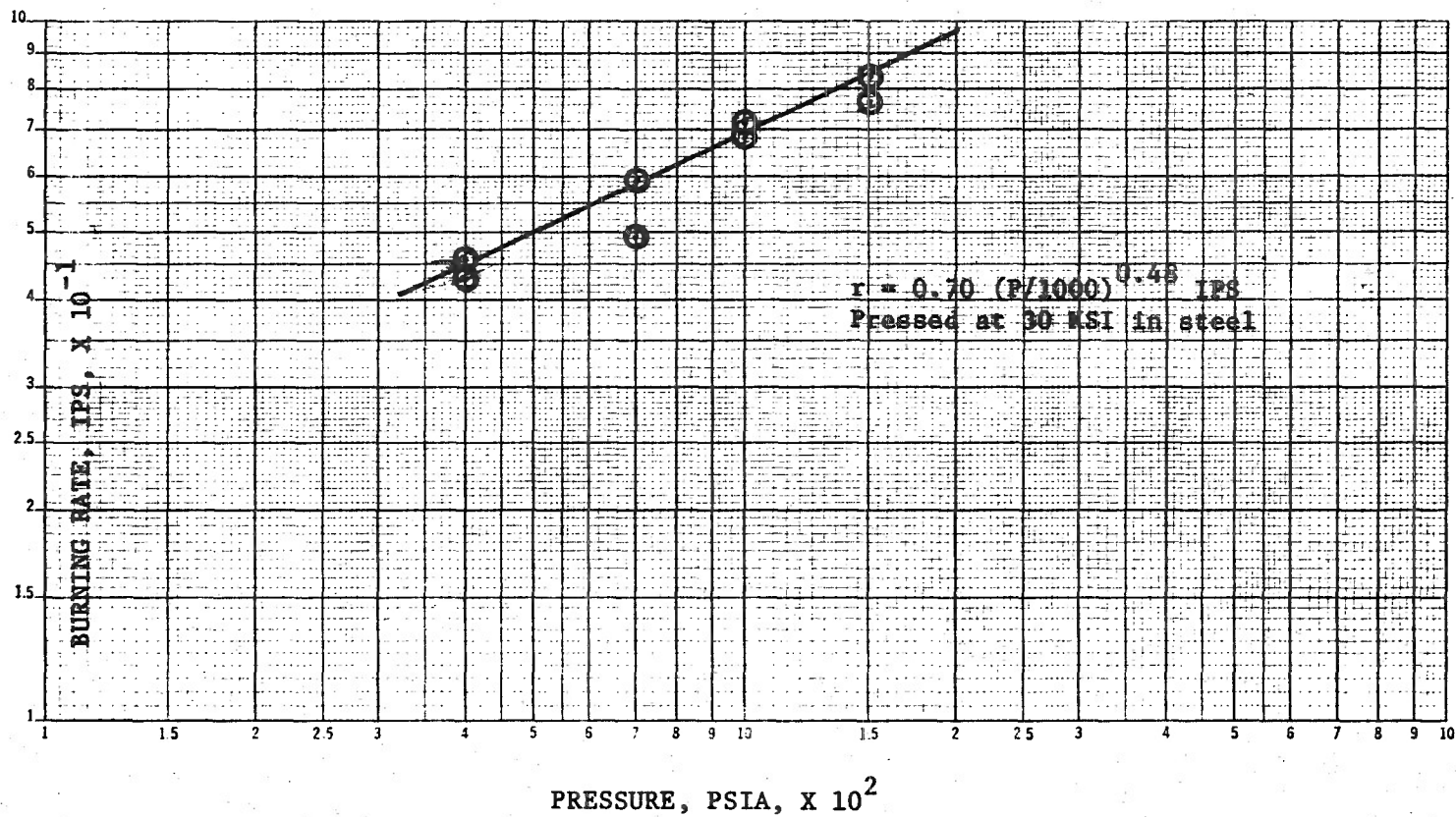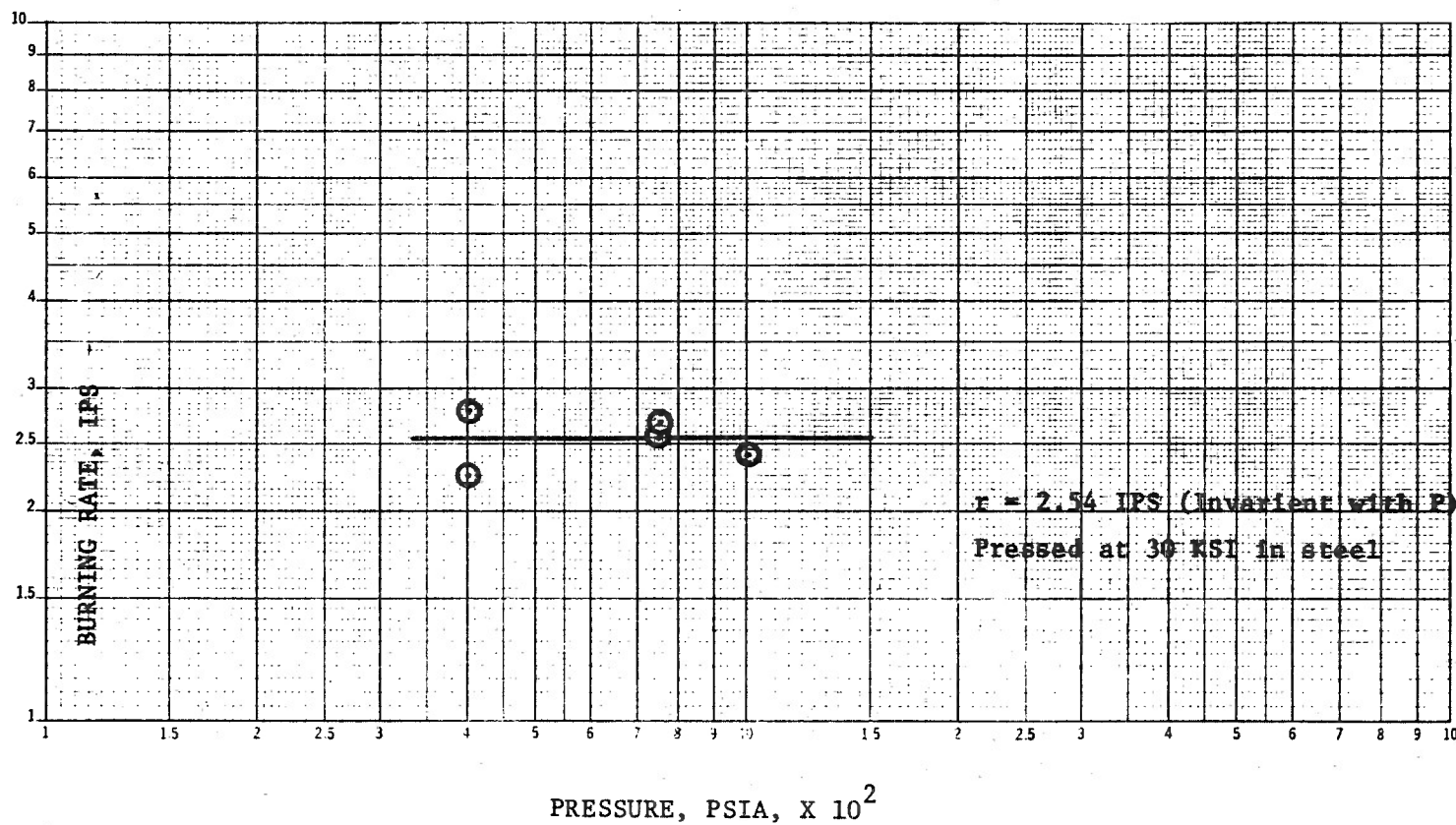
PRESSURE, PSIA, X 10^2

Figure 3.5. Burning Rate of Comp 22 - 19.285% H_2WO_4 + 54.612% Zr + 26.103% NH_4ClO_4.

For given values of propellant mass burning rate ($\dot{m}$) and combustion pressure (P_c), the nozzle discharge coefficient (C_D) is used to size the nozzle throat area (A_t) by means of the continuity equation,

$$\dot{m} = P_c \, C_D \, A_t \tag{1}$$

By continuity, $\dot{m}$ is also related to propellant burning surface area (S), burning rate (r), and density (ρ_p) and to the gas velocity (v_t) and density (ρ_g) at the throat:

$$\dot{m} = Sr\rho_p \tag{2}$$

$$= A_t \, v_t \, \rho_g \tag{3}$$

Combining Equation 1 and 3 yields

$$C_D = v_t \, \rho_g / P_c \tag{4}$$

For adiabatic combustion at an assigned value of P_c coupled with isentropic flow to sonic velocity, it is seen that C_D is thermodynamically derived. For the motors of interest, it is determined from only the gaseous combustion products which are ejected from the motor, since the condensed species are assumed to be retained within the motor as a clinker or a filter cake. For this case of uncoupled flow (gas only), the derived values of C_D are the first-reported numbers in Table 3.11. In the event that the condensed species are ejected from the motor because no clinker is formed or because of failure of the filter system, than a higher value of C_D is computed. These values are reported in parenthesis in Table 3.11 and represent an upper limit on the theoretical value for this parameter. In this case (coupled flow, i.e., gas and solids), considerably greater values of P_c are computed for a given value of A_t/S. Combining equation 1 and 2, and expressing $r = kP_c^n$, then

$$\left(\frac{P_c, \text{ coupled}}{P_c, \text{ uncoupled}} \right) = \left(\frac{C_D, \text{ uncoupled}}{F \cdot C_D, \text{ coupled}} \right)^{\frac{1}{1-n}}$$

where F = mass fraction of gaseous combustion products.

For compositions 3.3.4, 3.8.1, and 3.8.8, the P_c ratios are 6.26, 9.55 and 8.03, respectively. Thus, for a given value of A_t/S computed on the basis of uncoupled flow (which is the desired phenomenon), very high pressure rises can occur if the propellant does not clink or if the filter system fails. This is why a step-wise approach was taken in sizing the throat for the motor firings.

3.5.2   Sub-scale Motor Configurations

The motor hardware that was constructed was comprised of a heavy-wall case and closures, with a filter housing located between the combustion chamber and nozzle throat.   The intent was to allow for maximum flexibility in filter bed configuration and propellant mass burning rate.   Of the three candidate propellants, 3.8.1 clinks best when burned.   For this composition, a simple filter bed comprised of tungsten screens was evaluated.   This configuration is shown in Figure 3.6.

At the other extreme, composition 3.8.8 forms no clinker, and the solids content of the combustion products is 82.7% by weight.   For this composition, cyclones or centrifugal separators are best.   Attributes of cyclones include simplicity of design and operation, while centrifugals offer a more compact design envelop.   Re-entrainment of particles is a phenomenon peculiar to both techniques, since high gas velocities are involved.   For the cyclone, a tangential velocity on the order of 200 ft/sec is required for separation of 10-μ particles in the sub-scale envelop (3" dia).   For this reason, either an impingement separator or filter bed located upstream of the nozzle outlet may be required to remove residual solids.   Cyclones and centrifugals can both be operated at high pressure. The principal drawback of the cyclone is size, while that of centrifugals is the need for an external power source to drive the turbine and the increased mechanical complexity. It should be noted that centrifugation is an extremely effective technique for solids removal.   In previous work performed with spinning motors, complete removal of condensed combustion products (Al_2O_3 (ℓ), $C(c)$, and $B(\ell)$ was obtained for a 6-inch diameter motor spinning at 900 rpm (centrifugal force $\approx$70 g's).   The centrifugal effect for a full-scale motor probably can be attained by either spinning the motor, as above, or (more conventionally) by spinning the combustion products by means of a rotoclone, or cinder fan.   For compositions 3.8.8 and 3.3.4, a cyclone separation chamber was employed, primarily because of design simplicity and ease of use at high pressure.   This motor configuration is shown in Figure 3.7.   The cyclone effect is imposed on the combustion products by the deflector plate located above the propellant burning surface to direct the flow tangentially along the motor wall.   A re-entrant nozzle tube was employed to minimize the effects of re-entrainment.
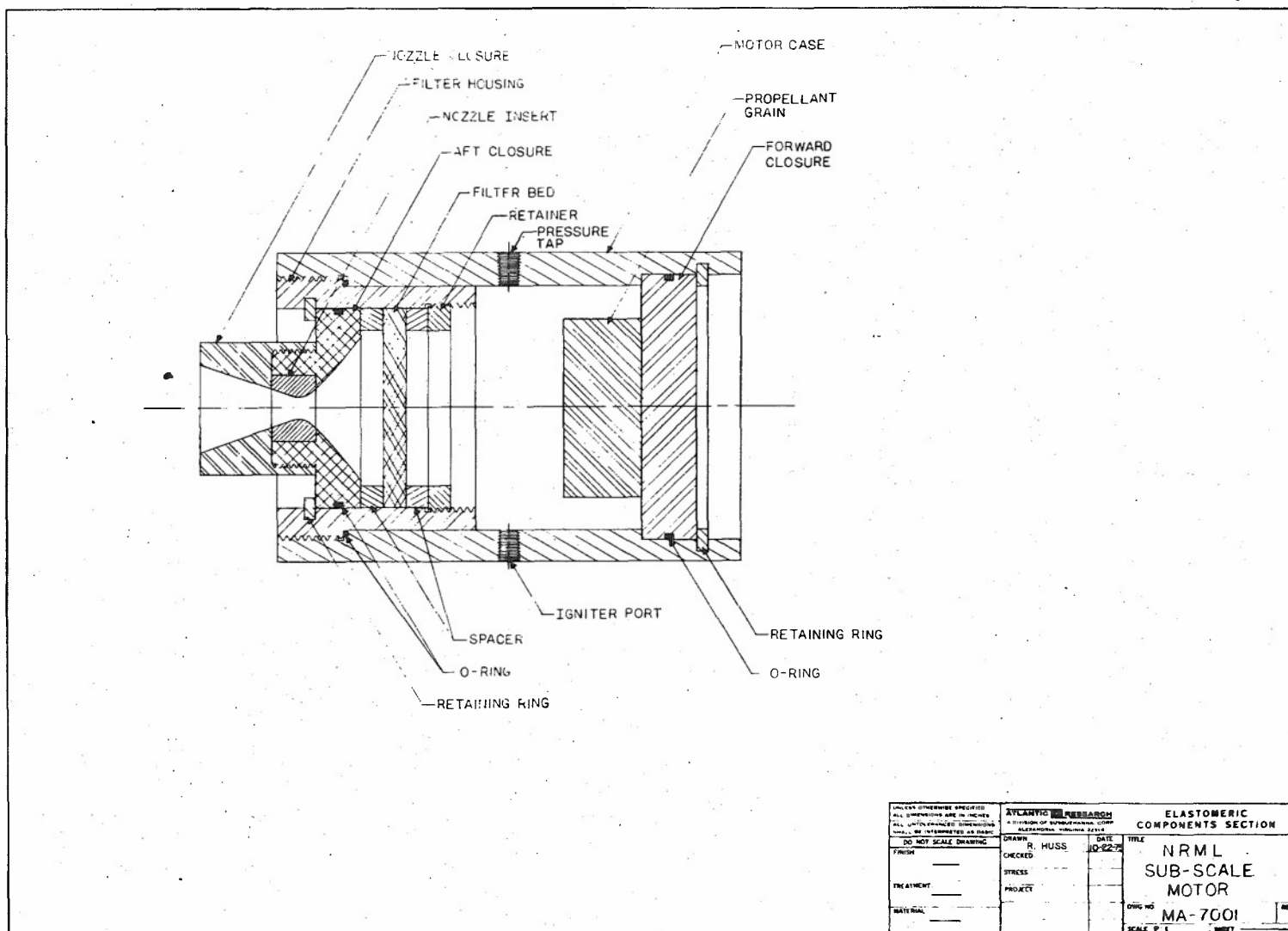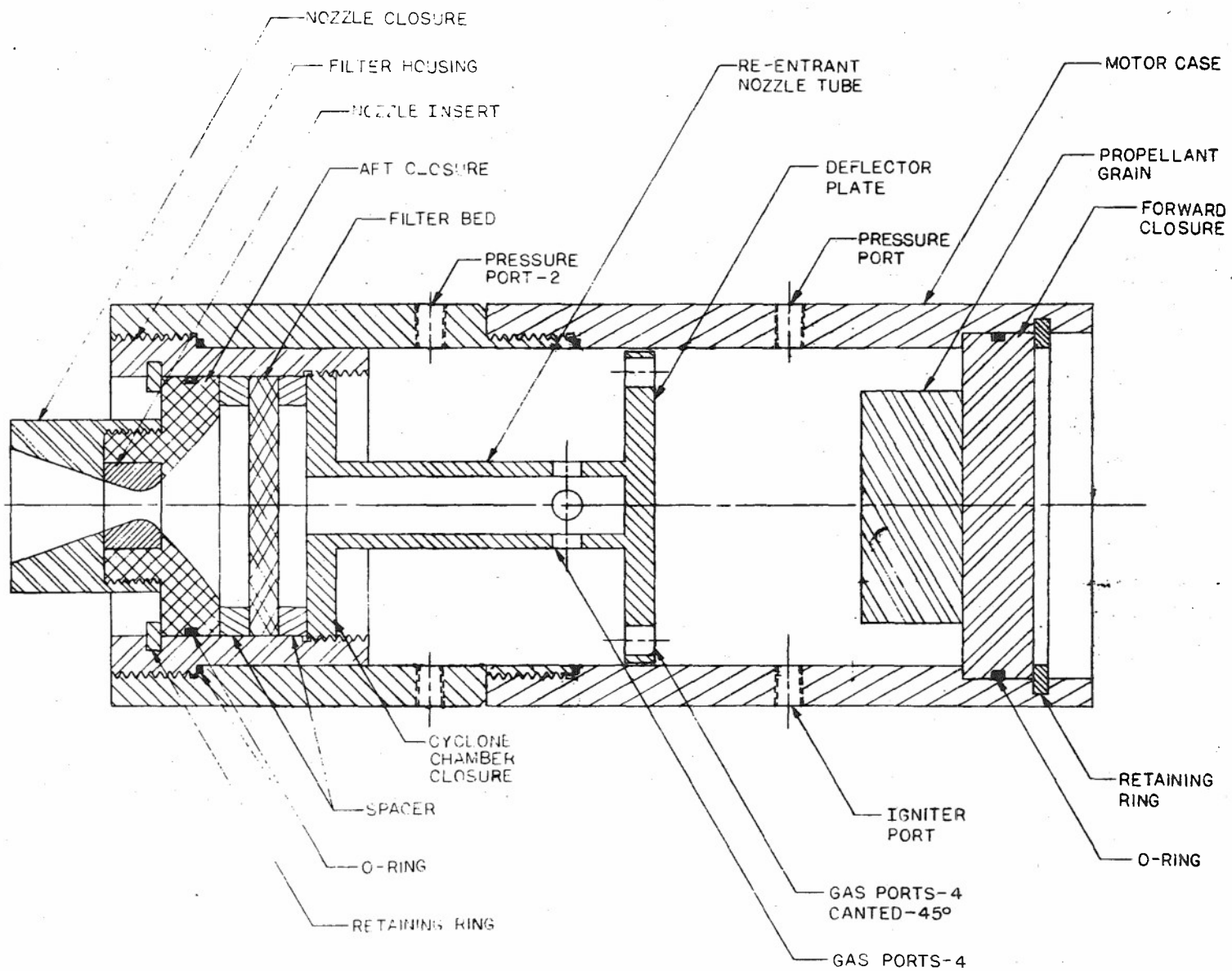
NOZZLE CLOSURE
FILTER HOUSING
NOZZLE INSERT
AFT CLOSURE
FILTER BED
RETAINER
PRESSURE TAP

MOTOR CASE
PROPELLANT GRAIN
FORWARD CLOSURE

IGNITER PORT
SPACER
O-RING
RETAINING RING
RETAINING RING
O-RING

ELASTOMERIC
COMPONENTS SECTION

ATLANTIC RESEARCH
A DIVISION OF SUSQUEHANNA CORP
ALEXANDRIA, VIRGINIA 22314

DRAWN R. HUSS   DATE 10-22-75
CHECKED
STRESS
PROJECT

NRML
SUB-SCALE
MOTOR

DWG NO MA-7001   REV

SCALE 2:1   SHEET

FIGURE 3.6

Figure 3.7. Motor in Cyclone Chamber.

3.5.3   Subscale Motor Firing Results

3.5.3.1   Composition 3.8.1 (H_2WO_4/ZrH_2/$Zr(OH)_4$/NH_4ClO_4)

The simplest motor configuration, that is shown in Figure 3.6, was used for these firings. The propellant forms excellent clinkers when burned, so that the only filter arrangement was comprised of 3 tungsten screens in series located in the filter housing. The screens are 1.60" diameter x 4 mil x 24 mesh, spaced 1/4 inch apart in series. Firing results are given in Table 3.15. Initial firings were oversized nozzles. It is seen that as P_c increases, the residue weight increases. Very little ash was found on the screens indicating a clean gas situation. Burn rates were difficult to measure from the motor firings at the lower values of D_T, because the ratio of motor volume to D_T is very large (motor volume $\simeq$ 350 cc), and the pressure decay times are significant fractions of the burn time. For no heat losses the rate at which pressure in the motor chamber decays to ambient is derived from the Perfect Gas Law and the continuity equation:

$$\frac{dP}{dt} = -\frac{RT}{V}\frac{dn}{dt}$$

$$= -\frac{RT}{V}\frac{P\ C_D A_t}{(MW)}$$

where

P	= Pressure in the chamber	t	= Time
T	= Temperature of the gas	R	= Gas constant
n	= Number of moles of gas	V	= Volume of chamber
		MW	= Molecular weight of gas

For firings 10-5, -6 and -7, the total burn times were 6.26, 6.12 and 6.52 sec, respectively; and the computed decay times are 0.22, 0.59 and 1.44 sec, respectively; resulting in computed burn times of 6.26 - 0.22 = 6.04, 5.53, and 5.08 sec, respectively. The tabulated burning rates, which are plotted in Figure 3.3, are based on the computed times and are seen to agree very well with strand data.

TABLE 3.15

Subscale Motor Firing Results: Composition 3.8.1 ($H_2WO_4/ZrH_2/Zr(OH)_4/NH_4ClO_4$)

Firing Number	Grain Dimensions Dia(in) x L(in) x Wt(gm)	Nozzle Throat Diameter D_t, in	Filter Configuration	P_c, psia	Average* Burn Rate ips	Residue, % of Theoretical	Remarks
10-1	2.512 x 0.586 x 122.6	0.402	3 W screens	Ambient	–	81.5	Ambient burn
10-2	Igniter shot						
10-3	1.688 x 0.845 x 98.4	0.128	3 W screens	55	–	93.0	3-sec ignition delay
10-4	1.688 x 0.860 x 99.4	0.089	3 W screens	197	–	100.0	See text
10-5	1.688 x 0.842 x 98.5	0.069	3 W screens	200	0.14(0.14)	99.7	See text
10-6	1.688 x 0.858 x 101.5	0.048	3 W screens	294	0.155(0.15)	97.0	See text
10-7	1.688 x 0.845 x 98.5	0.033	3 W screens	631	0.17(0.185)	98.5	See text

*Computed from the quotient web ÷ computed burn time (see text). Numbers in parenthesis are from strand data (see Figure 3.3).

93

3.5.3.2 Composition 3.3.4 ($NH_4NO_3/ZrH_2/Zr(OH)_4/NH_4(CO_4)$)

Results of these firings are given in Table 3.16. In the first firing, 9-1, the motor configuration of Figure 3.6 was used. The filter configuration was comprised of 3 Tungsten screens, 1/6" diameter x 4 mil x 24 mesh arranged in series 1/4 inch apart. The firing trace was very erratic and characterized by two pressure peaks. Post-firing inspection indicated the screens had been ruptured. It is known that the composition does not clink well at low pressures, and apparently the screens filled and ruptured, causing the second pressure peak. The average pressure is a poor value, and the resultant burning rate is therefore also poor.

In the second motor, also based on the 3.6 configuration, the filter housing was outfitted with three baffles made of 5 mil tungsten sheet and followed by a tungsten screen. The spacing between each baffle was 1/4 inch. The baffles were 1.6-inch dia discs with a 1/4 inch segment removed, each segment located on opposite diameters so that the flow through the baffles was serpentine. Post-firing examination revealed that the baffles were bent concave in the direction of flow, that the void space between baffles was filled with residue, and that the screen had become filled and ruptured above the open segment of the last baffle. The motor pressure had built up gradually to a value of 1500 psia 0.4 sec after ignition and dropped instantaneously to ~400 psia and remained at approximately this value for the remainder of the firing (0.4 sec). Apparently, the rise to the pressure spike is due to filling the baffles and screen, and the drop to operating pressure is due to failure of the screen after it had become completely filled. As above, the average pressure is not a very good one, due to the spike, and therefore the motor and strand burning rates, which are shown in Figure 3.2, do not agree well.

These firings indicate that the propellant does not clink well enough to permit the use of a simple filter configuration. For this reason, the remainder of the firings were carried out with the motor configuration of Figure 3.7, which includes a cyclone chamber and re-entrant nozzle. Firing 9-3 was carried out with this motor and the same filter configuration of 9-2. Even though the $\overline{P}_c$ was lower, the retention of residue was considerably better, and the agreement between motor burning rate and the strand value improved. For this firing, most of the residue was caught in the cyclone chamber. None was found between the baffles nor on the screen, both of which were intact and not deformed or ruptured as in the previous firings. Evidently,

TABLE 3.16

Subscale Motor Firing Results: Composition 3.3.4 ($NH_4NO_3/ZrH_2/Zr(OH)_4/NH_4ClO_4$)

Firing Number	Grain Dimensions Dia(in) x L(in) x Wt(gm)	Nozzle Throat Diameter D_t, in	Filter Configuration	Average P_c, psia	Average* Burn Rate ips	Residue, % of Theoretical	Remarks
9-1	2.50 x 0.947 x 194.2	0.334	Figure 3.6; 3 W screens	300	0.86(0.33)	55.1	Screens failed
9-2	2.51 x 0.481 x 97.7	0.250	Figure 3.6; 3 W baffles 1 W screen	400	0.60(0.36)	67.3	Screens failed
9-3	1.688 x 0.564 x 5-.3	0.099	Figure 3.7; 3 W baffles 1 W screen	264	0.40(0.32)	93.5	See text
9-4	1.688 x 1.076 x 97.22	0.067	Figure 3.7; ZrO_2 matt and W screen	335	0.43(0.35)	100	See text
9-5	1.688 x 1.061 x 96.61	0.055	Figure 3.7; ZrO_2 matt and W screen	627	0.50(0.42)	98.7	See text

*Computed from the quotient web ÷ burn time, Numbers in parenthesis are from strand data (see Figure 3.2).

the cyclone chamber is very effective in removing the solids from the combustion products.

The next two firings were also made with the re-entrant motor and with ZrO_2-fiber filter matt supported by tungsten screens in the filter housing replacing the baffle screen arrangement of the previous firings. For these firings, retention of the slag is essentially quantitative. In all three motor firings (9-3, -4, and -5), the motor burning rates are significantly greater than the strand rates ($\sim$20%). The reason for this is unexplained. It is possible that the grain breaks up near burnout, resulting in apparently shorter burn times. This could be due to inhibitor failure which consisted of a thinly painted coat of titanium dioxide filled epoxy.

3.5.3.3 Composition 3.8.8 (H_2WO_4/Zr/HDB/NH_4ClO_4)

As reported previously, this composition exhibited combustion instability when burned at 1500 psia. The possibility exists that pressure spikes occurring at ignition can trigger explosions instead of uniform combustion, so that no attempts were made to burn pellets of this composition in motors. Therefore, the bi-propellant two-compartment approach was taken, and motors comprised of HDB pellets and Composition 22 pellets were made up. The web lengths of the pellets were sized to permit equal burning times, based on strand data, and the relative number of pellets was governed by the required mass burning rates (39.97% HDB + 60.021% Composition 22). The motors were comprised of 10 pellets of HDB of dimensions of 0.5" diameter x 0.2" L x 0.52 gm weight, and one pellet of Composition 22, 0.5" diameter x 0.87" L x 8.9 gm weight. The pellets were inhibited on one end and the circumferential surface and functioned as end burners in the motor configuration of Figure 3.7 (cyclone chamber and re-entrant nozzle).

Three motors were fired. Because of the small amount of propellant, residue weights could not be measured accurately. Firing results (P_c vs D_T) are given in Table 3.17. The first motor was "fired for effect." The next two were fired with D_T = 0.10 inches, the 8A-2 with a ZrO_2 fiber matt filter supported by a tungsten screen and the second (8A-3) with two ZrO_2 matt filters in series, each supported by a tungsten screen and separated by 1/4 inch. In the first firing (8A-2) post firing observation indicated a light fluffy ash (BN) throughout the combustion chamber, cyclone chamber, and re-entrant tube.

- 84 -

TABLE 3.17

Subscale Motor Firing Results: HDB + Composition 22 (H_2WO_4/Zr/NH_4ClO_4)

Firing Number	Nozzle Throat Diameter , in	Filter Configuration	Average Pressure P_C, PSIA
8A-1	0.237	Motor 3.6, screen only	80
8A-2	0.100	Motor 3.7, ZrO_2 Matt + W Screen	575
8A-3	0.100	Motor 3.7, 2 ZrO_2 Matts + W screens	560

The combustion chamber also contained an acorn-sized metallic clinker weighing 3.7 gm, which was the residue from Composition 22. The filter and screen were intact.

The residue from 8A-3 was very similar to the above, but the filters had been bent. Apparently the use of two filters gives rise to a value of ΔP across the filters that is too high. Since there was no difference in the amount of residue on the filters between the second and third test, one filter would prove sufficient.

The motor firing traces for firing 8A-2 and 8A-3 are shown in Figure 3.8a and 3.8b. As can be seen from the traces, the chamber pressure is essentially constant. Thus, even though the HDB is tempermental when combined with other ingredients, in a two-compartment motor the ballistic properties of this system are excellent.

Theoretical calculations of the propellant combustion products have been made and have been compared with experimental values. The experimental procedure used in the analysis was to combust small pressed propellant samples in a stainless steel bomb. The interior of the bomb and all exposed metal surfaces were sandblasted, cleaned with trichloroethylene, then teflon coated. The teflon coating was primarily used to prevent absorption of HCl on cold metal surfaces – a phenomenon observed under previous programs. Before and after teflon coating, the bomb was baked out in an oven overnight at 800°F to remove any absorbed gases. All fittings, valves and transfer tubing was constructed of teflon or a similar HCl unreactive plastic.

The bomb was purged a minimum of 5 times with argon and vacuum pumped between purges to ensure no contamination with residual air. Bomb volume was exactly measured via displacement and the propellant weight recorded. Ignition was carried out by a hot wire technique, to avoid any introduction of contaminating gases, under one atmosphere of argon. Upon cooling, a plastic syringe sampled gases through a septum fitted directly to the bomb and transferred the gases directly to a calibrated gas chromatograph for analysis. Transit time and residence time in the bomb were minimized. The results of a gas chromatograph of the sample gave results that essentially agreed with predicted thermochemistry calculations.

Burn Time = 0.37 sec versus 0.34 from strands
$\overline{P}$ = 575 psia

Grain Configuration:

10 HDB pellets 0.2 in. L X 0.495 dia.
1 Comp. 22 pellet 0.87 in. L X 0.495 dia.
All pellets end burners burning on one end
Total propagation weight = 14.1 gm

Motor Configuration:

Re-entrant nozzle with cyclone chamber
One ZrO_2 fiber mat filter with tungsten screen
D_T = 0.1 in.

Post-firing Configuration:

Comp. 22 clinker in combustion chamber. Bn is uniformaly
distributed in combustion cyclone, and re-entrant chambers.
Filter, filter cake (Bn) and screen are intact.

Figure 3.8a

Figure 3.8b

FIGURE 3.8   MOTOR FIRING TRACES

3.6 SUMMARY
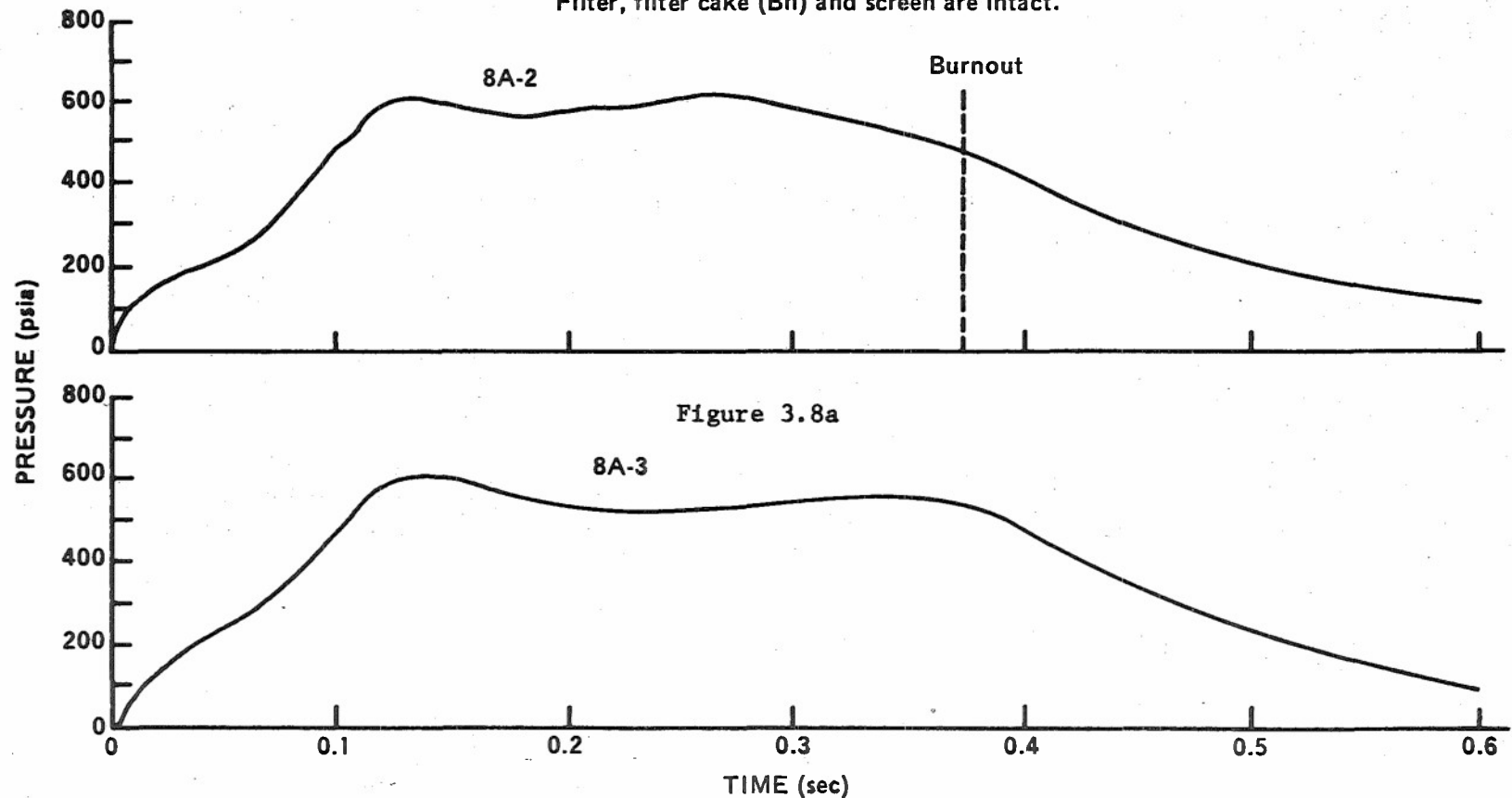
The objective of the solid propellant technology effort was to select and characterize three solid propellant candidates. Selection was based on the results of calculations of theoretical flame temperature and combustion product composition. For these calculations, propellant ingredient selection was constrained by state-of-the-art solid propellant chemistry. Successful sub-scale motor firings (1/4 lb nominal propellant weight) were carried out for all three candidates. Design factors for filtration and particle separation techniques for each candidate were delineated.

Of the three candidates, the first represents the best clinker propellant. This propellant is comprised of H_2WO_4, ZrH_2, $Zr(OH)_4$, and NH_4ClO_4, has a flame temperature of 2799°K and an (H_2 + HCl) yield of 2.59% by weight at 98.0% gas purity and H_2/HCl = 32.6 (molar). A simple filter comprised of a tungsten screen was found to be satisfactory for retaining entrained solids in the combustion products. Typical clinker weight >99% of theoretical values were measured for this propellant. The second propellant represents the best attainable from state-of-the-art ingredients. The propellant is comprised of NH_4NO_3, ZrH_2, $Zr(OH)_4$, and NH_4ClO_4, has a flame temperature of 2801°K, and an (H_2 + HCl) yield of 3.84% by weight at 89.5% gas purity and H_2/HCl = 38.2 (molar). Although this propellant does not form clinkers as well as the H_2WO_4 system, clinker weights >99% of theoretical were attained through the use of a cyclone chamber and a filter bed comprised of ZrO_2 fiber matt. A similar particle separator/filtration technique was used satisfactorily for the third propellant which is the best attainable from use of advanced propellant ingredients. This propellant is comprised of H_2WO_4, Zr, HDB and NH_4ClO_4, has a flame temperature of 2808°K, and an (H_2 + HCl) yield = 10.8% by weight at 95.9% gas purity and H_2/HCl = 33.3 (molar). In this propellant, HDB (hydrazine diborane) is the coolant. HDB is a compound that is easily synthesized and is available on special order. The motor firings for this propellant are especially unique because a bipropellant grain configuration was used in the motors due to the reactivity during combustion of HDB with NH_4ClO_4. One grain was comprised of H_2WO_4, Zr, and NH_4ClO_4 while the other was comprised of only HDB. The firings yield uniform combustion and pressure time traces, and the filtration system withstood the firing conditions without damage.

The high values of yield and purity of (H_2 + HCl) offered by use of HDB in propellants leads to the conclusion that additional work with this and possibly other HDB propellants is warranted. Synthesis of additional HDB is needed to permit propellant evaluation with a single lot of HDB, eliminating batch effects. Scale-up firings should be made, with the emphasis on BN(c) separation. The combustion products of $H_2WO_4/Zr/NH_4ClO_4$ form a good clinker when admixed with the auto-combustion products (H_2, BN) of HDB, and for this reason the use of a cyclone or centrifugal separator for only HDB combustion products minimizes the envelope and mechanical impact on the system as well as the heat sink effect of the filter hardware.

4.0   PROOF EXPERIMENT AND LASER SYSTEM CHARACTERISTICS

The end objective of the work described in this report is to develop an H_2-HCl laser device. Prior to design of such a device, it is anticipated that a laser proof experiment will be performed. The objective of the proof experiment is to experimentally determine laser performance at conditions that are of practical interest. The current phase is concerned with determining a low risk approach for the proof experiment and to develop the techniques that will be used in design of the proof experiment hardware.

An early objective of this task was directed at obtaining performance maps as a function of gas composition, chamber conditions, and nozzle contour. The one-dimensional harmonic oscillator program was used to generate these maps using the vibrational kinetics for the H_2/HCl system listed in Table 2.2. These calculations provided (i) a limited performance optimization, (ii) a base line performance for conditions expected to be achievable by propellant technology, and (iii) some effects on H-atom performance degradation.

Some preliminary performance sensitivity studies on stagnation and gas expansion conditions has been described in Phase I. It was shown that best performance was obtained at highest stagnation temperature (neglecting atom effects). However, it was also determined that there was an optimum value of $p_o h_{th}$ where p_o in stagnation pressure and h is the nozzle throat height. This effect is similar to that observed in the CO_2/N_2 GDL and is easily explained in terms of the H_2 vibrational energy freezing criterion. In addition, it was shown that maximum performance occurred at lowest HCl concentrations. This latter conclusion may be expected to be modified in favor of larger HCl concentrations in the A.H.O. model and when cavity power extraction is included in the modeling.

Some additional calculations illustrating the points mentioned above are given in Figures 4.1 and 4.2. It is seen that maximum available energy occurs at [HCl] $\sim$2% for the smaller throat height and P_o = 50 atm. At the higher stagnation pressure the throat height has a large effect on the performance whereas at the lower chamber pressure the performance is less sensitive. This effect is similar to that which occurs in the CO_2 GDL where performance drops off at large values of the parameter $p_o h_{th}$.
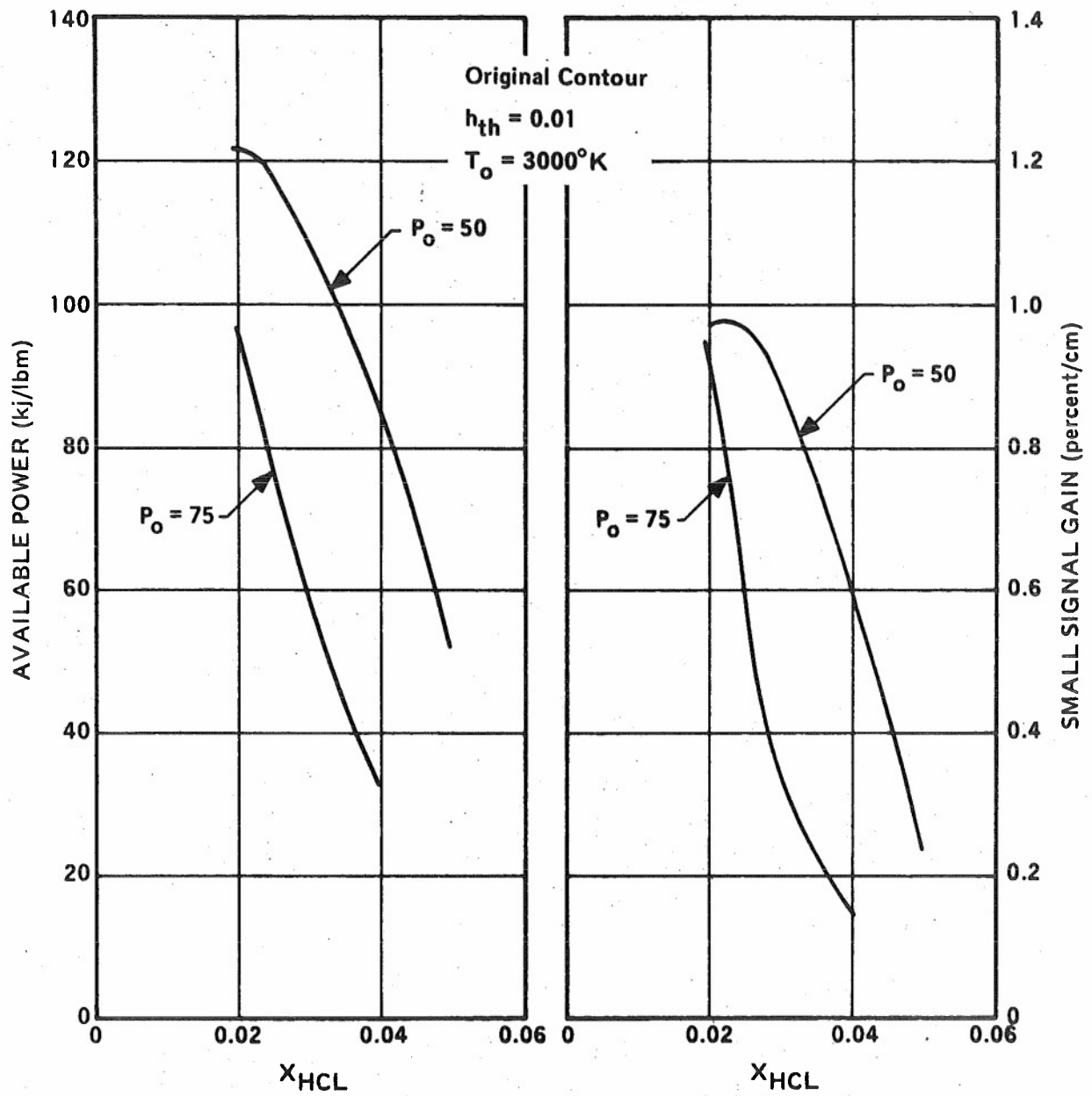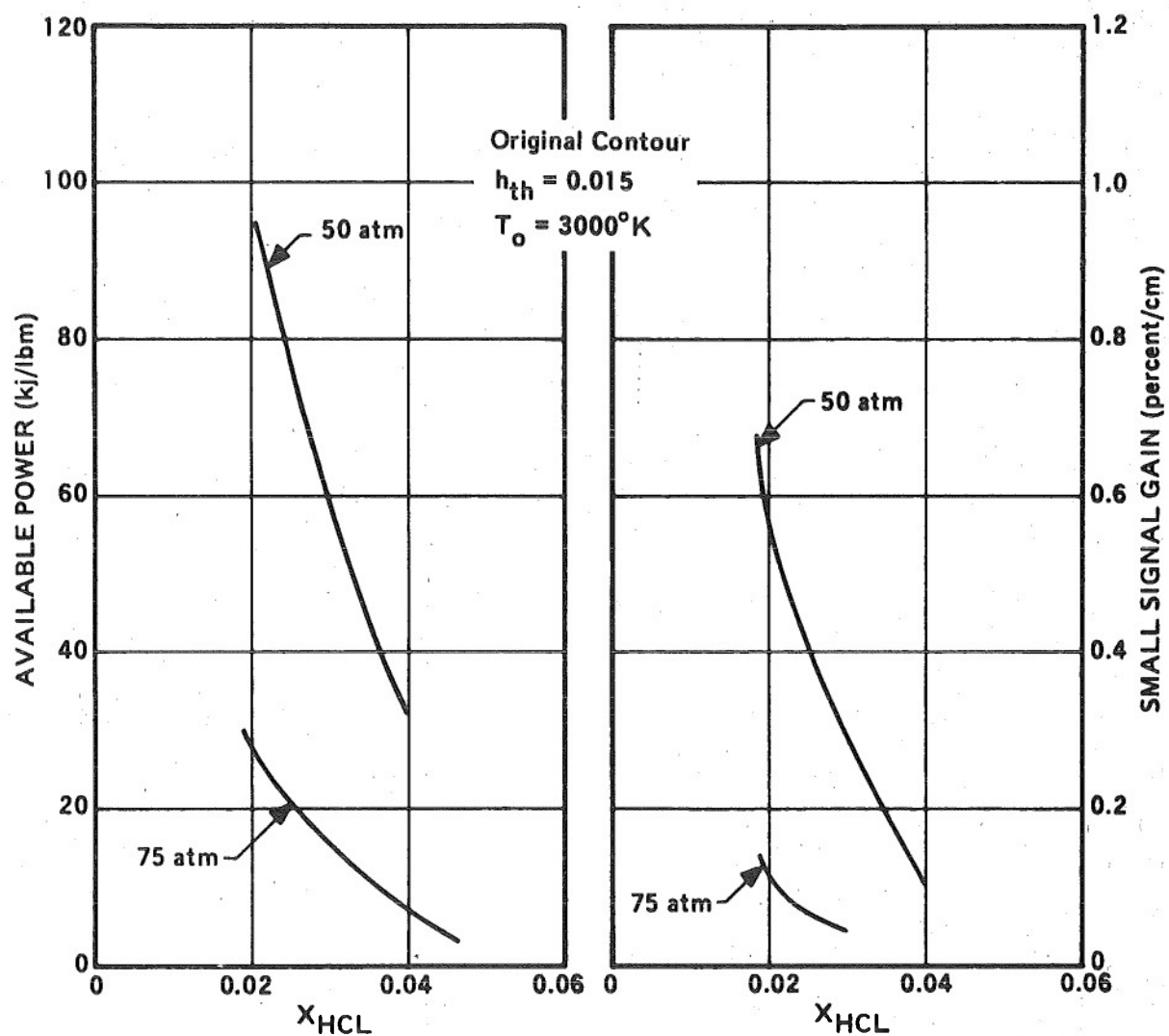
Figure 4.1

Figure 4.2

Some calculations were also performed using various assumed nozzle contours (or gas density distributions). The assumed density distributions are shown in Figure 4.3. Results of this limited study is Table 4.1. It is clear that some improvement in performance is possible by suitably tailoring the nozzle contour to maximize $H_2 \rightarrow HCl$ V$\rightarrow$V pumping. This study was not pursued further pending resolution of the basic kinetics of the H_2/HCl system.

Another technique was used to estimate the optimum area ratio for GDL performance. A calculation was performed comparing the characteristic reaction times for the various vibrational energy transfer processes. An isentropic flow was used to calculate the thermodynamic state associated with each expansion ratio starting from some assumed stagnation conditions. The characteristic time of the reaction is equivalent to the vibrational relaxation time for that process at the particular temperature and density that result from the expansion. An example of such a comparison is shown in Figure 4.4. Also in Figure 4.4. is a dashed line that indicates the time for an expanded gas sample to traverse a one meter long cavity. For an efficient device we wish the V$\rightarrow$V transfer reaction time to be short compared to the cavity flow time and in turn shorter than all V$\rightarrow$T deactivation processes. It can be seen that in Figure 4.4 this criterion occurs generally for A/A* < 30. Calculations like this were performed for a variety of concentration ratios and stagnation conditions to develop insight into optimum expansion ratio for H_2/HCl vibrational pumping.

The results of this analysis is shown in Figure 4.5. The available energy in the HCl at a distance of 100 cm from the throat is given as a function of area ratio for several HCl concentrations. Energies greater than 100 kJ/lb are obtained for HCl mole fractions of 0.01 - 0.02 for A/A* $\sim$ 50. This result is comparable to the previous results in the sense that it gives a rough estimate for the nozzle expansion ratio. It is also apparent from this limited optimization study that the stagnation temperature would be lowered to 2800°K where the propellant technology is more practical with no performance degradation. It was recognized in the Phase I feasibility study that H-atoms which occur at the high stagnation temperature and freeze during the rapid expansion can seriously degrade calculated performance by rapidly deactivating HCl. During this program a series of calculations was performed at successively lower stagnation temperature. Of course, it was expected
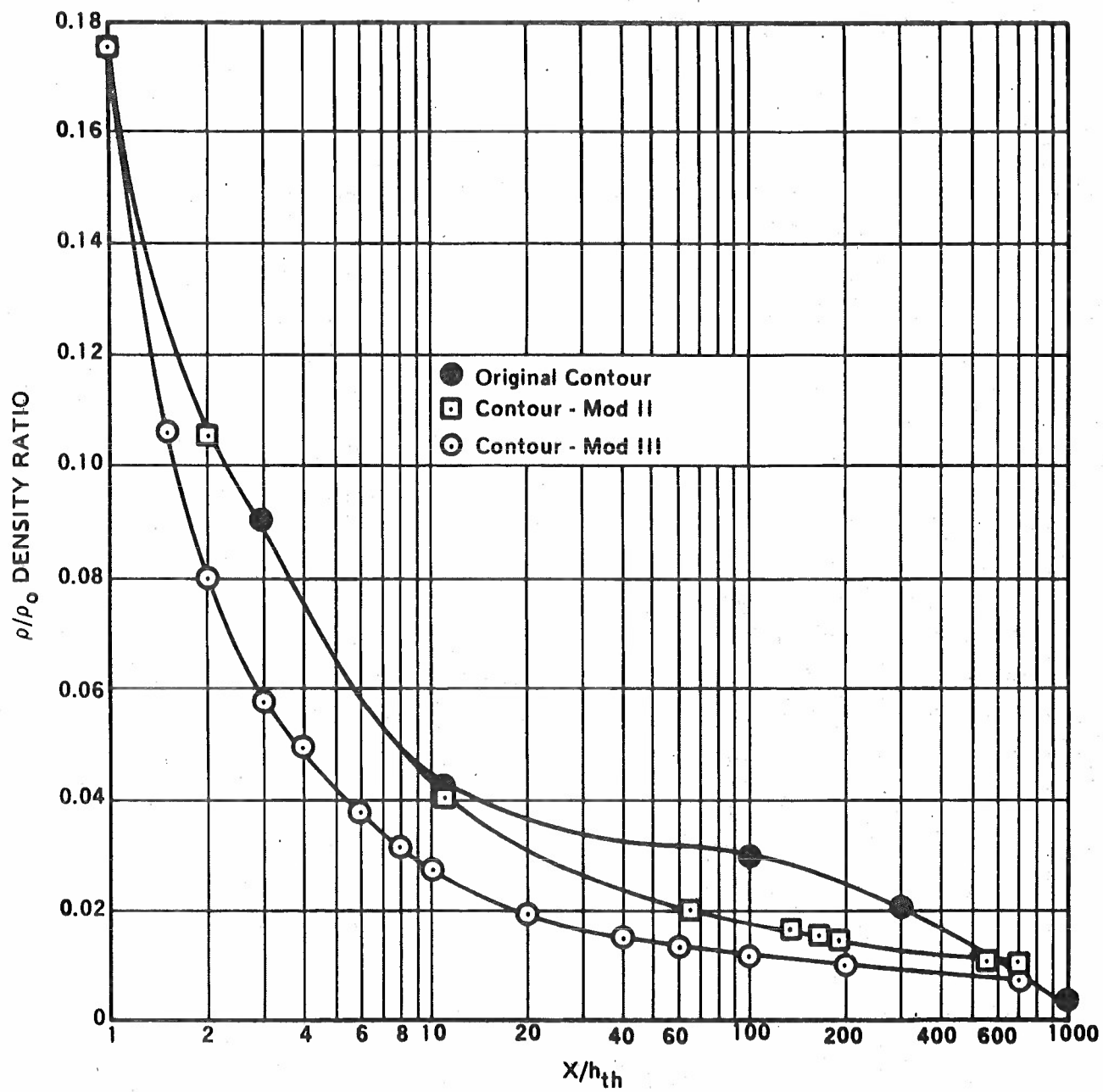
Figure 4.3

TABLE 4.1

Initial conditions: $T_o = 3000°K$, P_o atm, $[HCl] = 0.02$

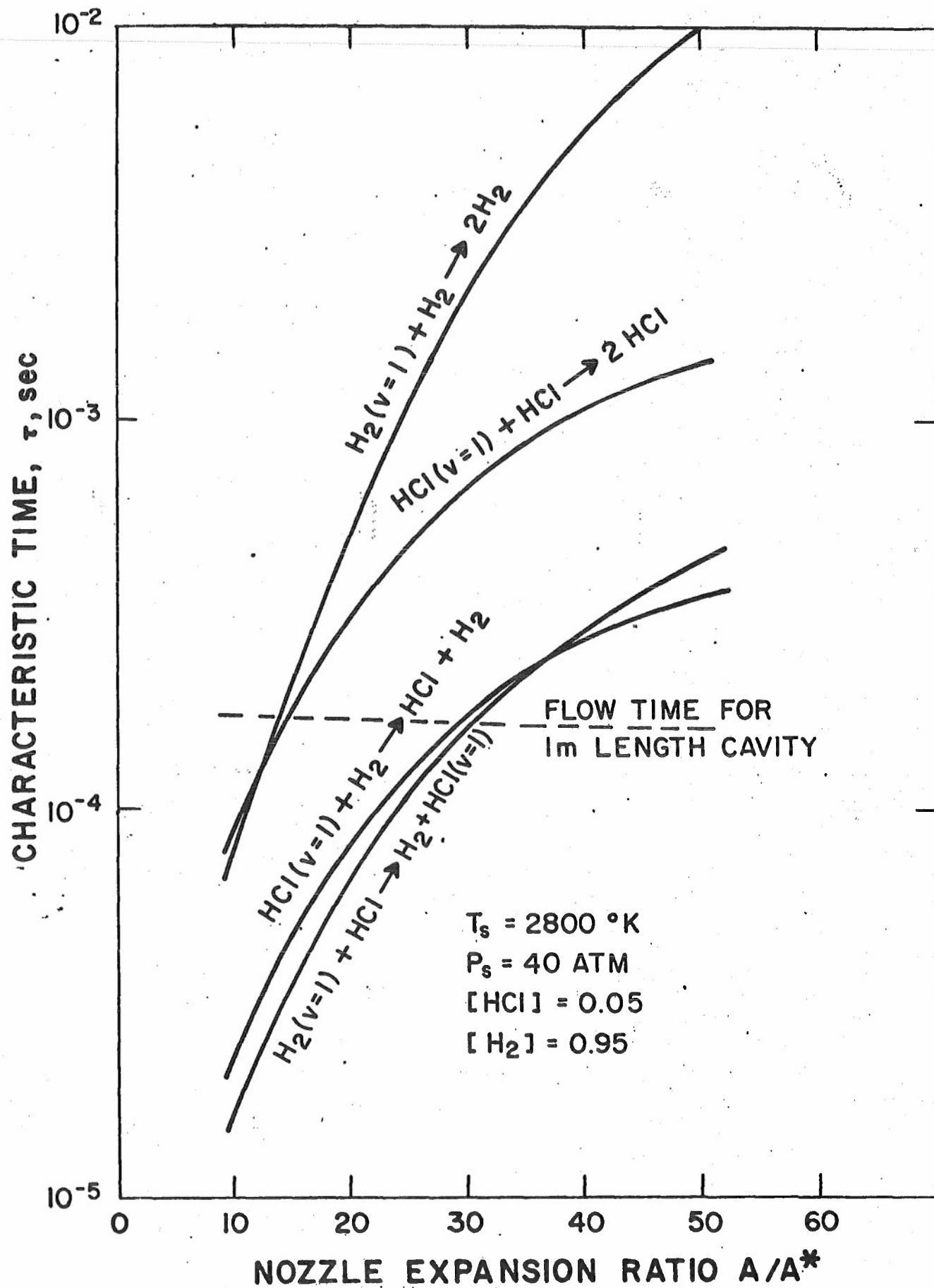| Contour	Available Energy kJ/lb
old	93
I	109
II	116

Figure 4.4   Characteristic Times for Various Energy
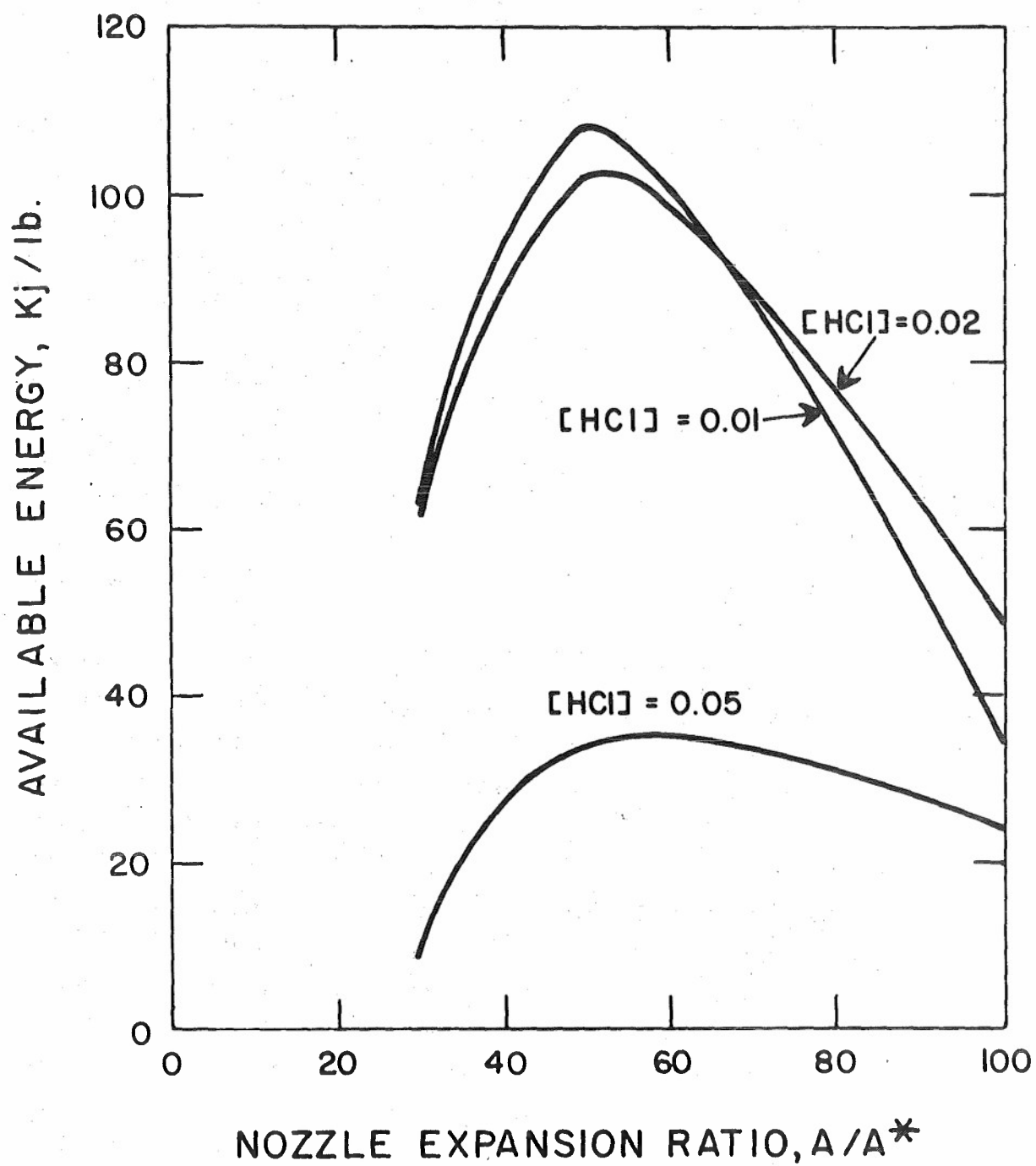Transfer Processes as a Function of Expansion Ratio.

Figure 4.5 Optimized performance map for
baseline condition of $T_s = 2800^\circ K$
and $P_s = 40$ atm.

that specific energy would decrease, but, at the lower T_o, H-atoms would also decrease and have less effect of performance.

The method employed was to systematically modify the nozzle contour and observe the change in the vibrational temperature of HCl versus axial distance. At temperatures of 2400°K and 2300°K, the specific power computed is 45 kJ/lb and 25 kJ/lb, whereas the gain is .55%/cm and .35%/cm, respectively. Although these values are not as attractive as the values obtained at the higher temperatures, the effect of H-atoms at 2300°K is estimated to be negligible. Thus, from the point of view of a low risk proof experiment a stagnation temperature of 2300°K appears to be a good choice.

These estimates use the equilibrium throat value of H-atoms. The area ratio of the resulting nozzle giving the best performance was 15. For a throat height of .01 cm, the overall length of the nozzle is 2 cm. Since the nozzle has such a low area ratio, a slight increase in gain can be obtained without significant degradation of pressure recovery by placing an additional expansion downstream of the nozzle. The vibrational temperature of HCl for this case is shown in Figure 4.6 along with the results of other calculations at different expansion ratios and chamber pressures. Another implication of Figure 4.6 is that the performance is not as critical on the H_2 vibrational temperature as originally believed. A stagnation temperature of 2300°K for the H_2-HCl mixture gives a frozen vibrational temperature of 2100°K for the H_2. This relatively low H_2 vibrational temperature pumps the HCl to a vibrational temperature of 6500°K.

The harmonic oscillator program was then modified to include the H-atom recombination kinetics to see if the equilibrium H-atom throat value could be obtained using a quick freeze nozzle. The original contour had a subsonic approach section of .1 cm long. This resulted in essentially no H-atom recombination in the nozzle. The subsonic approach section was increased to 1.6 cm and 3.2 cm as shown in Figure 4.7. The resulting H-atom concentration versus x is shown in Figure 4.8. The theoretical results indicate that the equilibrium throat value of H-atom concentration is not achieved. A similar calculation was performed for chamber conditions of 80 atmospheres and 2800°K. The H-atom concentration is shown in Figure 4.9. Again, the H-atoms do not reach the throat equilibrium value although at the large subsonic lengths the differences are not large.
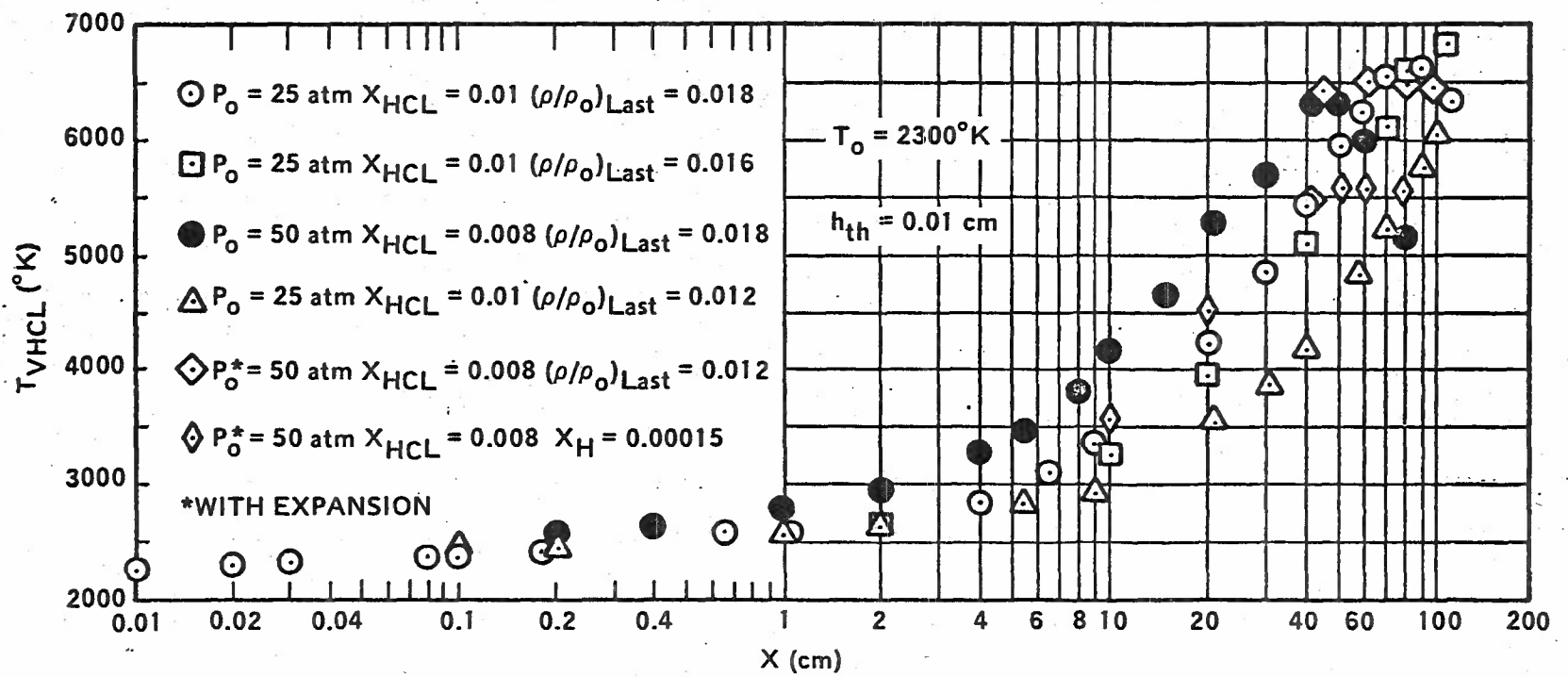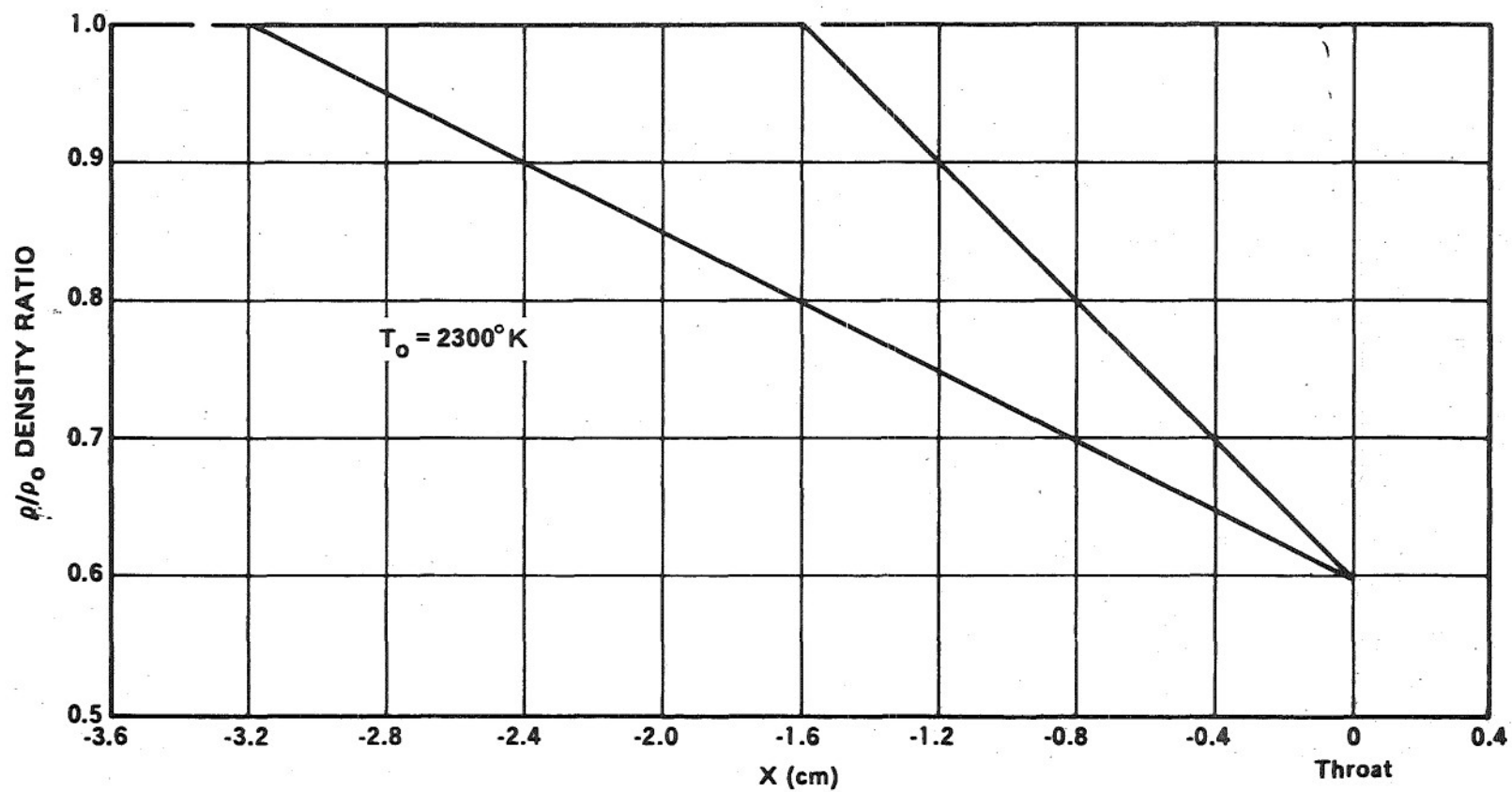
Figure 4.6 HCL Vibrational Temperature.

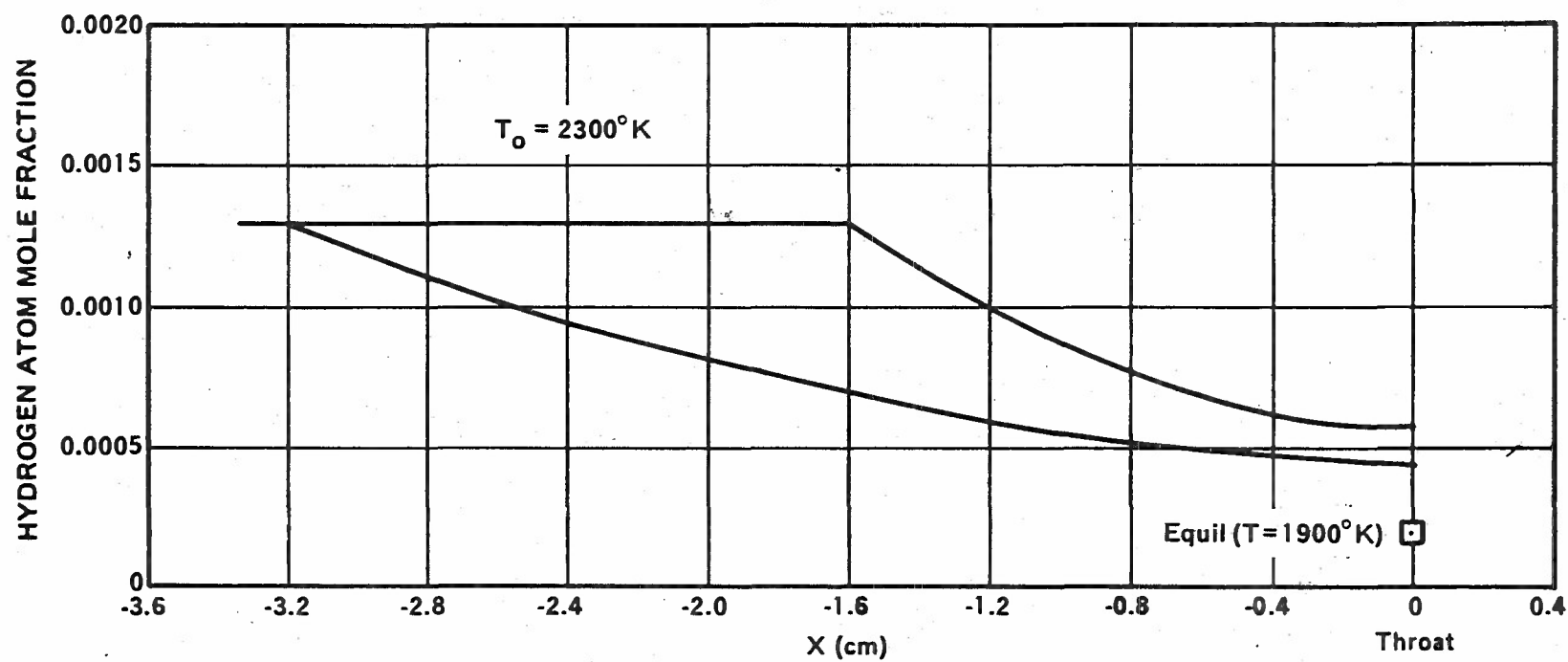FIGURE 4.7. NOZZLE SUBSONIC SECTION DENSITY DISTRIBUTION

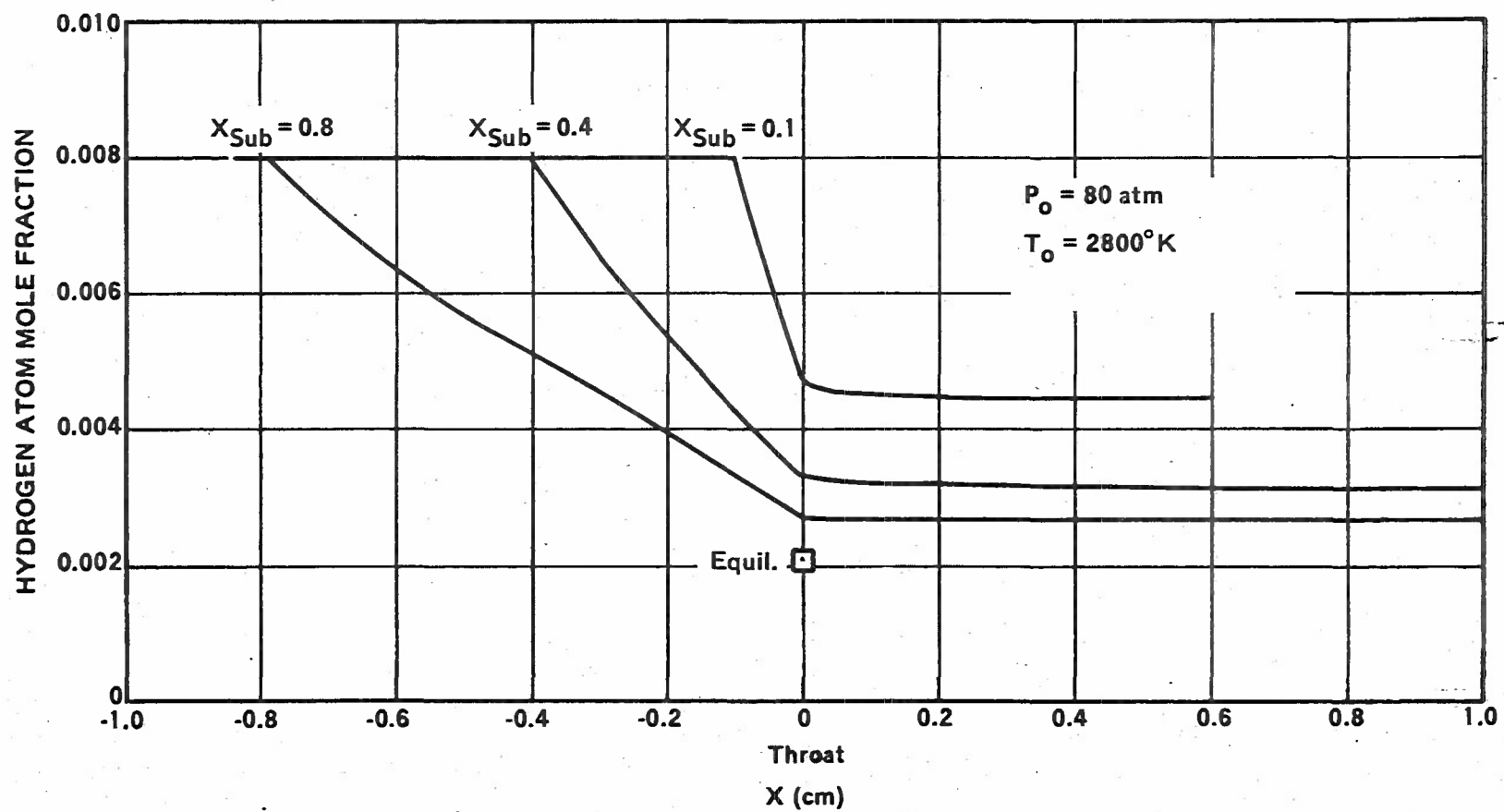FIGURE 4.8. H-ATOM CONCENTRATION IN SUBSONIC NOZZLE REGION

FIGURE 4.9.   H-ATOM CONCENTRATION

4.1   Method of Characteristics Analysis

The harmonic oscillator or anharmonic oscillator analysis is not capable of generating a smooth nozzle contour that will produce a nozzle exit flow that is uniform and shock free. For this reason, a method of characteristics computer program that takes into account the nonequilibrium nature of the flow was developed. This program is a combination of a method of characteristics program and the harmonic oscillator analysis program. The modifications required to the method of characteristics program were to use the frozen sound speed defined as

$$a_f^2 = \frac{p}{\rho} \left(\frac{C_p}{C_p - R} \right)$$

where p = pressure   R = gas constant

ρ = density

where C_p are comprised of only the rotational and translational contributions to the specific heat. Also, the velocity u and temperature T that appear in the compatibility equations are determined from the solution of the energy and momentum equations which are:

$$u \frac{du}{dx} = - \frac{dh}{dx}$$

$$\frac{u}{R} \frac{dh}{dx} = \left(- \dot{E}_v + \frac{C_p}{R} Tu \frac{d\ln\rho}{dx} \right) \Bigg/ \left(\frac{C_p}{R} - 1 \right)$$

$$uC_p \frac{dT}{dx} = u \frac{dh}{dx} - R \dot{E}_v$$

The terms involving $\dot{E}_v$ represent the effect of vibrational nonequilibrium and are the sum of the compounds from each specie. The quantity h is the static enthalpy as

$$h = \Sigma X_i E_{vi} + C_p T$$

where X_i is the mole fraction of specie i.

The compatability equations for the characteristics solution also contains a heat release term which accounts for nonisentropic vibrational energy changes. The compatibility equations are

$$A \, dp \pm d\theta + B \begin{Bmatrix} d\eta \\ d\xi \end{Bmatrix} + \frac{a_f}{u^2 C_p T} \, \Sigma \, X_i \, \dot{\omega}_i \begin{Bmatrix} d\eta \\ d\xi \end{Bmatrix}$$

where

$$A = \left(\frac{u^2}{a_f^2} - 1 \right)^{1/2} \Big/ \rho u^2$$

$$B = a_f \frac{\sin \theta}{uy}$$

$$\dot{\omega}_i = \frac{\partial E_{vi}}{\partial t}$$

The increments $d\eta$ and $d\xi$ are shown in Figure 4.10 and are the distances along the uprunning and downrunning characteristics, respectively.

The computer program has been used to determine a preliminary contour for the Mod VIII nozzle contour. The area distribution from the harmonic oscillator program was used to determine an initial estimate for the contour. This was then used to determine the nozzle slope as a function of x. This initial flow angle distribution is shown in Figure 4.11. This initial contour produced the wave diagram in Figure 4.12 and caused the program to terminate at about x = .125 cm on the centerline. This was due to the formation of a shock. The contour was then subsequently modified to that designated as A in Figure 4.11. The wave diagram for this case is shown in Figure 4.13. As can be seen from the figure, a weaker shock is now forming due to too rapid turning of the nozzle wall back to zero. The shock is weaker than the initial contour but is still present. Further reduction in the nozzle wall angle would eventually result in completely eliminating the shock.
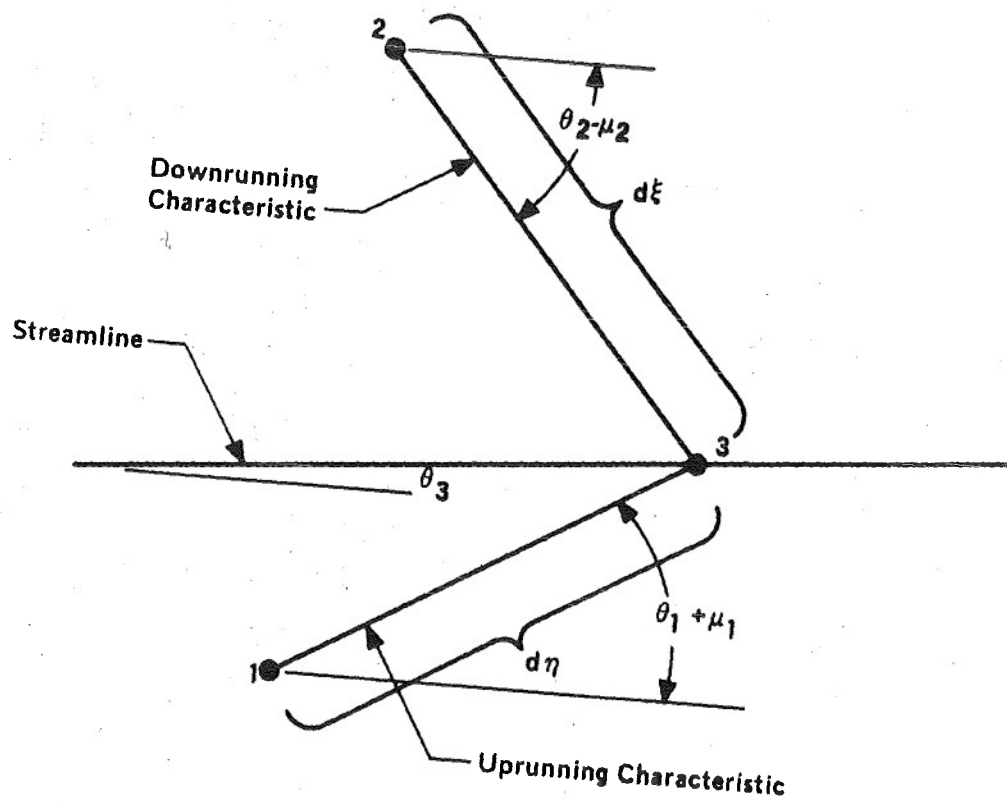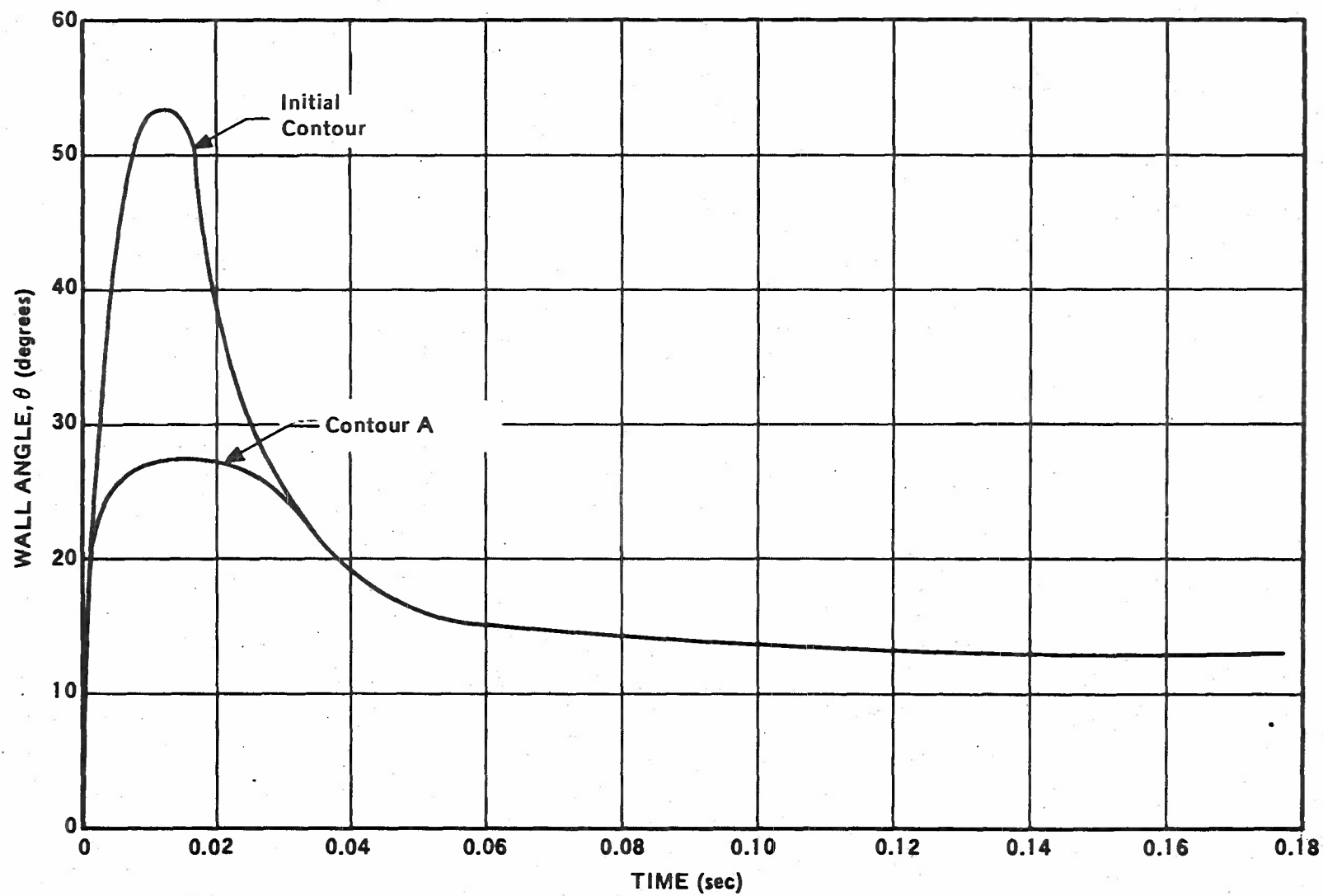
Figure 4.10. Characteristic Mesh Details.

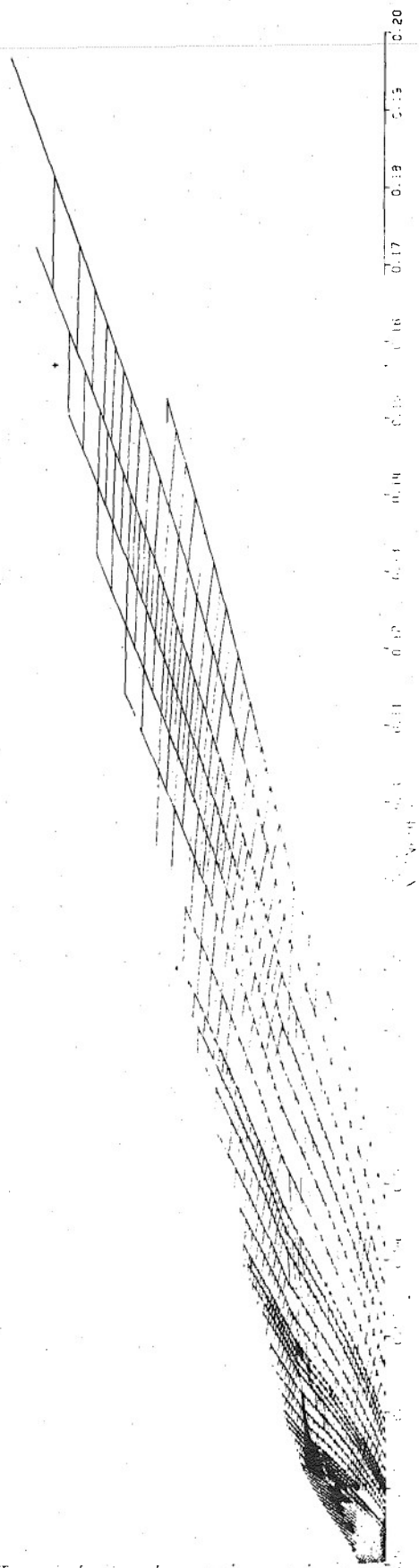Figure 4.11. Mod VIII Nozzle Contour, θ Versus

Figure 4.12. Nozzle Contour Test Case.
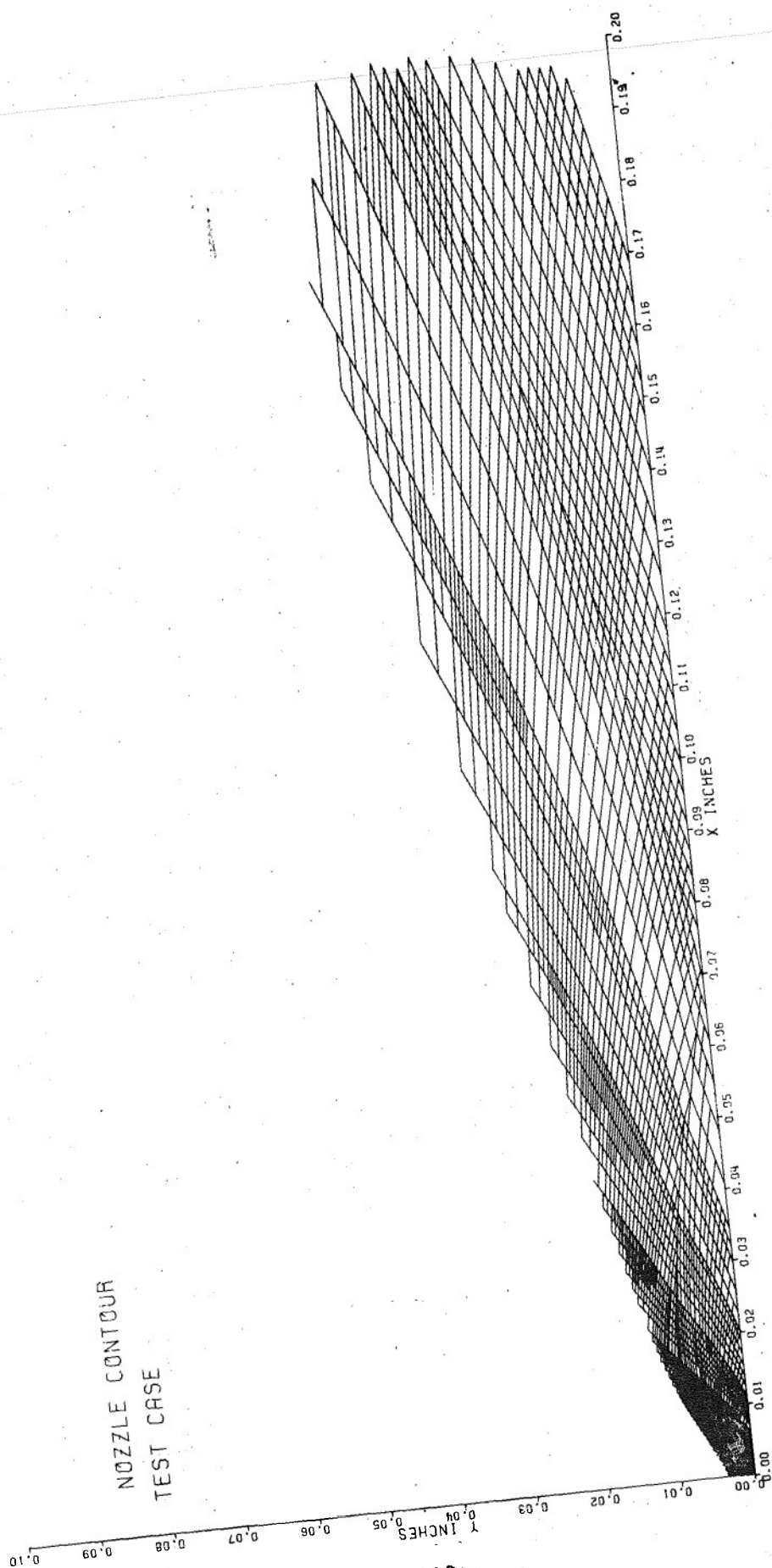
NOZZLE CONTOUR
TEST CASE

Figure 4.13. Nozzle Contour Test Case.

The inviscid nozzle contour as determined from the method of characteristics analysis has to be corrected for viscous effects due to boundary layer growth. To accomplish this, a boundary layer integral technique was used. Due to the extremely large flow gradients in the throat region of a quick freeze gas dynamic laser nozzle, an integral approach requires considerably less computer time than a finite difference technique. The integral technique employs the momentum integral equation which is

$$\frac{d\theta}{dx} + \frac{\theta}{\rho_e U_e^2} \frac{d}{dx}(\rho_e U_e^2) + \frac{\delta^*}{U_e} \frac{dU_e}{dx}$$

$$= \frac{\tau_\omega}{\rho_e U_e^2}$$

where U_e = boundary layer edge velocity

δ^* = displacement thickness

θ = momentum thickness

δ = boundary layer thickness

ρ_e = boundary layer edge density

τ_ω = wall shear stress

There are three unknowns in this equation, θ, δ^* and τ_ω. The quantities δ^* and θ are defined as

$$\delta^* = \delta \int_0^1 \left(1 - \frac{\rho}{\rho_e} \frac{u}{u_e}\right) d\eta$$

$$\theta = \delta \int_0^1 \frac{\rho u}{\rho_e u_e} \left(1 - \frac{u}{u_e}\right) d\eta$$

The evaluation of δ^* and θ require specifying the velocity profile and the density profile. The velocity profile selected is a power law profile of the form

$$\frac{u}{u_e} = (\eta)^{1/N}$$

The quantity N is determined using the empirical data of Reference 40. A curve fit of N is given in Figure 4.14. As can be seen in the figure, the value of θ and subsequently $R_{e\theta}$ determines the value of N which in turn determines the velocity profile. This approach is simpler than resorting to the use of an additional equation to determine N and since the real test of the method must rely on experimental data, for the present this technique is probably sufficient.

The density profile and shear stress were determined using the results of Reference 41. The work of Reference 41 reviewed the literature on compressible turbulent boundary layers. One of the results of Reference 41 was to develop an expression for the skin friction coefficient C_f from which the wall shear stress τ_ω can be determined. The skin friction relation developed has the form

$$C_f = \frac{F_{rd} R_{e\theta}}{F_c}$$

where

$$F_{rd} = \left(\frac{T_w}{T_\infty}\right)^{-.702} \left(\frac{T_{oe}}{T_w}\right)^{.772}$$

$$F_c = \left[\int_0^1 \left(\frac{\rho}{\rho_\infty}\right)^{1/2} d(u/u_e)\right]^{-2}$$

The density distribution used in the above relation is

$$\frac{\rho}{\rho_\infty} = \left[\frac{T_W}{T_\infty} + \left(1 + \frac{1}{2} r (\gamma - 1) M_\infty^2 - \frac{T_W}{T_\infty}\right) \frac{u}{u_c} - \frac{r}{2} (\gamma - 1) M_\infty^2 \left(\frac{u}{u_c}\right)^2\right]^{-1}$$

where r is the recovery factor and has a value of about .89. A plot of $F_c C_f$ versus $F_{r\theta} R_{e\theta}$ taken from reference 41 shown in Figure 4.15. These values are also tabulated in the reference and are given in Table 4.2. The two sets of data, however, do not agree. In order to eliminate this problem a test case for
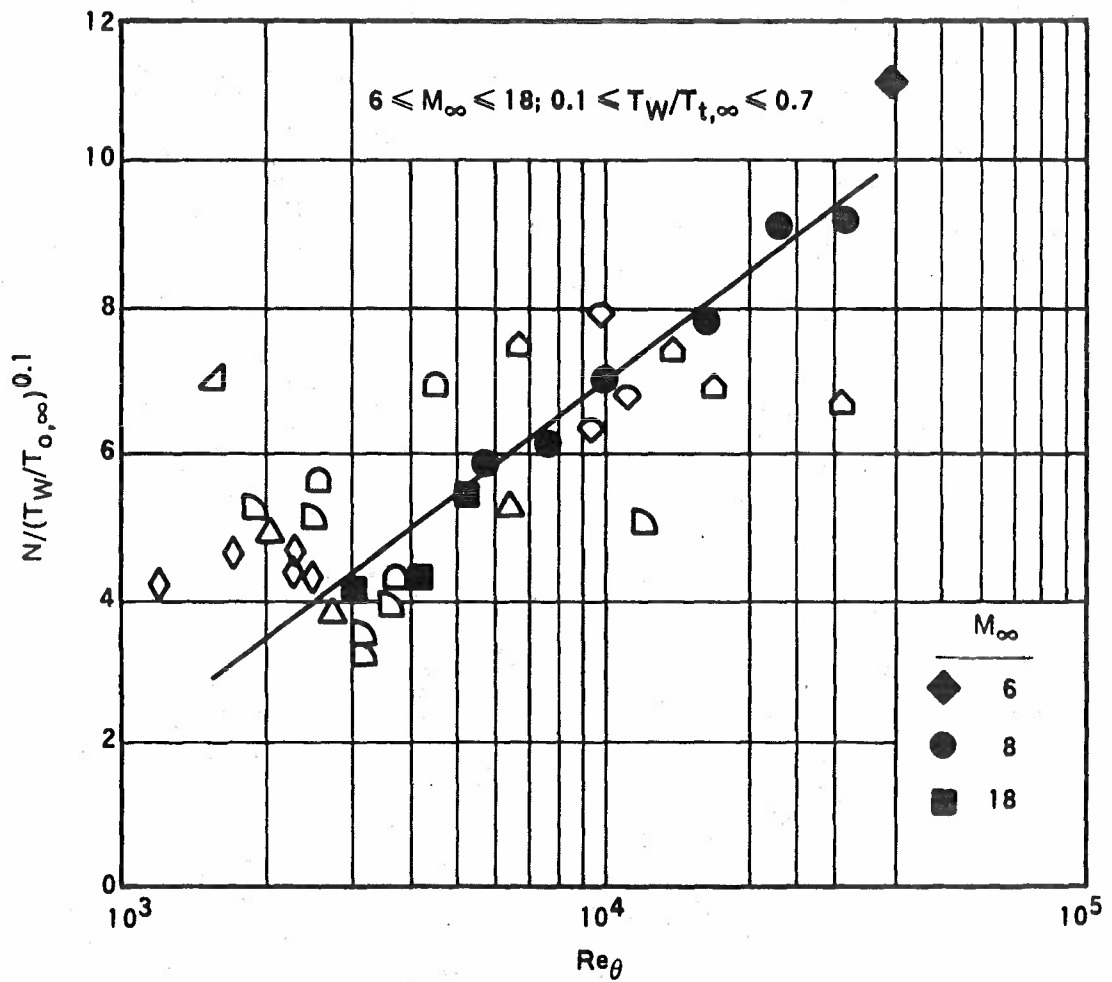
- 110 -

Figure 4.14   Variation of N with Re_θ for Axisymmetric Air and Nitrogen Nozzie Data.
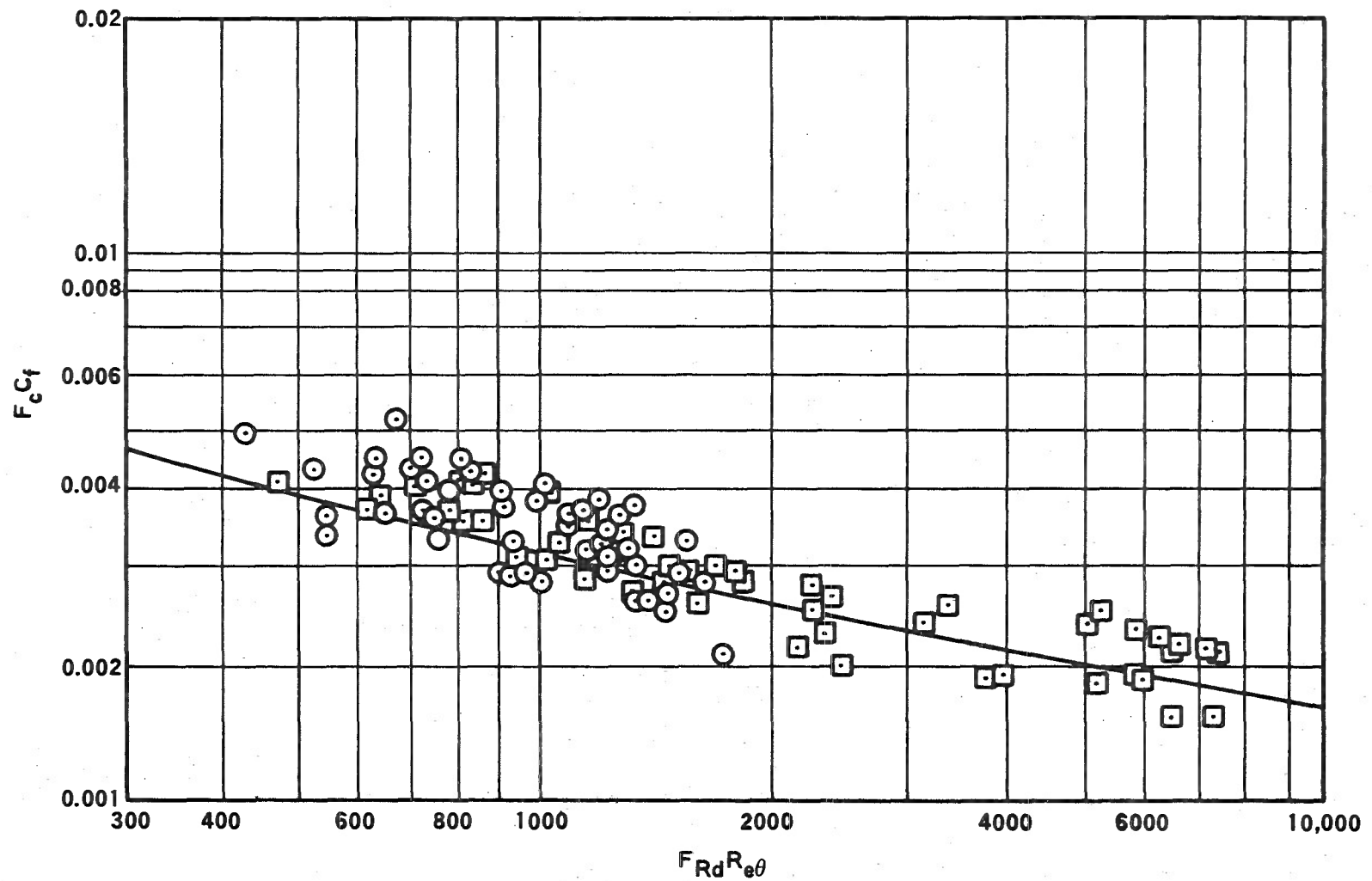
Figure 4.15 Comparison Between Theoretical and Experimental $F_c C_f$ Versus $F_{Rd} R_{e\theta}$.
$\boxdot$, Experiments, Adiabatic; O, Experiments with Heat Transfer; –, Theory.

TABLE 4.2

BOUNDARY LAYER CHARACTERISTICS *

$F_c c_f$	$F_{R_d} R_{e\theta}$	$F_c c_f$	$F_{R_d} R_{e\theta}$
0·0010	$2{\cdot}878 \times 10^7$	0·0060	233·0
0·0015	$3{\cdot}955 \times 10^5$	0·0065	177·6
0·0020	$5{\cdot}425 \times 10^4$	0·0070	140·4
0·0025	$1{\cdot}386 \times 10^4$	0·0075	114·4
0·0030	5030	0·0080	95·62
0·0035	2283	0·0085	92·49
0·0040	1208	0·0090	70·91
0·0045	716·0	0·0095	62·55
0·0050	462·3	0·0100	55·87
0·0055	319·4	0·0105	50·46

*Reference 41 - "The Drag of a Compressible Turbulent Boundary
Layer on a Smooth Flat Plat with and without Heat Transfer,"
D.B. Spalding and S.W. Chi, Journal of Fluid Mechanics, Vol. 18,
Part I, January 1964.

air was run that employed the analysis of reference 42. The results of this case are shown in Figure 4.16. The curve fit for C_f employed in the present technique that gave the best agreement with the method of reference 42 was

$$C_f = .0462 \left(F_{rd} R_{e\theta} \right)^{-.283826} / F_c.$$

The technique was then used to determine the boundary layer properties for the Mod VIII nozzle contour. The results of this calculation are shown in Figure 4.17. The results indicate that the boundary layer displacement thickness is relatively small and represents only a small percentage of the nozzle exit flow area. It must be remembered that these results are valid only within the limits of the analytical model employed but represent a good first estimate of the viscous effects.
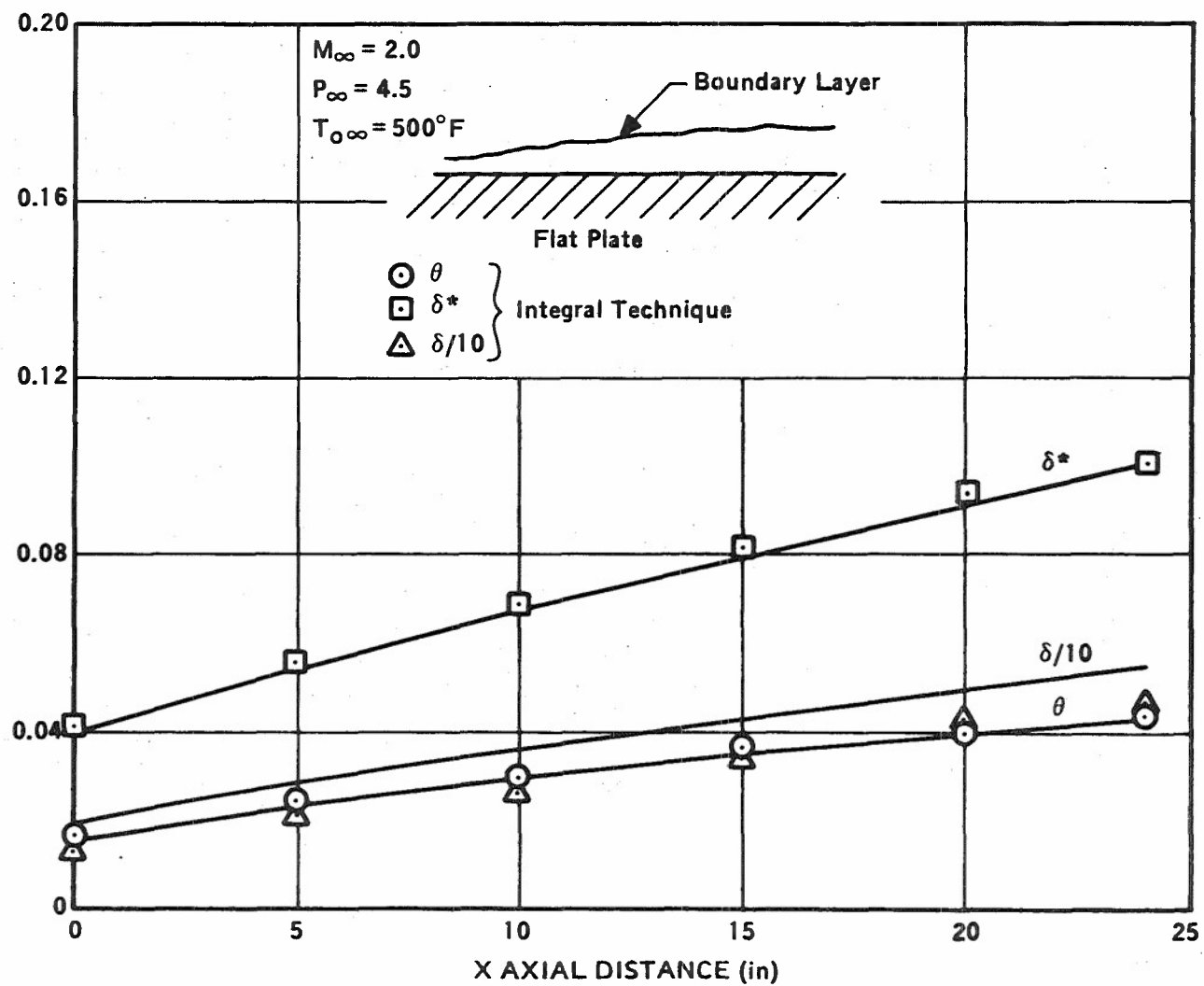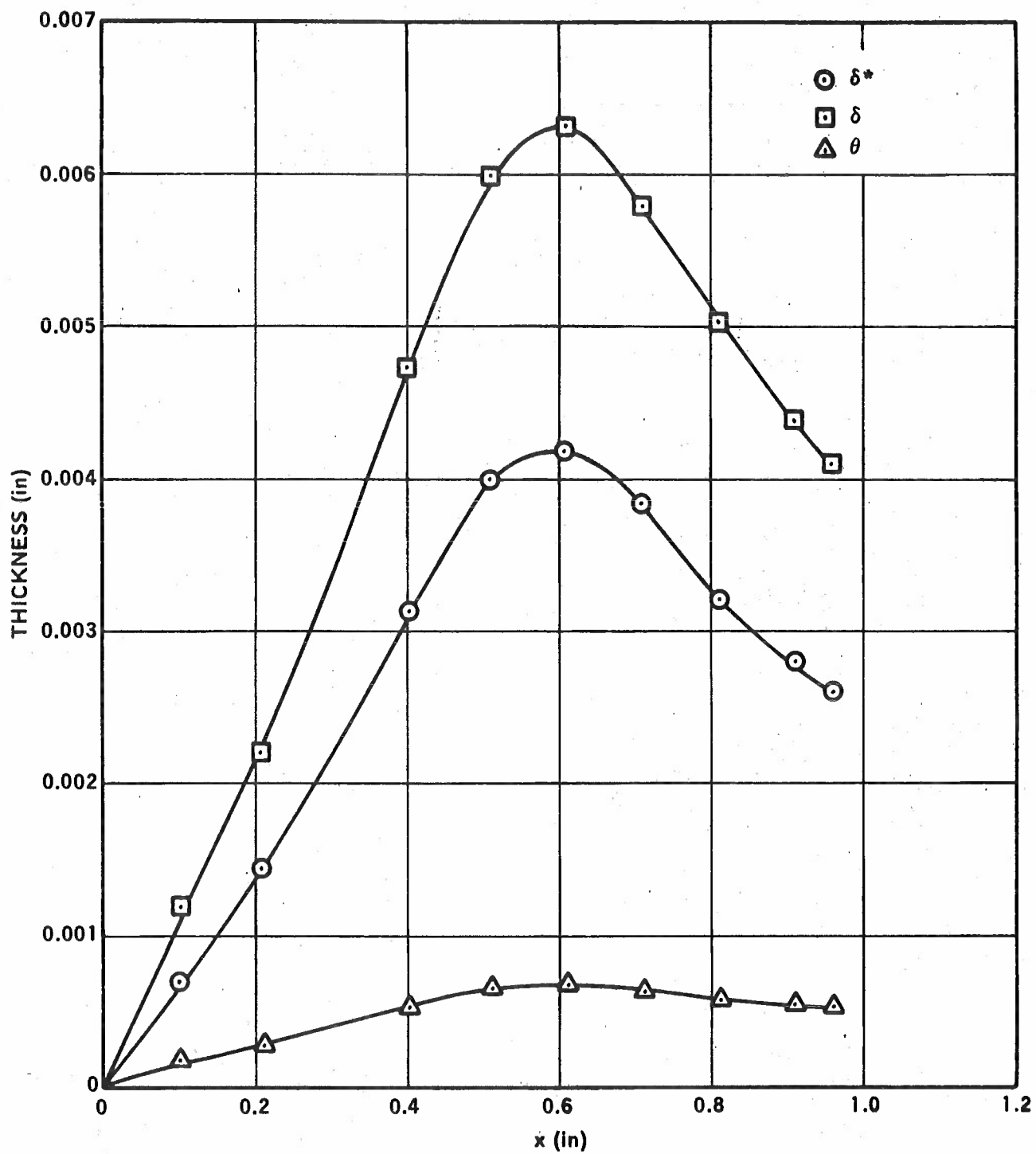
Figure 4.16 Test Problem Flow Configuration.

Figure 4.17 Nozzle Boundary Layer Properties.

4.3   Propellant Impurity Effects

During the solid propellant gas generator development, it was anti-cipated that various species other than H_2/HCl and their atoms might also be produced in small concentrations. A list of potential contaminant species is given in Table 4.3.   The effect of these impurity species on predicted laser performance is important, since it could well determine the technical direction of any further propellant development work undertaken.

Most of the impurity species listed in Table 4.3 are metallic halides, oxides, or hydroxides with relatively high boiling points. Because they are not easy to produce in the gas phase, there is no experimental data on their efficiency of vibrational relaxation on HCl or H_2. The fundamental vibrational frequencies of these refractory species are quite small compared to those for H_2 and HCl.   Therefore, it is anticipated that these impurities will not act as V → V deactivators. On the other hand, the efficiency of a V → T deactivation might reasonably be expected to vary between a probability per collision, P, of 10^{-1} to 10^{-5}. For illustration, we will assume a value of 10^{-3} which is also similar to the probability for the HCl/HCl V→T process at T = 300°K. Therefore, for impurity specie concentrations <<[HCl], the effect of the contaminant should be insignificant. To allow for the possibility of a larger probability per collision, a more conservative estimate of [impurity] $\lesssim 0.1$ mole percent is suggested. This appears to be generally within the capa-bility of the current propellant technology.

Of the species listed in Table 4.3 only two possess fundamental fre-quencies close to those of HCl, e.g., H_2O, and N_2.   Some data do exist on the vibrational coupling of N_2 to HCl, so it was decided to do a more quantitative estimate of the effect of these species on laser performance. .

H_2O is a special case. It is known that H_2O deactivates HCl very rapidly[35], although no temperature dependence is available. If the large cross-section for deactivation persists to elevated temperature, the effect of H_2O on laser performance would be very similar to that of H-atoms. For this reason, the concentration of H_2O was kept to a low value in the propellant formulations selected.

TABLE 4.3

POTENTIAL GAS CONTAMINANTS

SPECIES	VIBRATIONAL FREQUENCIES[33,34] (cm^{-1})
BF	1410
BF_2	1120, 470, 1450
BF_3	881, 670, 1463, 480
ZrCl	437
$ZrCl_2$	346, 92, 461
$ZrCl_3$	490, 185, 333, 131
$ZrCl_4$	376, 99, 418, 110
AlCl	480
$AlCl_2$	430, 210, 540
$AlCl_3$	371, 146, 185, 610
AlOCl	450, 350, 900
Al_2O	715, 238, 994
AlOH	1000, 1300, 3600
H_2O	3652, 1595, 3756
N_2	2331

Vibrational rate constants have been assembled for $N_2/H_2/HCl$ molecular systems from the available data[7,36,38] and are listed in Table 4.4. Figure 4.18 shows the result of a calculation of available energy as a function of N_2 mole fraction for the assumed base line condition. The results of this calculation indicate that 2-3% of N_2 is acceptable without appreciably affecting performance. A major part of the performance change is due to the increased effective mass of gas as N_2 is added. Some of the loss can be recovered through improved gas yields made possible by permitting N_2 formation. Thus, the gas generators selected are sufficient for good performance; however, a more detailed assessment of N_2 must await better kinetic data or shock tunnel gain experiments.

4.4   Power Extraction

The initial feasibility calculations were all based on the concept of "available energy," i.e., the amount of potentially abstractable energy existing in HCl at some selected position in the cavity. To provide a more realistic analytic capability, power extraction models based on the "gain equals loss" approximation were developed and became operational for both the H.O. and A.H.O. codes. These analyses for power extraction are based on the Rigrod approach[35] employing the concept that lasing can occur when the gain exceeds the single pass cavity loss. The photon amplification condition in the laser cavity can be expressed as:

$$e^{(2g_v^{v-1} \ell)} \geq [R(1 - L_c)]^{-1} \tag{32}$$

where g_v^{v-1} is the gain for vibrational transition $v \to v - 1$, ℓ is the cavity length between mirrors of "effective" reflectivity R (which includes all useless losses), and L_c is the cavity output coupling. Equation (32) can be rewritten as the lasing condition

$$g_v^{v-1} \geq -\frac{\ln[R(1 - L_c)]}{2\ell} \tag{33}$$

The gain is determined from the level populations which are in turn determined by the kinetic equations.

The effect of stimulated emission is incorporated into the differential equations for the level populations by adding to the kinetic terms the effects of lasing to and from the particular level; namely
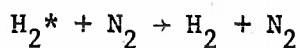
- 119 -

TABLE 4.4

VIBRATIONAL KINETICS FOR $N_2/H_2/HCl$ SYSTEMS

(Rate constants in units of $cm^3 - particles^{-1} sec^{-1}$)

$V \rightarrow T$ Process (26)

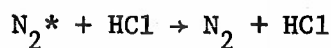$HCl^* + N_2 \rightarrow HCl + N_2$
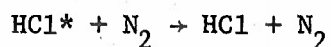
$\qquad k_f = 5.53 \times 10^{-14} \, T \exp(-109.62 \, T^{-1/3}) \, cm^3\text{-molecule}^{-1}\text{-sec}^{-1}$

$H_2^* + N_2 \rightarrow H_2 + N_2$ (27)

$\qquad k_f = 5.44 \times 10^{-10} \exp(-114.91 \, T^{-1/3})$

$N_2^* + HCl \rightarrow N_2 + HCl$ (28)

$\qquad$ (not known, but unimportant when $H_2 \quad HCl$)
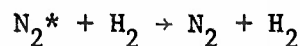
$N_2^* + H_2 \rightarrow N_2 + H_2$ (29)

$\qquad k_f = 1.78 \times 10^{-7} \exp(-172.69 \, T^{-1/3})$
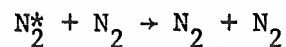
$N_2^* + N_2 \rightarrow N_2 + N_2$ (30)

$\qquad k_f = 8.53 \times 10^{-7} \exp(-273.10 \, T^{-1/3})$

$V \rightarrow V$ Process
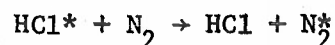
$HCl^* + N_2 \rightarrow HCl + N_2^*$ (31)

$\qquad k_f = 8.10 \times 10^{-17} \, T$

(The H_2/N_2 $V \rightarrow V$ process is considered as unimportant and thus neglected)

Figure 4.18. Effect of N_2 on Performance.

$$\frac{d\,n_v}{dt} = \frac{d\,n_v}{dt}\Bigg|_{\text{kinetic}} + g_{v+1}^v\,F_{v+1}^v - g_v^{v-1}\,F_v^{v-1} \tag{34}$$

F_v^{v-1} is the cavity flux determined from the imposition of Equation (33).
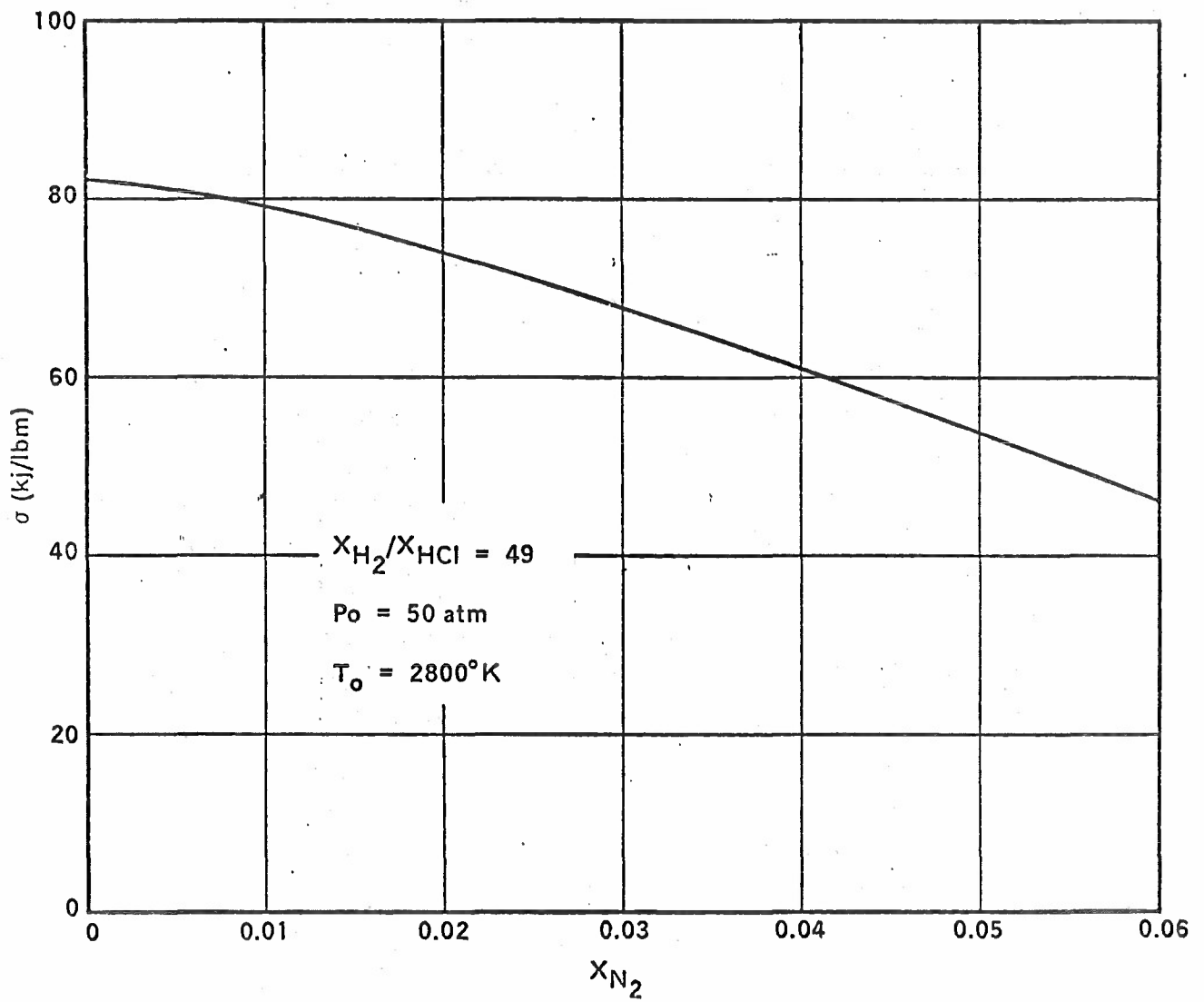
 This model assumes rotational equilibrium. For a given vibrational level, only the rotational line of largest gain is allowed to laser, but simultaneous lasing on different vibrational levels is allowed. In the GDL case, the total power extracted is calculated from the expression:

$$E = \sum_v \frac{1}{\rho^* u^*} \int h\nu_v^{v-1}\,F_v^{v-1}\,A/A^*\,\frac{L_c}{2\ell}\,dx \tag{35}$$

where ρ^* and u^* are the gas density and velocity at the throat, and $h\nu_v^{v-1}$ is the energy of the transition. The results of a calculation using this model are illustrated in Figures 4.19 - 4.20.

 Figure 4.19 shows the calculated small signal gain, g_o, determined for the given conditions from the A.H.O. kinetics model. The maximum gain occurring on vibrational levels v = 1 - 7 is shown as a function of distance downstream of the nozzle throat. Assuming an optical cavity condition of R = 0.98 and L_c = 0.2 a critical gain can be calculated from Equation (33) and is shown on Figure 4.19 as the dashed line. Lasing should occur for x $\geq$ 10 cm downstream of the throat.

 Figure 4.20 shows the same calculation as Figure 4.19 including power extraction at distances greater than 15 cm downstream. The effect of lasing is seen to surpress the gain to values around the critical value. Only a few gain histories are plotted on Figure 4.20 for clarity. The observed oscillatory behavior is due to rotational line shifting on a particular vibrational level.

 On Figure 4.21 the cavity fluxes F_v^{v-1} for a number of vibration levels and the total flux, are given for the same conditions. From this result the total output power is calculated to be 54 kj/lb with most of this power radiated from the first three vibrational levels. As is seen in Figure 4.21 the cavity was allowed to extend arbitrarily to 300 cm downstream.
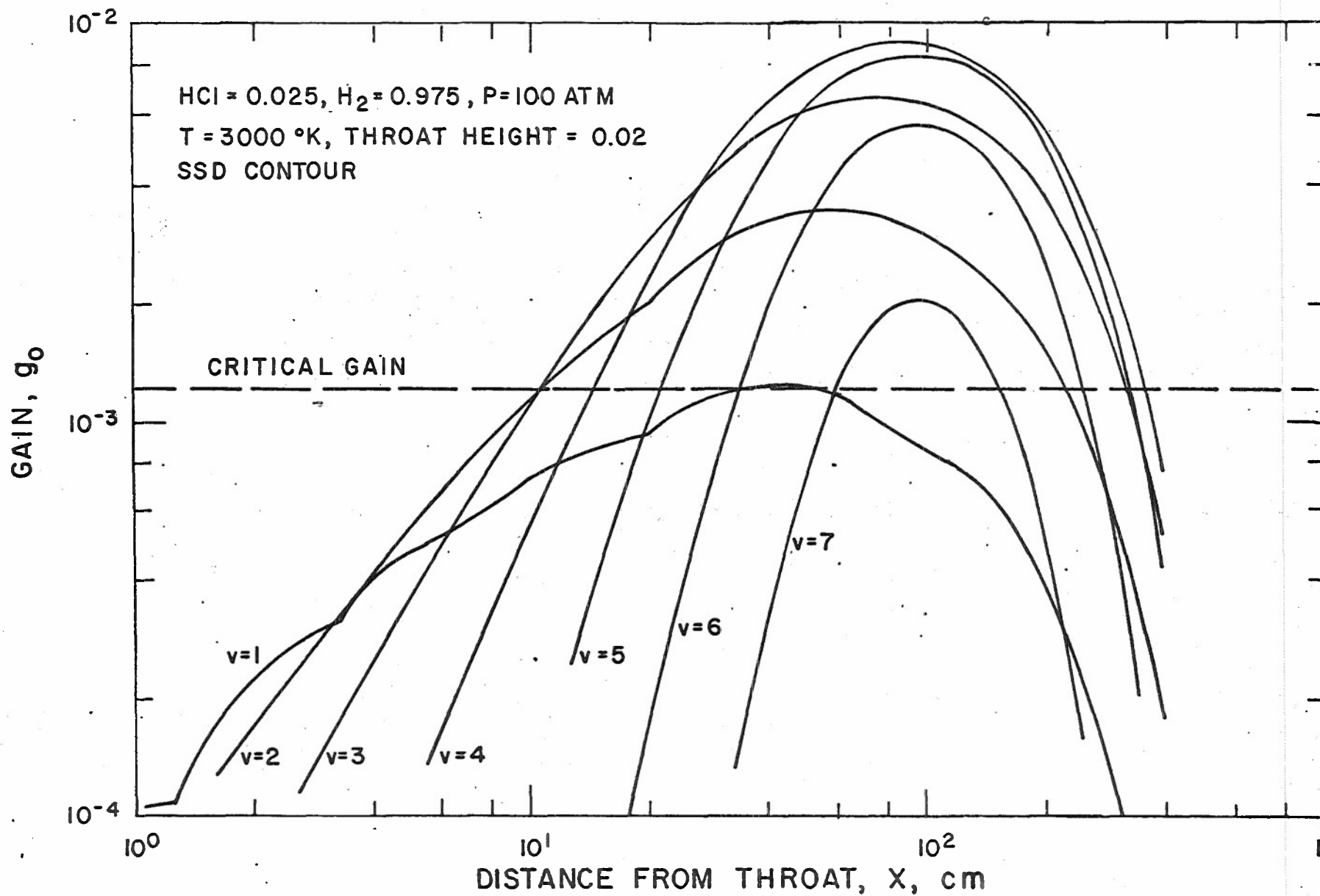
Figure 4.19. Maximum small signal gain for the v=1 to 7 vibrational levels of HCl. Critical gain is calculated for ℓ=100 cm, R=0.98, and L=0.2.
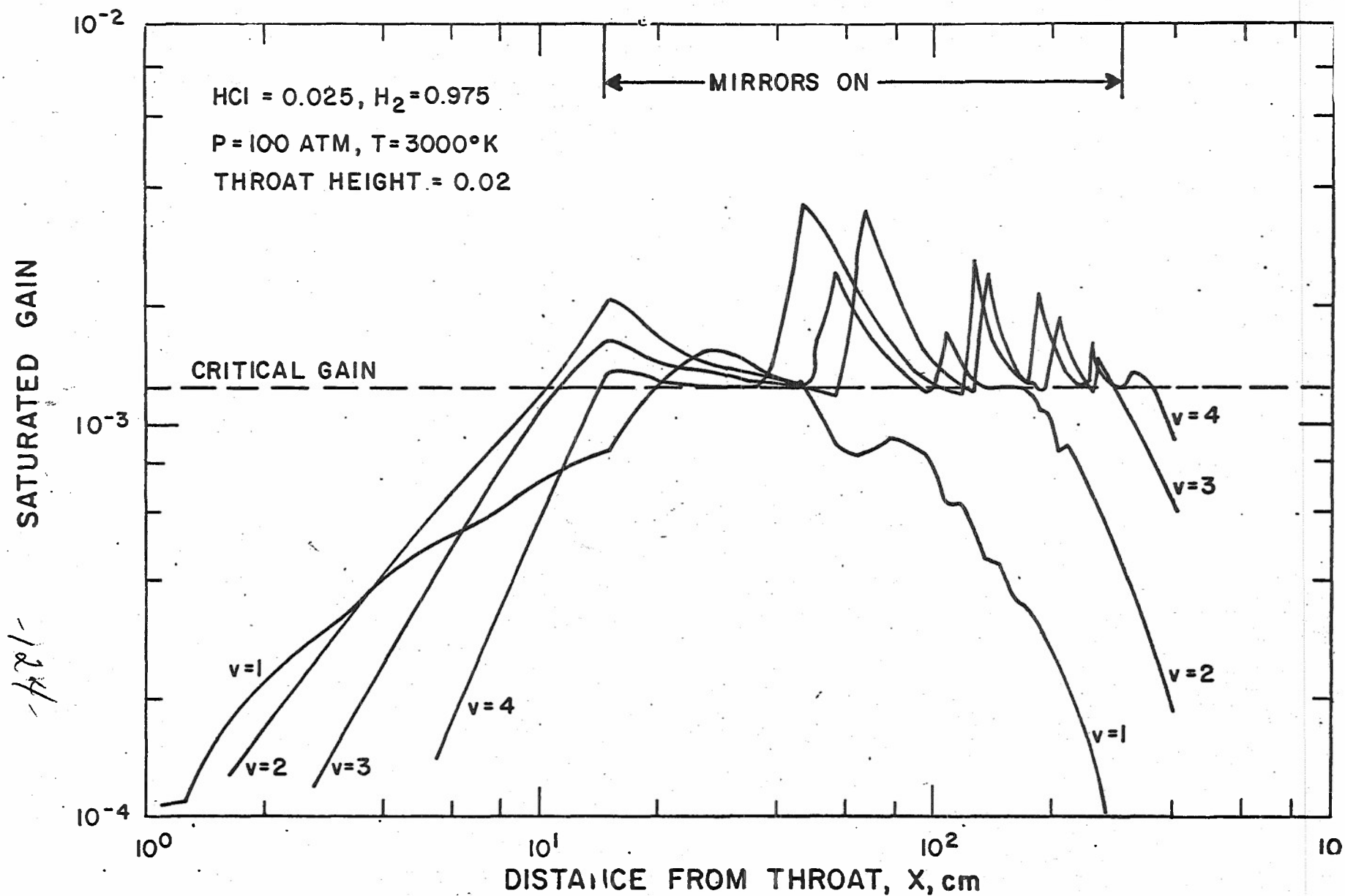
Figure 4.20. Saturated gain for v=1 to 4 vibrational levels of HCl.
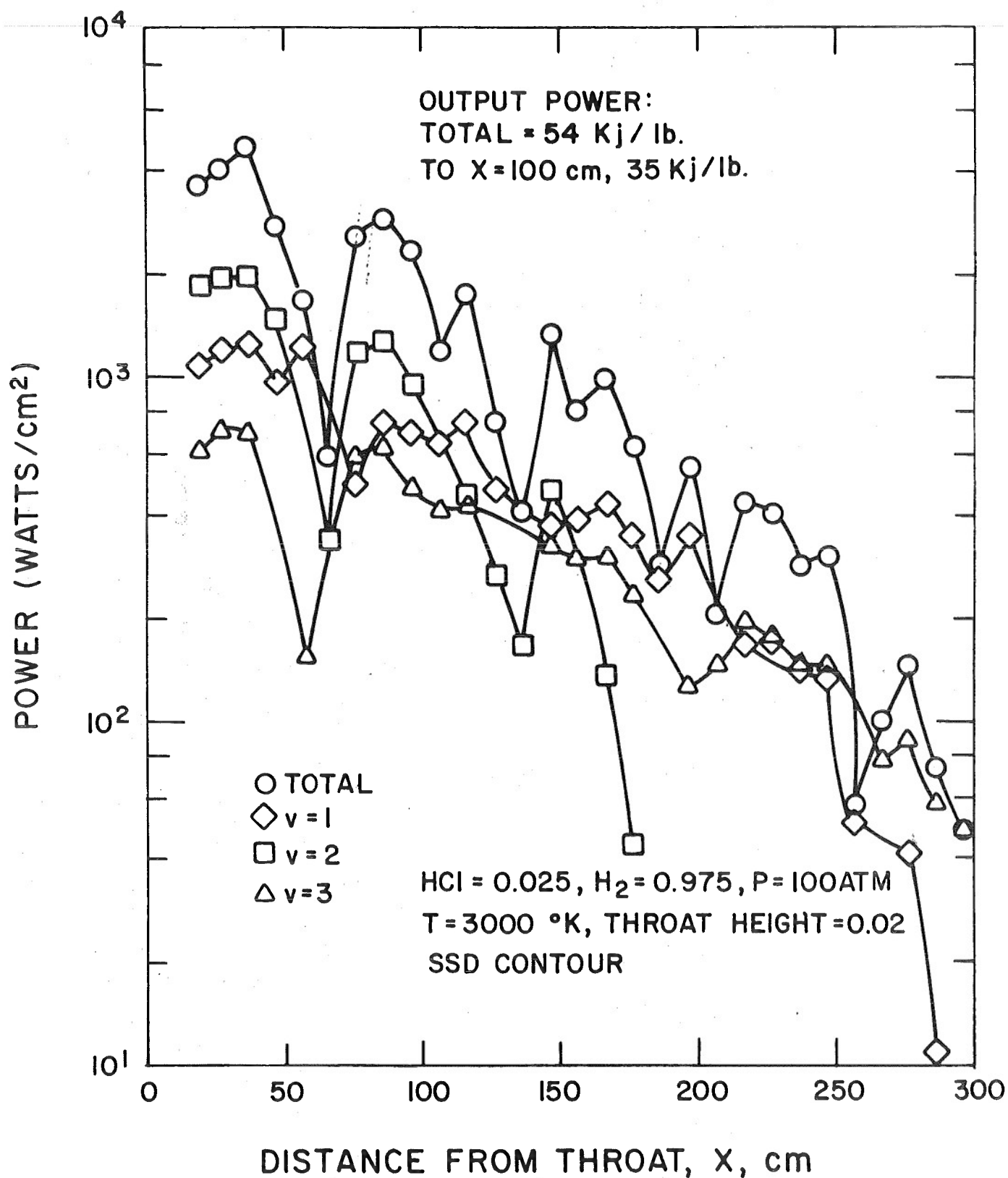Cavity conditions: ℓ=100 cm, R=0.98, and L=0.2.

Figure 4.21. Calculated intracavity flux for $v = 1$ to 3 vibrational transition of HCl. Also shown is the total flux, i. e., the sum of all levels, including those not shown.

However, the bulk of the energy is extracted early in the flow. For example, at X = 100 cm the output power is already 35 kj/lb. It is emphasized that the calculation presented in the figures is only illustrative, and no attempt has yet been made to optimize these results.

This power extraction routine can also be used with the H.O. model. In this situation, there is only a single vibrational level and the calculation is correspondingly simpler. The calculated output power in the H.O. approximation for the same assumed conditions as were shown previously for the A.H.O. case is given in Figure 4.22. A comparison of Figure 4.22 with the A.H.O. result indicates that the H.O. calculation yields about twice the extracted power as the A.H.O. result. This illustrates one severe limitation of this simple H.O. model of a vibration transfer laser.

4.5   Advanced H$_2$-HCl Gas Dynamic Laser System Characteristics

The end objective of the work performed is to develop a high energy laser device. The work performed during this phase is now sufficient to determine the weight and volume characteristics of a high energy laser system. A typical HEL device size was selected. The run time for the device consists of 20-three second bursts for a total run time of 60 seconds. The weight and volume of the laser system depends on the propellant weight yield and the specific power. The specific power used to estimate the system size is 100 kj/lb. This value represents an upper limit which depends on the effect of H-atoms on specific power. The H-atom problem will be addressed in much greater detail in the next year.

The laser device has been divided into three basic components which are: (1) the combustor; (2) the nozzle bank; and (3) the cavity and diffuser. A sketch of the device is shown in Figure 4.23. For the purpose of weight and volume estimates, the combustor is assumed to be comprised of 1" thick steel, the nozzle bank is assumed to be solid steel and the cavity and diffuser are assumed to consist of a 3" thermal skin. The thermal skin is comprised of a .25 inch thick steel plate outer shell and a .25 inch thick steel plate inner shell as shown in the inset of Figure 4.23.
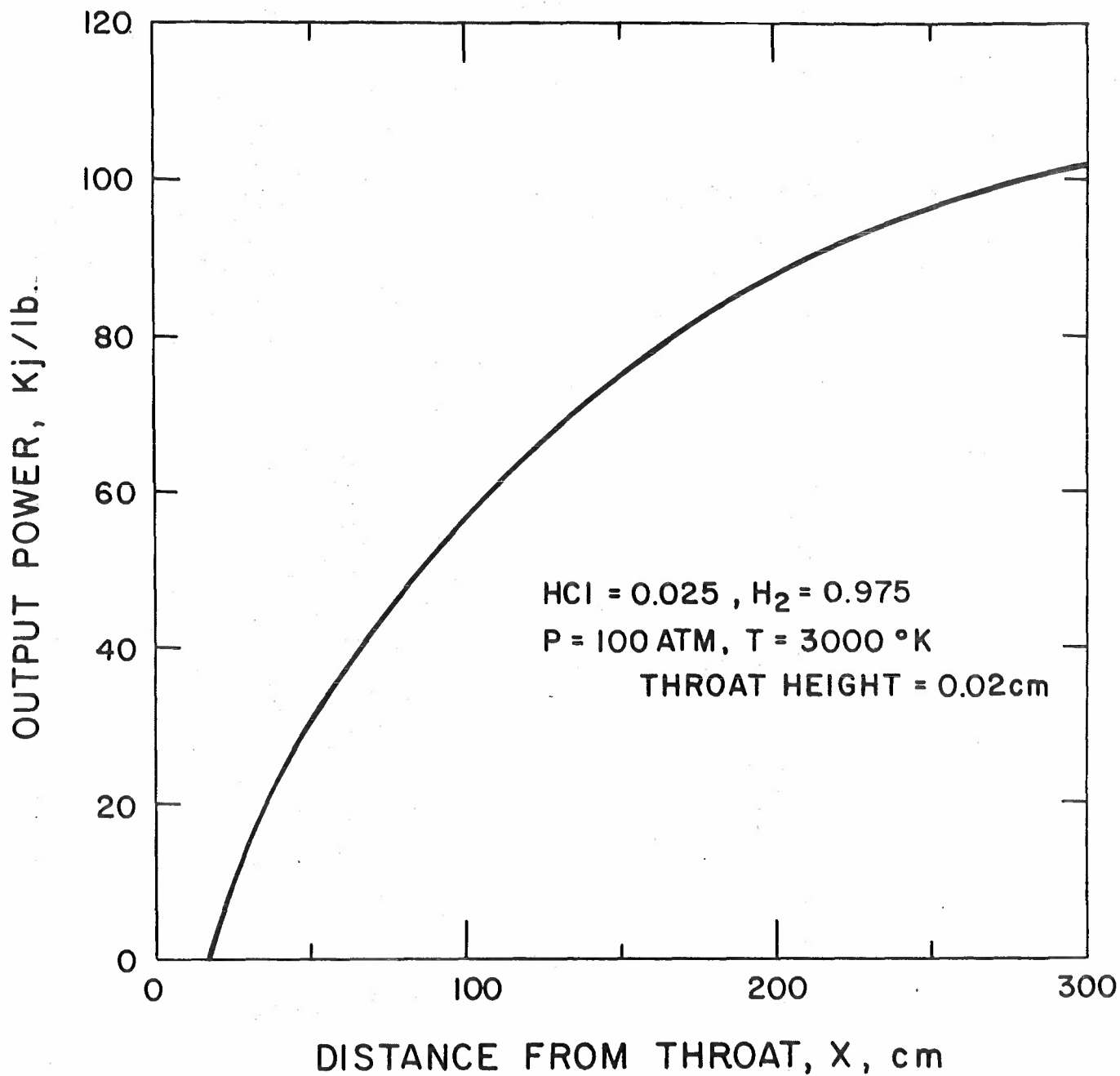
Figure 4.22. Calculated output power for H.O.
calculation. Cavity conditions
$\ell = 100$ cm, R = 0.98 and $L_c = 0.2$
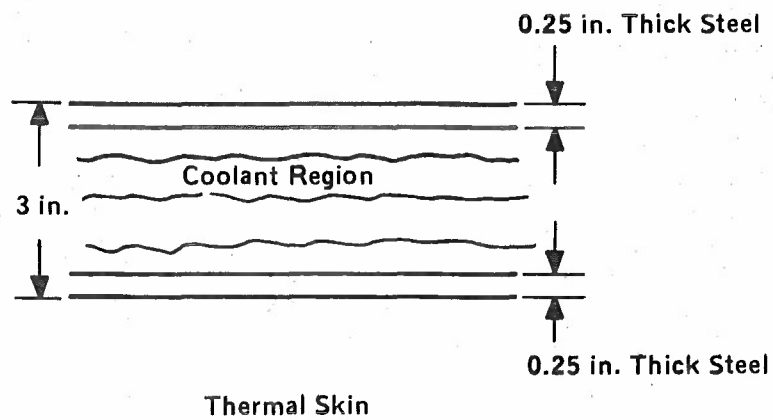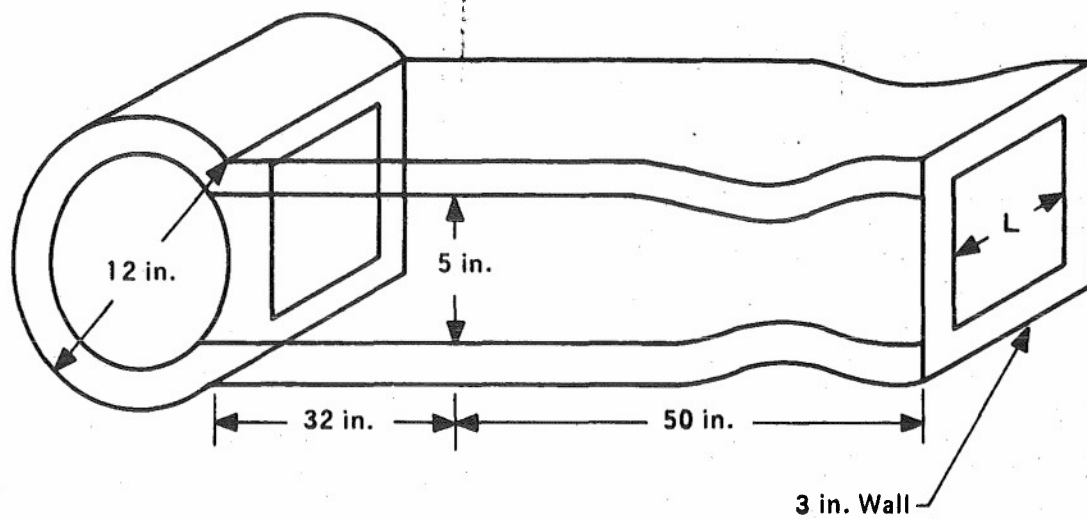
Figure 4.23. Laser Device

The weight and volume of the components is shown in Table 4.5 for each of the three candidate propellants. The overall envelope of the device is obtained using a packing factor of 2. The weight and volume of the individual gas generators are shown in Table 4.6. The gas generator weight and volume estimates include a filter system for propellant candidates 2 and 3. A more detailed breakdown of the gas generators is shown in Table 4.7.

The overall system weights and volumes are shown in Table 4.8. Also shown in Table 4.8 are the specific weight power of the laser devices, the specific volumetric power and the specific nozzle exit area power. The best device performance is obtained from the HDB propellant system, whereas the other two systems have about the same system weight and volume. Depending on whether the application of the laser is weight or volume limited either the device specific weight or volume parameter should be selected as the basis for comparison to other laser systems.

TABLE 4.5

WEIGHT AND VOLUME OF COMPONENTS

ITEM	PROP. 1 and 3 (L=2 ft)		PROP. 2 (L=2.5 ft)	
	WEIGHT(lb)	VOLUME(ft^3)	WEIGHT(lb)	VOLUME(ft^3)
COMBUSTOR	330	1.6	420	2
NOZZLE	378	0.73	500	1
CAVITY AND DIFFUSER	836	12.0	1,040	16
TOTAL	1,544	14.33	1,960	19
PF = 2		28.66		38

TABLE 4.6

WEIGHT AND VOLUME OF GAS GENERATOR

PROPELLANT	WEIGHT (lb)	VOLUME (ft^3)
1	4,900 (245)	45 (2.24)
2	10,100 (506)	88 (4.4)
3	11,580 (579)	104 (5.2)

( ) DENOTES PER SHOT

TABLE 4.7

PROPELLANT SYSTEM COMPARISON OF CANDIDATES

Comp ID	Composition, Wt %	H_2/HCl Molar	(H_2+HCl) Yield Wt %	Vol %	T_f, °K	Derived Propellant System Characteristics Propellant Wt (lb)	Weight of Case	Total Wt (lb)	Motor Vol(ft^3)	Motor Dia (in)	Motor Length (in)
1	11.821% H_2WO_4 33.475% Zr 38.704% HDB 16% AP	33.3	10.8	95.9	2808	139	121	260	2.8	15	26
2	10.482% NH_4NO_3 47.132% ZrH_2 38.186% $Zr(OH)_4$ 4% AP	38.2	3.84	89.5	2799	391	234	625	5.5	15	51
3	40.879% 42.968% ZrH_2 13.153% $Zr(OH)_4$ 3% AP	32.6	2.59	98.0	2799	579	275	854	6.5	15	61

TABLE 4.8

WEIGHT AND VOLUME OF SYSTEM

PROPELLANT	WEIGHT(ft)	VOLUME(ft^3)	kj/lb	kj/ft^3	kj/in^2
1	6,444	73	0.062	5.47	4.7
2	12,060	126	0.033	3.17	3.2
3	13,124	132	0.030	3.03	4.7

5.0   CONCLUSIONS

The results of the Phase I study indicated that an advanced H_2-HCl gas dynamic laser was indeed feasible. The objective of the current phase, Phase II, was to experimentally verify the V-V and V-T kinetics for the important H_2-HCl processes and to develop solid propellant gas generators that could be used to generate the required gases at attractive weight yields. The results of the current phase have verified that the kinetics are capable with operation of a H_2-HCl laser. In addition, the gas generator development program has succeeded in producing the required gases at weight yields that make the system attractive for Army field application. The potential of even higher gas yields that would make the system even more attractive is also possible but requires additional propellant development. The fundamental remaining problem area is the effect of H-atoms on performance. This problem area is currently under investigation and represents the only remaining barrier that prevents the development of an advanced H_2-HCl gas dynamic laser. It is believed that this problem may have to be resolved by the use of an adequate H-atom scavenging technique.

REFERENCES

1. "Final Report for Phase I of the NRML Laser," ARC Report No. 47-5629, Contract No. DAAH01-74-C-0611, Atlantic Research Corporation, Alexandria, Virginia 22311, February 1975.

2. W. D. Breshears and P. F. Bird, J. Chem. Phys. **52**, 999 (1970).

3. C. T. Bowman and D. J. Seery, J. Chem. Phys. **50**, 1904 (1969).

4. B. M. Hopkins, H. L. Chen and R. Sharma, J. Chem. Phys. **59**, 5758 (1973).

5. P. F. Zittel and C. B. Moore, J. Chem. Phys. **59**, 6636 (1973).

6. B. M. Hopkins and H. L. Chen, J. Chem. Phys. **57**, 3161 (1972).

7. J. F. Bott and N. Cohen, J. Chem. Phys. **63**, 1518 (1975).

8. M. M. Audibert, C. Joffries and J. Ducuing, Chem. Phys. Lett. **25**, 158 (1974).

9. J. H. Kiefer and R. W. Lutz, J. Chem. Phys. **44**, 668 (1966).
9a. J. E. Dove and H. Tietelbaum, J. Chem., Chemical Physics (1974) to be supplied.

10. The authors are indebted to Captain Charles Holmes of the Air Force Weapons Laboratory, Kirtland Air Force Base, Albuquerque, N.M., for his help in the theoretical calculation.

11. J. C. Decius, J. Chem. Phys. **32**, 1262 (1960).

12. R. V. Steele, Jr. and C. B. Moore, J. Chem. Phys. **60**, 279 (1974).

13. D. J. Seery, J. Chem. Phys. **58**, 1796 (1973).

14. R. N. Schwartz, Z. I. Slawsky, and K. R. Herzfeld, J. Chem. Phys. **20**, 1591 (1952).

15. R. L. Taylor, M. Camac and R. M. Feinberg, "Measurements of Vibration-Vibration Coupling in Gas Mixtures," Proceedings of the Eleventh Symposium (International) on Combustion, 14 - 20 August 1966, The Combustion Institute, Pittsburg, Pennsylvania, 1967, pp. 49-65.

16. V. Sato, S. Tsuchiya and K. Kuratani, J. Chem. Phys. **50**, 1911, (1969) plus Erratum, J. Chem. Phys. **53**, 1304 (1970).

17. K. Hancock, private communication.

18. D. Arnoldi and J. Wolfrum, Chem. Phys. Lett. **24**, 234 (1974).

19. R. F. Heidner III and J. F. Bott, J. Chem. Phys, **63**, 1810 (1975).

20. R. D. H. Brown, G. P. Glass and I. W. M. Smith, results to be published.

21. R. L. Wilkens, J. Chem. Phys. **63**, 534 (1975).

22. M. A. A. Clyne and D. H. Stedman, Trans. Far. Soc. **62**, 2164 (1966).

135

APPENDIX A

Theoretical values of flame temperature and combustion product compositions are tabulated here for selected propellants as a function of propellant compositions. Values of flame temperature are for adiabatic combustion with chemical equilibrium at 750 psia (generally). Values for combustion product compositions are for throat conditions, assuming expansion of only the gaseous species that exist at chamber conditions. The expansion is assumed to be isentropic, with chemical equilibrium throughout. The calculations are computerized results, using JANAF thermochemical data.

It should be noted that $Al_2O_3(c)$ and $BN(c)$ appear as combustion products at throat conditions of all propellants containing Al (or AlH_3) and HDB, respectively. This phenomenon has been discussed in the text and is essentially the result of condensation reactions of gaseous species during expansion. The effect is not large, amounting to ~2% by weight of combustion products appearing as condensed at the throat.

In the tables, the gas composition is expressed in terms of mol/100 gm of propellant. Some of the tables show the column entitled "Σng" which refers to the total moles of gaseous combustion products at the throat. The molar ratio H_2/HCl is seen to be quotient of the entry in Column 7 (H_2) divided by that in Column 8 (HCl). The yield (H_2 + HCl) is seen to be the sum of the products

$$2.016 \ (Col. \ 7) + 36.461 \ (Col. \ 8)$$

for the expression for weight percent. The yield (H_2 + HCl) for volume percent is the molar content of (H_2 + HCl) in the combustion products, and is

$$(H_2 + HCl)/\Sigma ng.$$

For most of the tables, this quantity is derived.

138

APPENDIX A

INDEX OF TABLES (1)

Propellant System

Oxidizer	Fuel	Coolant	Chlorides	Table Number
NH_4NO_3	ZrH_2	$Zr(OH)_4$	NH_4Cl	A1
			NH_4ClO_4	A2
		$(CH_2)_n$	NH_4Cl	A3
			NH_4ClO_4	A4
		HTPB	NH_4ClO_4	A5
	Zr	HTPB	NH_4ClO_4	A6
		HDB	NH_4Cl	A7
			NH_4ClO_4	A8
		HDB/CH_2		A9
	Al	$Al(OH)_3$	NH_4Cl	A10
			NH_4ClO_4	A11
		$(CH_2)_n$	NH_4Cl	A12
			NH_4ClO_4	A13
		HTPB		A14
	AlH_3	$Al(OH)_3$	NH_4Cl	A15
		$Al(OH)_3/(CH_2)_n$		A15
$N_2H_5NO_3$	ZrH_2	$Zr(OH)_4$	NH_4Cl	A16
			N_2H_5Cl	A17
			NH_4ClO_4	A18
		$(CH_2)_n$	NH_4Cl	A19
			N_2H_5Cl	A20
			NH_4ClO_4	A21
		HDB	NH_4Cl	A22
	Zr		N_2H_5Cl	A23
			NH_4ClO_4	A24
		$HDB/Zr(OH)_4$	$ZrCl_4$	A25

139

Propellant System

Oxidizer	Fuel	Coolant	Chlorides	Table Number
$N_2H_5NO_3$	Al	$Al(OH)_3$	NH_4Cl	A26
			N_2H_5Cl	A27
			NH_4ClO_4	A28
		$(CH_2)_n$	NH_4Cl	A29
			N_2H_5Cl	A30
			NH_4ClO_4	A31
		HDB	NH_4Cl	A32
	AlH_3	$Al(OH)_3$	NH_4Cl	A33
		$(CH_2)_n$		A34
		$Al(OH)_3$	NH_4ClO_4	A35
		$Zr(OH)_4$	NH_4Cl	A36
			NH_4ClO_4	A36
NH_4ClO_4	Al	HDB		A37
	Zr			A38
	Al		$ZrCl_4$	A38
	Zr	$Zr(OH)_4/(CH_2)_n$		A39
		$ZrH_2/Zr(OH)_4$		A40
H_2WO_4	ZrH_2	$Zr(OH)_4$	NH_4ClO_4	A41
		$(CH_2)_n$		A42
			$ZrCl_4$	A43
			$ZrCl_4/NH_4ClO_4$	A44
	Zr	HDB	NH_4ClO_4	A45
		$HDB/(CH_2)_n$		A46
		HDB	NH_4Cl	A47
	Zr/ZrH_2	$Zr(OH)_4/(CH_2)_n$	NH_4Cl	A48

140

Propellant System

Oxidizer	Fuel	Coolant	Chlorides	Table Number
WO_3	ZrH_2	$Zr(OH)_4$	NH_4ClO_4	A49
		$(CH_2)_n$		A50
			$ZrCl_4$	A51
	Zr	ZrH_2	N_2H_5Cl	A52
			NH_4ClO_4	A53
		$ZrH_2/Zr(OH)_4$		A54
		HDB	NH_4Cl	A55
		HDB	NH_4ClO_4	A56
	Zr/ZrH_2			A57
$ZrO(NO_3)_2 \cdot 2H_2O$	ZrH_2	$Zr(OH)_4$	NH_4Cl	A57
			NH_4ClO_4	A58
		$(CH_2)_n$	NH_4Cl	A59
			NH_4ClO_4	A60

141